Radiator Designs and Experimental Platforms for Near-Field Radiative Heat Transfer

Mathieu Giroux

Thesis submitted to the University of Ottawa
in partial fulfillment of the requirements for the
Ph.D. in Mechanical Engineering

Department of Mechanical Engineering
Faculty of Engineering
University of Ottawa

Abstract

Near-field radiative heat transfer (NFRHT) consists of evanescent electromagnetic coupling occurring between two bodies at sub-wavelength distances, allowing to increase the radiative exchange beyond conventional laws of thermal radiation. NFRHT has demonstrated great potential for applications such as energy conversion and heat transfer control. In particular, multiple works predict that performances of near-field thermophotovoltaic (NFTPV) modules, in which a hot radiator is positioned at sub-wavelength distances from a cold photovoltaic (PV) cell, could significantly surpass those of current solid-state heat-to-electricity conversion technologies.

Despite its tremendous potential, experimental progress on NFRHT and NFTPV has been slow due to technical challenges and gaps in knowledge, three of which are at the core of this thesis. Firstly, only a limited number (i.e., fewer than 30) of NFRHT experimental platforms have been reported worldwide. The field therefore faces limited capabilities in characterizing novel materials for NFRHT. Secondly, NFTPV technology commands highly specialized PV cells. Unfortunately, most reported NFTPV platforms relied on basic PV cells fabricated in-house, or on commercially available photodetectors, resulting in modest performances. This leaves many promising PV materials, e.g., InAs, largely unexplored. Thirdly, theoretical research on new radiator materials for NFTPV applications has predominantly focused on one class of materials (i.e., plasmonic materials) that are difficult to experimentally investigate as their optical properties are contingent upon factors such as film annealing and deposition conditions. Therefore, the most suitable radiator material for NFTPV remains ambiguous.

To address these three challenges, our first objective is to develop experimental methods for NFRHT, our second objective is to achieve NFTPV measurements using an optimal bandgap (i.e., InAs-based) PV cell, and our third objective is to theoretically

design an optimized radiator for an InAs-based NFTPV system.

Within the scope of our first objective, we experimentally demonstrate the potential of using nanomechanical resonators as a temperature sensor for NFRHT measurements. Our approach offers a high-precision flexible NFRHT platform that could facilitate the testing of many new interesting materials. We report measurements in the deep sub-wavelength regime (i.e., regime dominated by surface resonance coupling) without the need for custom-fabricated micro-devices. Moreover, we demonstrate that the use of nanomechanical resonators could allow fundamental advances on simultaneous measurement of NFRHT and Casimir forces. If we can distinguish the contributions from Casimir and NFRHT effects, nanomechanical resonators could provide a path to experimentally demonstrate the correction to the Casimir forces out of thermal equilibrium.

For our second objective, we aim to conduct experimental research on the NFTPV effect using InAs-based PV cells. These cells, optimized for near-field thermal radiation, were custom-fabricated by PV cell experts (Prof. Karin Hinzer group, uOttawa, and Prof. Zbig Wasilewski group, University of Waterloo) in close collaboration with our group during this work. Unfortunately, the geometry of our radiator significantly limited the capabilities of our experimental platform, preventing NFTPV measurements. In fact, the large thermal mass radiator employed in our initial approach precluded high-temperature scans and greatly complicated the alignment process. In the future, we, therefore, recommend a revised approach relying on a localized heating element, enabling vibrational contact detection.

Finally, regarding our third objective, using a one-dimensional fluctuational electrodynamics model, we theoretically explore new radiator materials for NFTPV, focusing specifically on reproducible crystalline materials. More precisely, we investigate spectral electromagnetic coupling of a near-field thermal radiator with a PV cell in order to enhance spectral efficiency and total output power. We find that when the radiator and PV cell are both made of InAs, nearly a threefold improvement of spectral efficiency

is possible compared to a silicon radiator with the same InAs cell. This enhancement reduces subgap thermal transfer while maintaining power output. Through this work, we also uncover an overestimation of free carrier absorption in InAs dielectric function models. We propose a corrective model and demonstrate that it accurately represents the absorption at moderate doping levels but could be further refined for improved accuracy at higher doping levels.

Acknowledgments

This thesis was only possible due to the help and support of many individuals to whom I would like to express my sincere gratitude.

First, I would like to thank my supervisor, Prof. Raphael St-Gelais, for his continuous support and guidance. I feel extremely lucky to have been able to complete my PhD under his supervision. He is an incredible mentor and a great researcher and played a significant role in my decision to pursue a PhD. He always made sure to make this journey challenging but also very enjoyable for the both of us, and he is deeply devoted to creating the best possible working environment in the lab. I am also greatly thankful for the opportunities he provided over the years, and I look forward to continuing to work with him in the future.

I would also like to extend my appreciation to my co-supervisor, Prof. Jacob J. Krich, for his invaluable insights and support. I have greatly enjoyed working with him, which allowed me to significantly deepen my understanding of many theoretical aspects of my field. He is a brilliant and meticulous researcher whose input has always been greatly valuable to me and contributed significantly to the quality of my work.

I would also like to thank my past and present colleagues at the UOMEMS lab at the University of Ottawa, from whom I have learned a great deal and with whom I have formed lasting friendships. I specifically thank Chang Zhang, Michel Stephan, Maxime Brazeau, Gengyang Mu, and Nikaya Snell, who significantly contributed to the achievements presented in this thesis.

I am also grateful to Gavin Forcade, Mathieu de Lafontaine, and Karin Hinzer from SUNLAB, whose contributions were instrumental to our work with thermophotovoltaic cells.

I would also like to thank the machine shop at the University of Ottawa for their

exceptional work. They have greatly accelerated the progress of our work by providing valuable feedback and high-quality craftsmanship.

Finally, I would like to acknowledge the funding agencies without which this work would not have been possible. In particular, I thank the Natural Sciences and Engineering Research Council of Canada (NSERC), which provided most of the funding for this research project.

Statement of Originality

I declare that this thesis is my own original work and that I am its sole author. Chapters 1 and 2 provide background information from the literature relevant to the research presented in this thesis, while Chapters 3–6 are original contributions. Each publication within the chapters is preceded by a detailed breakdown of the specific contributions of each author. Unless otherwise stated, I conducted the experiments, simulations, and data analysis, and was the primary author of the text and figures.

Key Contributions

Several of the findings presented in this thesis have been published in peer-reviewed journals and presented at conferences. Below is a list of the key contributions that resulted from this research.

Journal Articles

1. **M. Giroux**, S. Molesky, R. St-Gelais, J. J. Krich, "Radiator tailoring for enhanced performance in InAs-based near-field thermophotovoltaics," *Solar Energy Materials and Solar Cells*, vol. 292, p. 113804, Oct. 2025.

2. G. P. Forcade, M. de Lafontaine, **M. Giroux**, M. C. Tam, Z. Wasilewski, J. J. Krich, R. St-Gelais, K. Hinzer, "Epi-grown broadband reflector for InAs-based thermophotovoltaics," *Solar Energy Materials and Solar Cells*, vol. 285, p. 113544, Jun. 2025.

3. **M. Giroux**, M. Stephan, M. Brazeau, S. Molesky, A. W. Rodriguez, J. J. Krich, K. Hinzer, R. St-Gelais, "Measurement of near-field radiative heat transfer at deep sub-wavelength distances using nanomechanical resonators," *Nano Letters*, vol. 23,

no. 18, p. 8490-8497, Sept. 2023.

4. **M. Giroux**, C. Zhang, N. Snell, G. Mu, M. Stephan, R. St-Gelais, "High resolution measurement of near-field radiative heat transfer enabled by nanomechanical resonators," *Applied Physics Letters*, vol. 119, no. 17, p. 173104, Oct. 2021.

Conference Presentations

1. **M. Giroux**, S. Molesky, R. St-Gelais, J. J. Krich, "Improved Near-Field Thermophotovoltaics with Matched Radiator and Receiver," *15th World Conference on Thermophotovoltaic Generation of Electricity (TPV-15)*, Madrid, Spain, Oct. 2024. [Oral presentation, **Best student finalist**]

2. **M. Giroux**, C. Zhang, M. Stephan, M. Brazeau, R. St-Gelais, "Near-field Radiative Heat Transfer Measurements Using Nanomechanical Resonators," *2023 Photonics and Electromagnetics Research Symposium (PIERS 2023)*, Prague, Czechia, Jul. 2023. [Oral presentation]

3. **M. Giroux**, M. Stephan, S. Molesky, A. W. Rodriguez, J. J. Krich, K. Hinzer, R. St-Gelais, "Measurement of Near-Field Radiative Heat Transfer at Deep Subwavelength Distances using Nanomechanical Resonators," *4th Frontiers of Nanomechanical Systems Workshop (FNS 2023)*, Delft, Netherlands, Jun. 2023. [Poster presentation]

4. **M. Giroux**, C. Zhang, M. Stephan, M. Brazeau, G. P. Forcade, S. Molesky, A. W. Rodriguez, J. J. Krich, K. Hinzer, R. St-Gelais, "Nanomechanical Resonators and High Flatness Silicon MEMS Radiators for Near-Field Radiative Heat Transfer Measurements," *14th World Conference on Thermophotovoltaic Generation of Electricity (TPV-14)*, Virtual, Jun. 2023. [Oral presentation]

5. **M. Giroux**, C. Zhang, G. Mu, N. Snell, R. St-Gelais, "Near-field radiative heat transfer measurements using SiN drumhead nanomechanical resonator," *17th Inter-*

national Workshop on Nanomechanical Sensing (NMC 2021), Virtual, Jun. 2021. [Oral presentation]

6. **M. Giroux**, C. Zhang, G. Mu, N. Snell, R. St-Gelais, "High Resolution Near-Field Radiative Heat Transfer Measurements Using Nanomechanical Oscillators," *2021 APS March Meetings*, Virtual, Mar. 2021. [Oral presentation]

Contents

List of Figures

List of Tables

Nomenclature

List of Symbols

Roman Symbols

A_j	Area of surface j [m^2]
$\overrightarrow{\mathbf{B}}$	Magnetic flux density [$\mathrm{Wb} \cdot \mathrm{m}^{-2}$]
c_0	Speed of light in vacuum (2.998×10^8) [$\mathrm{m} \cdot \mathrm{s}^{-1}$]
d	Distance [m]
d_0	Distance at the sphere apex [m]
d_{min}	Minimal distance [m]
$\overrightarrow{\mathbf{D}}$	Electric displacement [$\mathrm{C} \cdot \mathrm{m}^{-2}$]
e	Elementary charge (1.6022×10^{-19}) [C]
E	Young modulus [Pa]
E_{b}	Blackbody emissive power [$\mathrm{W} \cdot \mathrm{m}^{-2}$]
E_{f}	Energy of the final state [eV]
E_{F}	Fermi level [eV]
E_{g}	Bandgap energy [eV]
$E_{\mathrm{g}}^{\mathrm{MB}}$	Moss-Burstein shift [eV]
E_{i}	Energy of the initial state [eV]
E_λ	Spectral emissive power of a real surface [$\mathrm{W} \cdot \mathrm{m}^{-2} \cdot \mathrm{m}^{-1}$]
$E_{\lambda,\mathrm{b}}$	Blackbody spectral emissive power [$\mathrm{W} \cdot \mathrm{m}^{-2} \cdot \mathrm{m}^{-1}$]
$\overrightarrow{\mathbf{E}}$	Electric field [$\mathrm{V} \cdot \mathrm{m}^{-1}$]
f_0	Resonance frequency at room temperature [Hz]
f_j	Oscillator strength of the jth Lorentzian oscillator

$f_{\mathrm{P},j}$	Oscillator strength of the jth phonon mode
FF	Fill factor
F_{cas}	Casimir force [N]
F_{ij}	View factor from surface i to surface j
G_{NF}	NFRHT thermal conductance $[\mathrm{W}\cdot\mathrm{m}^{-2}\cdot\mathrm{K}^{-1}]$
h	Planck constant (6.626×10^{-34}) $[\mathrm{J}\cdot\mathrm{s}]$
$\hbar$	Reduced Planck constant (1.0546×10^{-34}) $[\mathrm{J}\cdot\mathrm{s}]$
$\overrightarrow{\mathbf{H}}$	Magnetic field strength $[\mathrm{A}\cdot\mathrm{m}^{-1}]$
i	Imaginary number $(\sqrt{-1})$
$\mathbf{I}$	Identity matrix
J	Current density $[\mathrm{A}\cdot\mathrm{m}^{-2}]$
J_{mp}	Current density at the maximum power point $[\mathrm{A}\cdot\mathrm{m}^{-2}]$
J_{sc}	Short-circuit current density $[\mathrm{A}\cdot\mathrm{m}^{-2}]$
$\overrightarrow{\mathbf{J_e}}$	Current density due to free electrons $[\mathrm{A}\cdot\mathrm{m}^{-2}]$
$\overrightarrow{\mathbf{J}_{\mathrm{fl}}}$	Fluctuating current density $[\mathrm{A}\cdot\mathrm{m}^{-2}]$
k	Wavevector $[\mathrm{rad}\cdot\mathrm{m}^{-1}]$
k_{B}	Boltzmann constant (1.3807×10^{-23}) $[\mathrm{J}\cdot\mathrm{K}^{-1}]$
k_{cas}	Effective spring constant induced by the Casimir force $[\mathrm{N}\cdot\mathrm{m}^{-1}]$
k_{F}	Fermi wavevector $[\mathrm{rad}\cdot\mathrm{m}^{-1}]$
k_j	Wavevector in medium j $[\mathrm{rad}\cdot\mathrm{m}^{-1}]$
k_{SiN}	Thermal conductivity of SiN $[\mathrm{W}\cdot\mathrm{m}^{-1}\cdot\mathrm{K}^{-1}]$
k_{v}	Vacuum wavevector $[\mathrm{rad}\cdot\mathrm{m}^{-1}]$
k_z	Perpendicular wavevector in vacuum $[\mathrm{rad}\cdot\mathrm{m}^{-1}]$
k_{zj}	Perpendicular wavevector in medium j $[\mathrm{rad}\cdot\mathrm{m}^{-1}]$
k_ρ	Parallel wavevector $[\mathrm{rad}\cdot\mathrm{m}^{-1}]$
K	Effective spring constant $[\mathrm{N}\cdot\mathrm{m}^{-1}]$
L	Side length of a square membrane [m]

m	Total number of Lorentzian oscillators
m_0	Electronic mass (9.109×10^{-31}) [kg]
m_{eff}	Resonator effective mass [kg]
m_{e}^*	Electron effective mass [kg]
M	Total number of phonon modes
n	Refractive index
n'_{IB}	Real part of the interband refractive index
n''_{IB}	Imaginary part of the interband refractive index
n_j	Refractive index of layer j
n_{PV}	Refractive index of the PV cell
n_{Rad}	Refractive index of the radiator
n_{SiN}	Refractive index of SiN
n_{SiO_2}	Refractive index of SiO_2
N	Carrier density $[\text{m}^{-3}]$
N_{d}	Doping level $[\text{m}^{-3}]$
N_{dip}	Number of elementary dipoles per unit volume $[\text{m}^{-3}]$
$\mathcal{P}$	Cauchy principal value of an integral
P	Useful transferred power $[\text{W} \cdot \text{m}^{-2}]$
P_0	Zero-point Casimir pressure $[\text{N} \cdot \text{m}^{-2}]$
P_j	Potential at node j $[\text{W} \cdot \text{m}^{-2}]$
P_{max}	Maximum electrical power density output $[\text{W} \cdot \text{m}^{-2}]$
P_{PV}	Electrical power density output of the PV cell $[\text{W} \cdot \text{m}^{-2}]$
P^{neq}	Total Casimir pressure out of thermal equilibrium $[\text{N} \cdot \text{m}^{-2}]$
$P_{\text{th}}^{\text{eq}}$	Lifshitz pressure at thermal equilibrium $[\text{N} \cdot \text{m}^{-2}]$
$P_{\text{th}}^{\text{neq}}$	Nonequilibrium thermal Casimir pressure $[\text{N} \cdot \text{m}^{-2}]$
$\overrightarrow{\mathbf{P}}$	Polarization $[\text{C} \cdot \text{m}^{-3}]$
$\dot{q}_{\text{FF}_{\text{back}}}$	Far-field radiative heat flux at the back side of the membrane $[\text{W} \cdot \text{m}^{-3}]$

$\dot{q}_{\mathrm{FF_{front}}}$	Far-field radiative heat flux at the front side of the membrane [$\mathrm{W \cdot m^{-3}}$]
$\dot{q}_{\mathrm{gen}}$	Rate of volumetric energy generation [$\mathrm{W \cdot m^{-3}}$]
q_{TF}	Thomas-Fermi screening wavevector [$\mathrm{rad \cdot m^{-1}}$]
Q	Spectral heat flux [$\mathrm{W \cdot s \cdot m^{-2}}$]
Q_{evan}	Evanescent spectral heat flux [$\mathrm{W \cdot s \cdot m^{-2}}$]
Q_{prop}	Propagating spectral heat flux [$\mathrm{W \cdot s \cdot m^{-2}}$]
Q_{TE}	Radiative heat flux associated with the TE polarization [$\mathrm{W \cdot s \cdot m^{-1}}$]
Q_{TM}	Radiative heat flux associated with the TM polarization [$\mathrm{W \cdot s \cdot m^{-1}}$]
r	Radius [m]
r_{eff}	Effective radius [m]
$r^{\gamma}_{j,j+1}$	Fresnel reflection coefficient at the $(j+1)$th interface in polarization state γ
$\overrightarrow{\mathbf{r}}$	Displacement from rest position [m]
R	Radius of curvature [m]
R^{γ}_{j}	Reflection coefficient of layer j in polarization state γ
R_j	Surface resistance of surface j [$\mathrm{m^{-2}}$]
R_{ij}	Space resistance between surfaces i and j [$\mathrm{m^{-2}}$]
t	Time [s]
t_j	Thickness of layer j [m]
$t^{\gamma}_{j,j+1}$	Fresnel transmission coefficient at the $(j+1)$th interface in polarization state γ
t_{SiN}	Thickness of the SiN membrane [m]
T	Temperature [K]
T^{γ}_{j}	Transmission coefficient of layer j in polarization state γ
T_{m}	Membrane temperature [K]
$\overline{T_{\mathrm{m}}}$	Average membrane temperature [K]
T_{sphere}	Glass half sphere temperature [K]
T_{Rad}	Radiator temperature [K]
T_{TE}	Transmission coefficient associated with the TE polarization

T_{TM}	Transmission coefficient associated with the TM polarization
T_{∞}	Ambient temperature [K]
u	Out-of-plane displacement [m]
V	Applied bias [V]
V_{mp}	Voltage at the maximum power point [V]
V_{oc}	Open-circuit voltage [V]

Greek Symbols

α	Thermal expansion coefficient [K^{-1}]
α_{IB}	Interband absorption coefficient [m^{-1}]
α_{lh}	Light-hole absorption coefficient [m^{-1}]
χ	Electric susceptibility
χ_{FC}	Susceptibility due to free carrier absorption
χ_{IB}	Susceptibility due to interband transitions
χ_{Lattice}	Susceptibility due to lattice vibrations
δ_j	Uncertainty associated with variable j
Δf	Resonance frequency shift [Hz]
Δf_{cas}	Resonance frequency shift due to Casimir forces [Hz]
Δf_{NF}	Resonance frequency shift due to near-field radiation [Hz]
ΔP_{th}	Nonequilibrium thermal Casimir pressure correction [$\mathrm{N} \cdot \mathrm{m}^{-2}$]
$\Delta P_{\mathrm{th}}^{\mathrm{evan}}$	Evanescent correction to nonequilibrium thermal Casimir pressure [$\mathrm{N} \cdot \mathrm{m}^{-2}$]
$\Delta P_{\mathrm{th}}^{\mathrm{prop}}$	Propagating correction to nonequilibrium thermal Casimir pressure [$\mathrm{N} \cdot \mathrm{m}^{-2}$]
ΔT	Temperature shift [K]
ΔT_{m}	Membrane temperature variation [K]
$\Delta \overline{T_{\mathrm{m}}}$	Average membrane temperature variation [K]

ϵ	Emissivity
ϵ_{Glass}	Emissivity of the glass radiator
ϵ_{SiN}	Emissivity of SiN
ϵ_{λ}	Spectral hemispherical emissivity
$\epsilon_{\lambda,\theta}$	Spectral directional emissivity
ε	Dielectric function
ε'	Real part of the dielectric function
ε''	Imaginary part of the dielectric function
ε_0	Vacuum permittivity (8.8542×10^{-12}) [$\text{F} \cdot \text{m}^{-1}$]
ε_{FC}	Free carrier dielectric function
ε_{IB}	Interband dielectric function
ε_{j0}	Static dielectric constant of layer j
ε_{∞}	High-frequency dielectric constant
η	Spectral efficiency
γ	Damping coefficient [$\text{rad} \cdot \text{s}^{-1}$]
γ_{F}	Free carrier damping coefficient [$\text{rad} \cdot \text{s}^{-1}$]
γ_j	Damping coefficient of the jth Lorentzian oscillator [$\text{rad} \cdot \text{s}^{-1}$]
γ_{P}	Phononic damping coefficient [$\text{rad} \cdot \text{s}^{-1}$]
$\gamma_{\text{P},j}$	Damping coefficient of the jth phonon mode [$\text{rad} \cdot \text{s}^{-1}$]
λ_{Th}	Characteristic wavelength of thermal radiation [m]
λ	Wavelength [m]
ν	Poisson ratio
ω	Frequency [$\text{rad} \cdot \text{s}^{-1}$]
ω_0	Resonance frequency at room temperature [$\text{rad} \cdot \text{s}^{-1}$]
ω_j	Resonance frequency of the jth Lorentzian oscillator [$\text{rad} \cdot \text{s}^{-1}$]
ω_{LO}	Longitudinal optical phonon frequency [$\text{rad} \cdot \text{s}^{-1}$]
$\omega_{\text{LO},j}$	Longitudinal optical phonon frequency of the jth phonon mode [$\text{rad} \cdot \text{s}^{-1}$]

ω_{p}	Plasma frequency [$\mathrm{rad} \cdot \mathrm{s}^{-1}$]
ω_{TO}	Transverse optical phonon frequency [$\mathrm{rad} \cdot \mathrm{s}^{-1}$]
$\omega_{\mathrm{TO},j}$	Transverse optical phonon frequency of the jth phonon mode [$\mathrm{rad} \cdot \mathrm{s}^{-1}$]
ρ	Density [$\mathrm{kg} \cdot \mathrm{m}^{-3}$]
ρ_{e}	Charge density [$\mathrm{C} \cdot \mathrm{m}^{-3}$]
σ	Stephan-Boltzmann constant (5.67×10^{-8}) [$\mathrm{W} \cdot \mathrm{m}^{-2} \cdot \mathrm{K}^{-4}$]
σ_0	Temperature-independent component of the in-plane stress [Pa]
σ_r	Position-dependent component of the in-plane stress [Pa]
τ_{th}	Characteristic thermal response time [s]
θ	Angle [rad]
θ_{c}	Critical angle for total internal reflection [rad]
θ_{i}	Angle of incidence [rad]
θ_{r}	Angle of reflection [rad]
θ_{t}	Angle of transmission [rad]
Θ	Planck mean oscillator energy [J]
ξ	Imaginary angular frequency [$\mathrm{rad} \cdot \mathrm{s}^{-1}$]

List of Abbreviations

3IT	Interdisciplinary Institute for Technological Innovation
AFM	Atomic force microscopy
BR	Back reflector
FF	Far-field
FSF	Front surface field
GaAs	Gallium arsenide
InAs	Indium arsenide

InSb	Indium antimonide
ITO	Indium-tin-oxide
IV	Current-voltage
LO	Longitudinal optical
MEMS	Micro-electromechanical systems
NFRF	New Frontiers in Research Fund
NFRHT	Near-field radiative heat transfer
NFTPV	Near-field thermophotovoltaic
NH_3	Ammonia
NREL	National Renewable Energy Laboratory
NSERC	Natural Sciences and Engineering Research Council of Canada
OGS	Ontario Graduate Scholarship
PCB	Printed circuit board
PID	Proportional integral derivative
PLL	Phase-locked loop
PV	Photovoltaic
RIE	Reactive ion etching
RTD	Resistance temperature detector
Si	Silicon
SiH_4	Silane
SiN	Silicon nitride
SiO_2	Silicon dioxide
SP	Surface polariton
SThM	Scanning thermal microscope
TE	Transverse electric
TEG	Thermoelectric generator
TEM	Transmission electron microscopy

TIR	Total internal reflection
TM	Transverse magnetic
TO	Transverse optical
TPV	Thermophotovoltaic

1. Introduction

Near-field radiative heat transfer (NFRHT) has attracted a lot of attention over the past years for potential applications such as energy conversion [1–8] and active thermal control [9–12], or for more fundamental studies on the effect of various materials [13–17], geometries [18], or external fields [19]. Generally speaking, radiative heat transfer occurs through the generation of propagating electromagnetic waves (i.e., far-field radiation), which carry energy from the surface of one body to another. The intensity of this radiation is well-described by the Planck distribution and always remains below the blackbody limit. However, when we bring the two objects to sub-wavelength distances, the system enters the near-field regime, where Planck's distribution is no longer valid. NFRHT consists of evanescent radiative thermal coupling occurring between two bodies at sub-wavelength distances. This evanescent coupling enables radiative heat transfer exceeding conventional laws of thermal radiation by orders of magnitude [20–22] while being concentrated over a narrow spectral bandwidth [23–26]. As demonstrated theoretically [3, 4], this enhancement could allow conversion of heat to electricity with a higher efficiency than any existing portable solid-state solution. In addition, by concentrating heat into a narrow spectral bandwidth [23–26], near-field thermal radiation could be used to better control the flux of heat [18], thus potentially enabling active thermal control devices such as thermal diodes and transistors [11, 27].

One of the most promising applications of NFRHT is waste heat recovery through near-field thermophotovoltaic (NFTPV) technology. Approximately 10% of the energy generated by primary energy carriers is lost as waste heat at temperatures above 600 K [28]. Harnessing a portion of this waste heat to generate electricity would significantly enhance energy-use efficiency and reduce carbon emissions. For 600–900 K heat sources, thermoelectric generators (TEGs) are the most-widely used solid-state technology [29].

While TEGs have experimentally achieved high power densities up to 22 W/cm^2 at 868 K [30], they suffer from low conversion efficiencies, typically less than 10% [29], as they are fundamentally limited by conduction losses, which prevent the achievement of large thermal gradients and high conversion efficiencies [31]. Thermophotovoltaic (TPV) systems present an alternative solid-state approach, offering high efficiencies, theoretically up to 45% at 900 K [29], although they suffer from low power densities, with theoretical estimates suggesting values below 0.2 W/cm^2 at 900 K [29]. This power density cannot be substantially increased, as it is fundamentally constrained by the blackbody limit. In contrast, NFTPV systems can achieve significantly higher power densities since the blackbody limit can be greatly surpassed in the near-field. Theoretical investigations [1–5] have indicated that NFTPV systems could achieve both high efficiencies and power densities, up to 40% and 11 W/cm^2 at 900 K [2]. The NFTPV effect is achieved by combining the NFRHT effect and the TPV effect; in other words, it involves positioning a hot radiator at sub-wavelength distances from a cold photovoltaic (PV) cell. This near-field coupling allows for tremendous amounts of heat to leave the hot object under the form of light, towards the PV cell, where it is converted to electricity.

Despite its tremendous potential, experimental progress on NFRHT and NFTPV has been slow due to technical challenges and gaps in knowledge, three of which are at the core of this thesis. Firstly, only a limited number (i.e., fewer than 30 [6, 12, 16, 26, 32–56]) of NFRHT experimental platforms have been reported worldwide. The field therefore faces limited capabilities in characterizing novel materials for NFRHT. Secondly, NFTPV technology requires highly specialized PV cells, further complicating experimental progress. Thirdly, theoretical research on new radiator materials for NFTPV applications has been scarce, therefore, the most suitable radiator material for NFTPV remains ambiguous. The objectives of this work, which address these challenges, are outlined below and are also summarized graphically in Fig. 1.1.

In relation to the first challenge, despite a large amount of promising theoretical work,

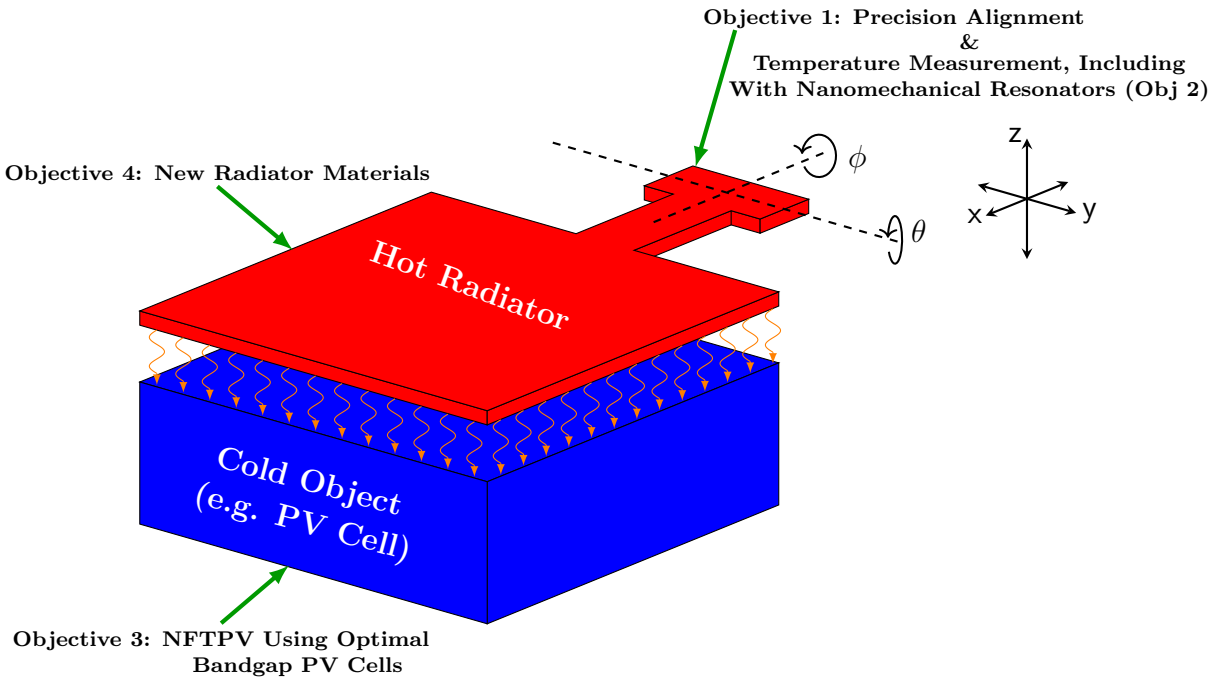

Figure 1.1: Illustration of a NFRHT system in which evanescent thermal coupling occurs between a hot radiator and a cold object positioned in extreme proximity. The illustration outlines the objectives of this thesis.

technical challenges of precision alignment at high temperatures often limit experimental progress on NFRHT. The separation required between the two surfaces in a NFRHT platform depends on the materials and geometry of the system, but for applications such as waste heat recovery and thermal control, separations below 100 nm are typically necessary [1, 57, 58]. In the case of waste heat recovery, the effective area of PV cells employed in NFTPV systems can reach up to $0.53\,\mathrm{cm}^2$ [59]. Positioning a radiator within 100 nm of a PV cell over such effective area poses significant challenges, as it requires a surface roughness below 50 nm and an angular deviation of no more than $750\,\mu^\circ$ to avoid contact. Several approaches have been reported to mitigate or overcome experimental difficulties. While some used nanotips [12, 16, 26, 32, 33, 60] or microspheres [34–37, 53, 61, 62] to eliminate the need to maintain parallelism between the coupled surfaces, others relied on more customized designs to study NFRHT between parallel surfaces using active parallelism control [38–46] or custom nanofabricated static devices

[7, 47–52]. The development of static devices is key for achieving practical application of NFRHT. However, their custom-fabricated nature makes it difficult to integrate various new materials [13–15, 18, 19, 63, 64] to experimentally study and confirm existing theoretical work on NFRHT. The fabrication processes involved in custom devices are tailored to their specific materials and geometries, limiting flexibility and complicating the integration of new materials. Since the majority of reported NFRHT experiments also employ custom nanodevices [7, 12, 16, 32, 34, 38–41, 47–53], experimental capabilities for investigating new materials for NFRHT remains limited. There is, consequently, a substantial imbalance between a large body of theoretically investigated phenomena and relatively modest experimental capabilities in the field of NFRHT research. Moreover, a large proportion of these platforms used SiO_2 for the radiator and receiver [65]. Although SiO_2 is efficient for NFRHT experiments, many materials with attractive properties, such as graphene [63], thin-film metals [13], multilayers [64], lossy materials [18], hyperbolic materials [14, 19], and metamaterials [15], remain largely untested.

In Chapter 4, we show that nanomechanical resonators offer a potential solution to this challenge. Nanomechanical resonators are small mechanical structures, that vibrate at a specific frequency when excited by an external source. These resonators enable the measurement of both force and temperature by monitoring the frequency shift induced by stress relaxation due to temperature variations or additional stress originating from external forces. Given that materials are routinely deposited on these resonators, this platform could facilitate the testing of many new interesting materials for NFRHT. Additionally, since nanomechanical resonators allow measurement of both temperature and forces simultaneously, they could offer the opportunity to investigate more fundamental phenomena occurring between two objects at sub-wavelength distances. Despite their promising performance in radiation sensing applications [66–75], these resonators had never been employed for NFRHT measurements prior to this thesis.

Concerning the second challenge—i.e., the requirement for highly specialized PV

cells—experimental progress on NFTPV, similarly to NFRHT, has been slow, arguably from lack of a truly multidisciplinary approach. The nanoscale heat transfer community [6, 8] has been, to date, the sole leader in the experimental development of the technology. This community relied on basic PV cells fabricated in-house [8] or on commercially available photodetectors [6], while the technology demands highly specialized PV cells. In fact, NFTPV requires specialized narrow bandgap PV cells to optimize power generation, as the low radiator temperature in waste heat recovery applications (< 1000 K) results in a photon flux at higher energies that is generally too weak for larger bandgap PV cells to be effective [6]. Additionally, thin geometries are necessary to minimize parasitic subgap absorption, which otherwise heats the cell and degrades performance [59, 76]. As a result, systems employing basic PV cells achieved modest performances: less than a nW of generated power and conversion efficiencies well below 1% [6, 8]. Recently, PV cells optimized for NFTPV operation [53, 77] were reported, leading to higher efficiencies and power densities, up to 14% and 0.75 W/cm^2. However, these performances either required liquid nitrogen cooling [53] or a hot radiator temperature (~ 1200 K) [77] much higher than the typical temperature of waste heat recovery applications (< 1000 K) [6].

In Chapter 5, we conduct experimental research on the NFTPV effect using custom-fabricated InAs-based PV cells. InAs PV cells demonstrated great potential in theoretical works [2, 78] for NFTPV applications, due to their bandgap being well-aligned with the Planck spectrum for the temperature range of waste heat recovery applications. Nevertheless, NFTPV measurements with InAs cells had not been reported when we undertook this work[1], except for one preliminary demonstration performed in the early stages of the field [7].

Regarding the third challenge, while experimental works are slowly starting to implement PV cells optimized for NFTPV operation [53, 77], many studies still rely on doped silicon radiators [6, 77, 79]. A few theoretical works [4, 5] reported optimized

[1]NFTPV measurements with InAs cells have now been reported in Ref. 59

radiator designs for NFTPV applications. These studies relied on plasmonic materials, such as indium-tin-oxide (ITO), which exhibit surface polariton resonances in the infrared region, enhancing the radiative heat flux in a spectral distribution located just above the bandgap of the PV cell. While these materials greatly improve the theoretical performance of NFTPV systems, in practice their optical properties are contingent upon factors such as film annealing and deposition conditions [80], making the experimental reproduction of these results quite challenging. Therefore, the lack of investigation into reproducible radiator materials leaves the nature of the most suitable radiator material for NFTPV ambiguous.

In Chapter 6, with eye towards near-term large-scale implementation, we theoretically explore new radiator materials for NFTPV, focusing specifically on reproducible crystalline materials. More precisely, we systematically investigate spectral electromagnetic coupling of InAs and Si near-field thermal radiators with an InAs PV cell in order to enhance spectral efficiency and total output power.

In summary, the main objective of this thesis is to experimentally and theoretically investigate the NFRHT phenomenon, with a particular emphasis on NFTPV energy conversion. More specifically:

1. Build a flexible platform for experimental testing of new materials for NFRHT and NFTPV.

2. Investigate the potential of nanomechanical resonators for NFRHT measurements.

3. Achieve NFTPV measurements using an optimal bandgap material, i.e., InAs.

4. Theoretically investigate new radiator materials for improving the performance of NFTPV systems.

In the following chapter, a theoretical review of NFRHT and related concepts is provided. In Chapter 3, we summarize the different stages of development of our experimental platforms, including our recommendation on future improvements. Chapter

4 discusses our efforts in achieving Objectives 1 and 2, while Chapters 5 and 6 focus on Objectives 3 and 4, respectively. In Chapters 4 and 6, we present articles dedicated to addressing the corresponding objectives. Conversely, Chapter 5 focuses on the technical challenges encountered during attempts to perform NFTPV measurements using custom InAs PV cells (i.e., Objective 3). Finally, the conclusions and recommendations are outlined in Chapter 7.

2. Background

Planck's distribution, derived in 1900 [81], is well known in the scientific community and often used to determine the radiative heat exchange between two bodies. It is, however, very often forgotten that Planck's distribution is only valid when all characteristic lengths in the system are much greater than the characteristic wavelength of thermal radiation. When this assumption is not respected, the radiative heat transfer follows very different sets of laws. In fact, in the near-field, radiative heat transfer can exceed conventional laws of thermal radiation by orders of magnitude [20–22]. Theoretical works [3, 4] have demonstrated that this enhancement could allow to convert heat to electricity with a higher efficiency than any existing portable solid-state solution.

This chapter provides an overview of NFRHT and related concepts and is structured as follows. Section 2.1 begins with a brief review of far-field thermal radiation concepts, followed by Section 2.2, which covers the fundamentals of NFRHT, and Section 2.3, which discusses energy harvesting using NFRHT. In Section 2.4, we address dielectric function modeling, and in Section 2.5, we delve into nanomechanical resonators. Finally, Section 2.6 elaborates on the Casimir forces.

2.1 Far-Field Radiative Heat Transfer

Thermal radiation consists of energy emitted by matter in the form of light. Any object at nonzero temperature radiates energy carried by electromagnetic waves (i.e., photons) [82]. This thermal radiation arises from the movement of charges in the material. As the temperature of an object rises, its atoms vibrate more which causes its electrons to be excited to higher energy states. Eventually, these electrons return to their original states, emitting electromagnetic waves in the process [83]. The spectral distribution of

the emitted radiation varies with temperature, as electrons occupy different energy states.

Emission is a volumetric phenomenon, as the radiation emerging from a finite volume of matter results from the combined contributions of local emissions throughout that volume. However, radiation is generally treated as a surface phenomenon, since in most solids and liquids, radiation emitted from interior molecules is strongly absorbed by neighbouring molecules. In fact, radiation emitted from a solid or liquid primarily originates from molecules located within roughly 1 µm of the exposed surface [82]. This behavior is reflected in the widely used Planck distribution, which treats emission as a surface phenomenon [84].

Planck's distribution describes the spectral emissive power (in $\mathrm{W} \cdot \mathrm{m}^{-2} \cdot \mathrm{m}^{-1}$) of a blackbody (i.e., an ideal radiator), denoted as $E_{\lambda,\mathrm{b}}$

$$E_{\lambda,\mathrm{b}}(\lambda, T) = \frac{2\pi h c_0^2}{\lambda^5 \left(e^{\frac{hc_0}{\lambda k_\mathrm{B} T}} - 1\right)}, \tag{2.1}$$

where λ is the wavelength of the emitted radiation, h is the Planck constant [6.626×10^{-34} $\mathrm{J} \cdot \mathrm{s}$], c_0 is the speed of light in vacuum [2.998×10^8 m/s], k_B is the Boltzmann constant [1.3807×10^{-23} J/K], and T is the temperature. The blackbody is defined as a perfect emitter and absorber, serving as a reference for comparing real absorbing and emitting materials. For real surfaces, the emissivity ϵ, which ranges between 0 and 1, is used to quantify how efficiently a surface emits energy relative to a blackbody. As a result, the spectral emissive power of a real surface E_λ depends on its spectral hemispherical emissivity ϵ_λ and the spectral emissive power of a blackbody at the same temperature

$$E_\lambda(\lambda, T) = \epsilon_\lambda(\lambda, T)\, E_{\lambda,\mathrm{b}}(\lambda, T). \tag{2.2}$$

Note that Eq. 2.2 is only valid for a diffuse emitter [82].

According to Eq. 2.2, the spectral heat flux between two real surfaces always remains below the blackbody limit (see Fig. 2.1a). However, Planck's distribution was derived

under the assumptions of ray optics, and, therefore, is only valid in the far-field regime, where all the characteristic lengths of the system are much greater than the characteristic wavelength of thermal radiation λ_{Th} [85]. The characteristic wavelength λ_{Th} corresponds to the wavelength at which thermal emission reaches its maximum for a given temperature, as determined by Wien's displacement law

$$\lambda_{\mathrm{Th}} T = 2898\,\mu\mathrm{m} \cdot \mathrm{K}. \tag{2.3}$$

If this condition is violated and the distance between the two bodies becomes smaller than the characteristic wavelength, the system enters the near-field regime. The interaction occurring between two bodies in the near-field can significantly enhance the radiative heat flux, allowing to overcome conventional laws of thermal radiation (see Fig. 2.1b). NFRHT is further discussed in Section 2.2.

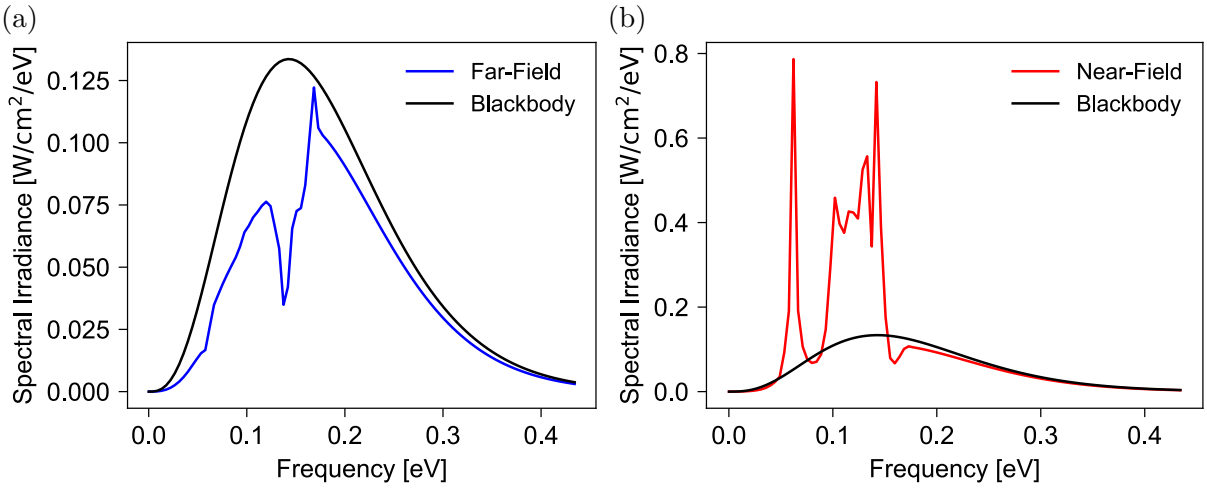

Figure 2.1: Spectral radiative heat flux between two bodies (a) in the far-field (i.e., where all the characteristic lengths of the system are much greater than the characteristic wavelength of thermal radiation λ_{Th}) and (b) in the near-field (i.e., where the distance between the two bodies is smaller than λ_{Th}).

2.2 Near-Field Radiative Heat Transfer

In this section, we provide an overview of NFRHT. We first discuss the working principles of NFRHT in Section 2.2.1, followed by its modeling in Section 2.2.2.

2.2.1 Working Principle

In the case of two radiating bodies at large distances, the exchange of energy occurs through the generation of propagating electromagnetic waves (i.e., far-field radiation), which carries energy from the surface of one body to another, as discussed in Section 2.1. However, as we bring these two bodies to distances smaller than the characteristic wavelength of the thermal radiation λ_{Th} (defined by Wien's displacement law), a phenomenon known as NFRHT emerges. At such distances, the radiative heat transfer is dominated by evanescent waves—electromagnetic modes that decay exponentially in the direction perpendicular to the surface (see Fig. 2.2). These evanescent waves only interact with bodies located in extreme proximity to the surface. If the separation between bodies exceeds the characteristic wavelength, the evanescent wave field of a surface cannot interact with another surface and, therefore, no net energy is radiated from the surface through evanescent modes [84].

Evanescent waves, as illustrated in Fig. 2.2, originate from two distinct sources: frustrated modes and surface polaritons. Frustrated modes, which are possibly the most common source, arise from frustrated total internal reflections. The interaction of light at an interface between two media of refractive index $n_1 > n_2$ is represented in Fig. 2.3. In a typical refraction scenario (case on the left in Fig. 2.3), a light ray propagates in medium 1 at an angle θ_{i} towards the interface between medium 1 and medium 2. At the interface, the light ray is partially reflected back in medium 1 at an angle $\theta_{\mathrm{r}} = \theta_{\mathrm{i}}$, while the remainder is transmitted into medium 2 at an angle θ_{t}, thereby giving rise to a propagating wave. The angle of the transmitted ray can be found using Snell's law

(a) Far-Field Radiation

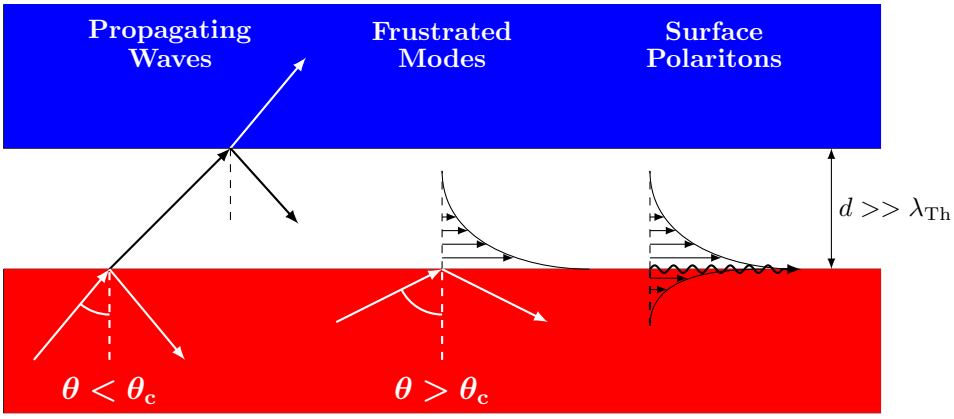

(b) Near-Field Radiation

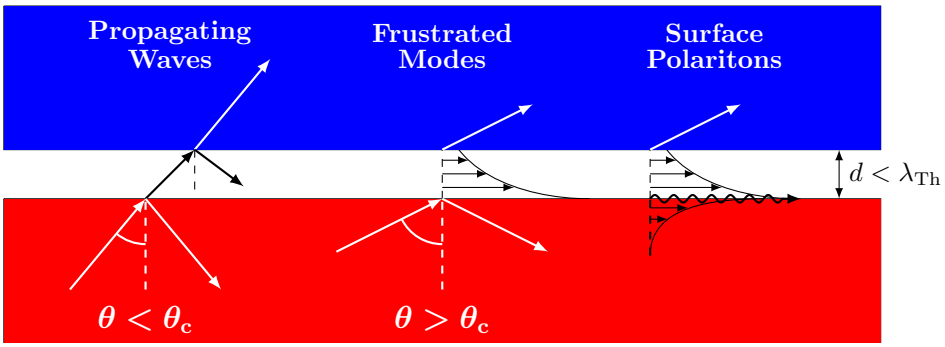

Figure 2.2: (a) Representation of the far-field radiative heat transfer occurring between two planar surfaces separated by a vacuum gap larger than the characteristic wavelength of thermal radiation λ_{Th}. At such distance, since the evanescent waves generated by frustrated modes and surface polaritons are not able to reach the second surface, the two bodies only exchange heat through propagating waves. (b) In the case where the vacuum gap is smaller than λ_{Th}, evanescent waves can interact with the second body allowing NFRHT to take place (similar to Fig. 2.1 of Ref. 86).

$$n_1 \sin(\theta_{\mathrm{i}}) = n_2 \sin(\theta_{\mathrm{t}}). \tag{2.4}$$

However, in this case, since $n_1 > n_2$, Snell's law predicts that for a certain angle of incidence θ_{i} all the light is reflected back in medium 1 (case on the right in Fig. 2.3). The critical angle θ_{c} at which this total internal reflection (TIR) occurs is given by

$$\theta_{\mathrm{c}} = \sin^{-1}\left(\frac{n_2}{n_1}\right). \tag{2.5}$$

As shown in Fig. 2.3, Maxwell's equations predict that the optical disturbance occurring at the surface of the material during a TIR generates an exponentially decaying evanescent wave at the interface between medium 1 and medium 2 [86]. When a third medium (the cold body) is introduced and approached to sub-wavelength distances from the first medium (the hot body), the second medium (the vacuum gap) forms a thin film with a thickness on the order of the wavelength of the light. This "frustrates" the TIR of the light allowing it to transmit energy to the third medium [87]. A similar phenomenon is observed in bare optical fibers densely packed together, commonly referred to as "cross talk" [83].

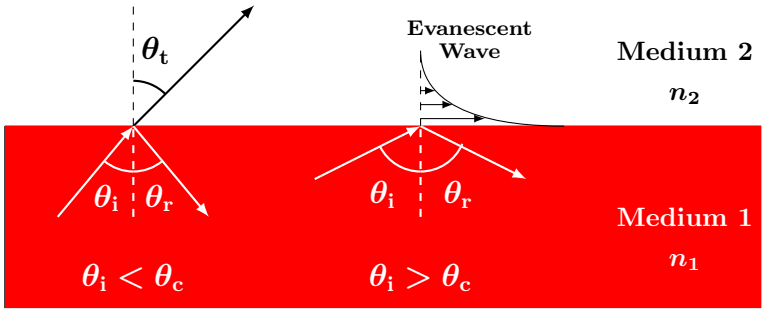

Figure 2.3: Representation of the interaction of light at the interface between two media with refractive indices $n_1 > n_2$. In the case of a standard interaction (i.e., $\theta_i < \theta_c$), part of the incident light is transmitted into medium 2. However, if $\theta_i > \theta_c$, the incident light undergoes a TIR. The evanescent wave illustration depicts the electric field amplitude and direction, with the amplitude decaying away from the surface in medium 2 (similar to Fig. 2.1 of Ref. 88).

Surface modes or surface polaritons are electromagnetic modes that arise from the coupling of an electromagnetic field with a resonant polarization oscillation at the surface of the material [89]. There are two distinct types of surface polaritons: surface plasmon-polaritons and surface phonon-polaritons. Surface plasmon-polaritons, arising in electrically conducting materials, are due to the coupling of an electromagnetic field with free electrons. Likewise, surface phonon-polaritons, arising in the crystal lattice of a material, are due to the coupling of an electromagnetic field with optical phonons [89]. In both cases, the surface modes propagate along the interface between two media with

evanescent fields decaying exponentially in both materials [90], as illustrated in Fig. 2.4. These surface modes can lead to quasi-monochromatic thermal emission due to the large number of electromagnetic modes concentrated within a narrow spectral band [84].

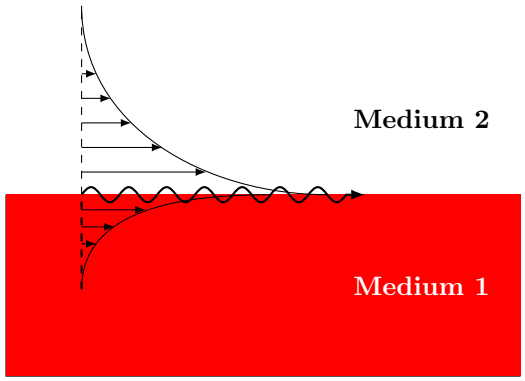

Figure 2.4: Representation of a surface polariton occurring at the interface between an optical medium (medium 1) and vacuum (medium 2) (similar to Fig. 2.2 of Ref. 88).

2.2.2 Modeling

As discussed earlier, Planck's distribution [81] is only valid if all the characteristic lengths of the system are much greater than the characteristic wavelength of thermal radiation. Therefore, in the near-field, Planck's distribution is not valid. A model for NFRHT was eventually derived, from the fluctuational electrodynamics framework [91], by Polder and Van Hove in 1971 [22].

The fluctuational electrodynamics framework is derived from Maxwell's equations by incorporating fluctuating currents to account for the thermally generated electromagnetic field [91]. Assuming time-harmonic fields of the form $e^{-i\omega t}$, the equations are expressed in the frequency domain as follows [84]:

$$\nabla \cdot \overrightarrow{\mathbf{D}} = \rho_{\mathrm{e}}, \tag{2.6}$$

$$\nabla \cdot \overrightarrow{\mathbf{B}} = 0, \tag{2.7}$$

$$\nabla \times \overrightarrow{\mathbf{E}} = i\omega \overrightarrow{\mathbf{B}}, \tag{2.8}$$

$$\nabla \times \overrightarrow{\mathbf{H}} = -i\omega \overrightarrow{\mathbf{D}} + \overrightarrow{\mathbf{J}_{\mathbf{e}}} + \overrightarrow{\mathbf{J}_{\mathrm{fl}}}, \tag{2.9}$$

where ω is the angular frequency, i is the complex constant, ρ_{e} is the charge density, and $\overrightarrow{\mathbf{D}}$, $\overrightarrow{\mathbf{B}}$, $\overrightarrow{\mathbf{E}}$, and $\overrightarrow{\mathbf{H}}$ denote the electric displacement, magnetic flux density, electric field, and magnetic field strength, respectively. The quantities $\overrightarrow{\mathbf{J}_{\mathbf{e}}}$ and $\overrightarrow{\mathbf{J}_{\mathrm{fl}}}$ represent the current density due to free electrons and the fluctuating current density, respectively. In this framework, Ampère's law (Eq. 2.9) includes a fluctuating component $\overrightarrow{\mathbf{J}_{\mathrm{fl}}}$, as thermal currents are treated statistically, which induces additional fields. These fluctuating currents, representing the stochastic nature of thermal emission, arise from the random motion of charges due to their thermal energy [89]. The relation between the fluctuating currents and the local temperature of the matter can be derived from the fluctuation-dissipation theorem [92]

$$\left\langle \overrightarrow{\mathbf{J}_{\mathrm{fl}}}(\overrightarrow{\mathbf{r}}\,', \omega) \otimes \overrightarrow{\mathbf{J}_{\mathrm{fl}}}^{*}(\overrightarrow{\mathbf{r}}\,'', \omega') \right\rangle = \frac{4\omega\varepsilon_0\varepsilon''(\omega)}{\pi}\, \Theta(\omega, T)\, \delta(\overrightarrow{\mathbf{r}}\,' - \overrightarrow{\mathbf{r}}\,'')\, \delta(\omega - \omega')\, \mathbf{I}, \tag{2.10}$$

where $\otimes$ denotes the outer product, $\langle \cdot \rangle$ denotes an ensemble average, and the superscript * refers to the complex conjugate. The terms $\delta(\overrightarrow{\mathbf{r}}\,' - \overrightarrow{\mathbf{r}}\,'')$ and $\delta(\omega - \omega')$ are Dirac functions, and $\mathbf{I}$ is the identity matrix. ε_0 denotes the vacuum permittivity [8.8542×10^{-12} F/m], while ε'' represents the imaginary part of the dielectric function. The vector $\overrightarrow{\mathbf{r}}$ is a position vector, and Θ is the Planck mean oscillator energy given by

$$\Theta\left(\omega, T\right) = \frac{\hbar\omega}{e^{\hbar\omega/k_{\mathrm{B}}T} - 1}, \tag{2.11}$$

where $\hbar$ is the reduced Planck constant [1.0546×10^{-34} J $\cdot$ s]. While Planck's distribution

approximates emission to a surface process, fluctuational electrodynamics treats emission as a volumetric process [84]. When objects are sufficiently large and far apart, the details of volumetric emission become negligible, allowing emission to be modeled as a surface phenomenon. However, when this approximation breaks down, emission must be treated as a volumetric process.

Using the formalism described above, the spectral NFRHT between two films can be expressed in terms of the reflection and transmission coefficients, as described in Ref. 93. This model describes the NFRHT between two perfectly smooth parallel, homogeneous, isotropic, nonmagnetic films in local thermodynamic equilibrium, as depicted in Fig. 2.5. The bodies are infinite in the ρ-direction and azimuthally symmetric (i.e., invariant over ϕ), such that the system can be approximated to a one-dimensional problem. The two films of thickness t_1 and t_3, kept at temperatures T_1 and T_3, are separated by a vacuum gap of length d, and have frequency-dependent dielectric functions $\varepsilon_1(\omega)$ and $\varepsilon_3(\omega)$. Modeling of the dielectric function is discussed in Section 2.4.

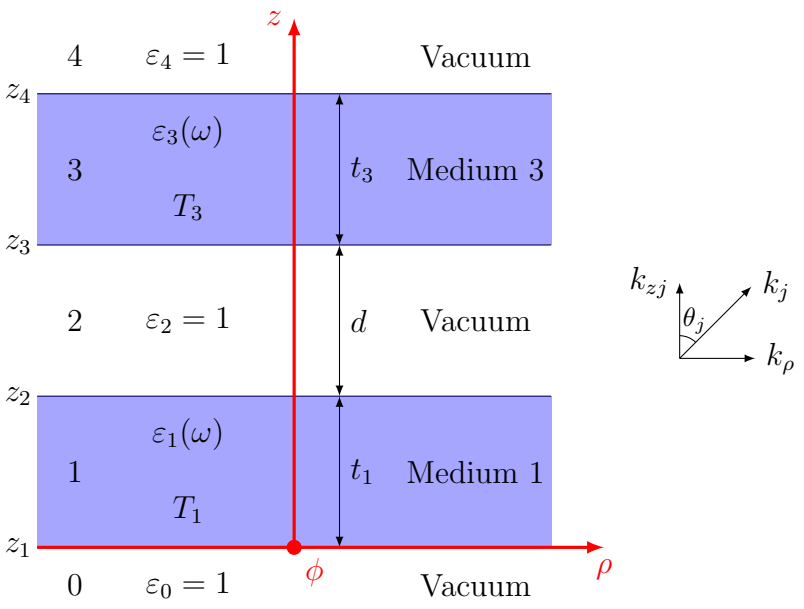

Figure 2.5: Representation of a two-body system submerged in vacuum for which the NFRHT is computed between layer 1 and 3 (similar to Fig. 1 of Ref. 93).

For such a case, the spectral heat flux at a specific location z in layer j resulting

from the emission from film 1 can be determined by computing the time-averaged z-component of the Poynting vector [93]. The radiative heat flux absorbed by medium 3 can, afterwards, be computed by subtracting the flux crossing the interface 3-4 (i.e., $j = 4$, $z = z_4$) from the flux crossing the interface 2-3 (i.e., $j = 3$, $z = z_3$). This derivation yields two expressions, representing the propagating $Q_{\text{prop}}(\omega)$ and evanescent $Q_{\text{evan}}(\omega)$ contributions to the spectral heat flux absorbed by film 3 due to emissions from film 1

$$Q_{\text{prop}}(\omega) = \frac{\Theta(\omega, T_1)}{4\pi^2} \cdot \sum_{\gamma=\text{TE,TM}} \int_0^{k_\text{v}} \frac{\left(1 - |R_1^\gamma|^2 - |T_1^\gamma|^2\right)\left(1 - |R_3^\gamma|^2 - |T_3^\gamma|^2\right)}{\left|1 - R_1^\gamma R_3^\gamma e^{2ik_z d}\right|^2} k_\rho \mathrm{d}k_\rho, \tag{2.12}$$

$$Q_{\text{evan}}(\omega) = \frac{\Theta(\omega, T_1)}{\pi^2} \cdot \sum_{\gamma=\text{TE,TM}} \int_{k_\text{v}}^{\infty} \frac{\text{Im}\left(R_1^\gamma\right)\text{Im}\left(R_3^\gamma\right)}{\left|1 - R_1^\gamma R_3^\gamma e^{2ik_z d}\right|^2} e^{-2d\text{Im}(k_z)} k_\rho \mathrm{d}k_\rho, \tag{2.13}$$

where $k_\text{v} = \omega/c_0$ is the vacuum wavevector, k_ρ is the wavevector parallel to the surface of the layers, and $k_z = \sqrt{k_\text{v}^2 - k_\rho^2}$ is the perpendicular wavevector in vacuum (see Fig. 2.5). R_j^γ and T_j^γ are, respectively, the reflection and transmission coefficients of layer j in polarization state γ (transverse electric (TE) or transverse magnetic (TM)). Using the multilayer formalism [94], these coefficients can be expressed as follows:

$$R_j^\gamma = \frac{r_{j-1,j}^\gamma + r_{j,j+1}^\gamma e^{2i\sqrt{k_j^2 - k_\rho^2}t_j}}{1 + r_{j-1,j}^\gamma r_{j,j+1}^\gamma e^{2i\sqrt{k_j^2 - k_\rho^2}t_j}}, \tag{2.14}$$

$$T_j^\gamma = \frac{t_{j-1,j}^\gamma t_{j,j+1}^\gamma e^{i\sqrt{k_j^2 - k_\rho^2}t_j}}{1 + r_{j-1,j}^\gamma r_{j,j+1}^\gamma e^{2i\sqrt{k_j^2 - k_\rho^2}t_j}}, \tag{2.15}$$

where $k_j = n_j k_\text{v}$ is the wavevector in the j^{th} medium, t_j is the thickness of the j^{th} layer, and $r_{j,j+1}^\gamma$ and $t_{j,j+1}^\gamma$ are, respectively, the Fresnel reflection and transmission coefficients at the $(j+1)^{\text{th}}$ interface in polarization state γ. The Fresnel coefficients are given by [83]

$$r_{j,j+1}^{\mathrm{TE}} = \frac{\sqrt{k_j^2 - k_\rho^2} - \sqrt{k_{j+1}^2 - k_\rho^2}}{\sqrt{k_j^2 - k_\rho^2} + \sqrt{k_{j+1}^2 - k_\rho^2}}, \tag{2.16}$$

$$r_{j,j+1}^{\mathrm{TM}} = \frac{\frac{k_{j+1}}{k_j}\sqrt{k_j^2 - k_\rho^2} - \frac{k_j}{k_{j+1}}\sqrt{k_{j+1}^2 - k_\rho^2}}{\frac{k_{j+1}}{k_j}\sqrt{k_j^2 - k_\rho^2} + \frac{k_j}{k_{j+1}}\sqrt{k_{j+1}^2 - k_\rho^2}}, \tag{2.17}$$

$$t_{j,j+1}^{\mathrm{TE}} = \frac{2\sqrt{k_j^2 - k_\rho^2}}{\sqrt{k_j^2 - k_\rho^2} + \sqrt{k_{j+1}^2 - k_\rho^2}}, \tag{2.18}$$

$$t_{j,j+1}^{\mathrm{TM}} = \frac{2\sqrt{k_j^2 - k_\rho^2}}{\frac{k_{j+1}}{k_j}\sqrt{k_j^2 - k_\rho^2} + \frac{k_j}{k_{j+1}}\sqrt{k_{j+1}^2 - k_\rho^2}}. \tag{2.19}$$

Note that, here, we only compute the radiative heat flux absorbed by film 3. Therefore, to compute the net radiative heat transfer between the films, we must also subtract the heat flux absorbed in layer 1 due to emissions from film 3. This flux can be computed using Eqs. 2.12 and 2.13, except that the Planck mean oscillator energy is now calculated using temperature T_3.

Since Polder and Van Hove derived the first NFRHT model in 1971 [22], significant efforts have been made to enable the modeling of more complex structures [54, 85, 95, 96]. For instance, the model described in this section (Eqs. 2.12–2.19) is tailored to enable the computation of NFRHT in multilayer stacks. Additionally, the Derjaguin approximation [97], which models a spherical shape by treating it as a series of small planar elements, can be employed to compute the NFRHT for curved surfaces. This approximation is proven to be valid for NFRHT [35], especially for relatively large objects.

In this work, we employ a range of approximations to the NFRHT model described above (Eqs. 2.12–2.19). In Chapter 4, we simplify the model by neglecting transmission and approximating the two bodies as semi-infinite stacks, as done in Ref. 5. In Chapter 6, we build on the one-dimensional fluctuational electrodynamics model from Ref. 98,

which accounts for transmission, consequently allowing to compute the absorption in each sublayer of a stack.

2.3 Near-Field Thermophotovoltaic Systems

In this section, we provide an overview of NFTPV systems. We first cover the working principle of PV cells in Section 2.3.1, and subsequently, we discuss the performance of NFTPV systems in Section 2.3.2.

2.3.1 Photovoltaic Effect

The simplest form of a PV cell is a p-n junction, consisting of a positively doped (p-doped) semiconductor in contact with a negatively doped (n-doped) semiconductor. A p-doped semiconductor is a material in which impurities that produce excess holes (positive charge carriers) have been introduced. For example, in Si (a Group IV semiconductor), Group III elements (generally boron) are commonly used as dopants. Similarly, an n-doped semiconductor is a material in which impurities that provide excess electrons (negative charge carriers) have been introduced. In Si, this is typically achieved using Group V elements (generally phosphorus or antimony). This p-n junction is typically grown on top of a thick crystal substrate, which provides mechanical support and can sometimes play a role in heat dissipation and electrical insulation [99].

When the p-doped and n-doped semiconductors are brought in contact, a large density gradient exists between the two sides of the junction. Therefore, free electrons from the n-doped region flow across the junction to fill up some holes in the p-doped region. Likewise, holes in excess in the p-doped region flow across the junction to recombine with some free electron in the n-doped region [83]. This flow of electrons and holes across the junction is known as diffusion. This process leaves behind uncompensated positive donor ions (in the n-doped region) and negative acceptor ions (in the p-doped region) near the p-n junction, as illustrated in Fig. 2.6. The presence of these uncompensated

electrical charges generates an electric field $\overrightarrow{\mathbf{E}}$ across the junction, opposing the diffusion of electrons and holes [100]. Eventually, this electric field $\overrightarrow{\mathbf{E}}$ becomes large enough to halt the diffusion of electrons and holes completely. Therefore, the region near the junction interface has a much lower concentration of free charge carriers compared to the rest of the semiconductor. This region is called the depletion region [101].

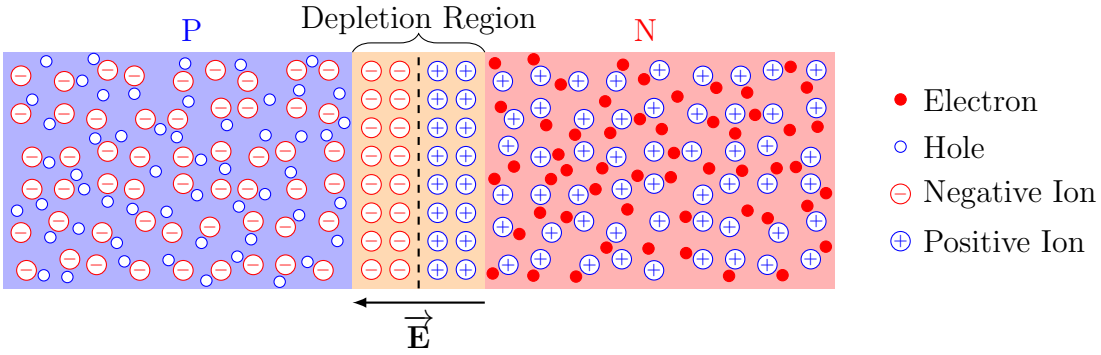

Figure 2.6: Representation of a p-n junction (similar to Fig. 17 of Ref. 101).

When photons of energy exceeding the bandgap energy E_g of the semiconductor (i.e., energy required to excite an electron from the valence band to the conduction band) are absorbed near the junction, they generate electron-hole pairs. The electric field $\overrightarrow{\mathbf{E}}$ present at the junction separates the electron-hole pairs such that electrons are collected in the n-doped region and the holes in the p-doped region, causing a change in voltage. This flow of electrons, consequently, generates an electrical current in the semiconductor [83].

Power generation in a PV cell is typically evaluated from the J-V characteristic, which depicts the relation between the current density J and the applied bias V. Fig. 2.7 illustrates the performance of a PV cell under both dark and illuminated conditions. Under dark conditions (i.e., when the p-n junction is not illuminated), the PV cell operates solely as a diode. In such case, the J-V characteristic exhibits the typical exponential curve associated with a diode, and the measured current, called dark current, results from the applied voltage at the junction. Under illuminated conditions, the radiation

absorbed within the junction generates a photocurrent opposing the dark current. This photocurrent shifts part of the J-V curve into the fourth quadrant indicating power generation [102]. Under these conditions, the power density output of the PV cell is given by

$$P_{\mathrm{PV}} = -JV. \tag{2.20}$$

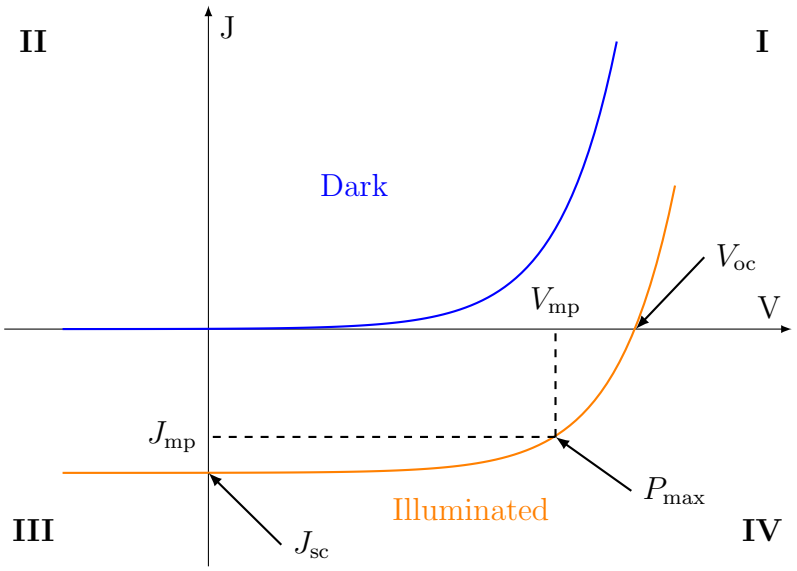

Figure 2.7: Schematic representation of the J–V characteristic of a PV cell under dark (in blue) and illuminated (in orange) conditions (similar to Fig. 2 of Ref. 103).

Valuable insights on key parameters can be extracted from the illuminated J-V characteristic of a PV cells. For example, the short-circuit current density (J_{sc}) corresponds to the current density when the junction is shorted, as depicted in Fig. 2.7. On the other hand, the open-circuit voltage (V_{oc}) represents the voltage in the absence of a current flow. Additionally, the current density (J_{mp}) at the maximum power point (P_{max}) and its corresponding voltage (V_{mp}) indicate the operating condition that maximizes the power output of the PV cell. These key parameters can be used to determine the fill factor (FF)

$$FF = \frac{J_{\mathrm{mp}} V_{\mathrm{mp}}}{J_{\mathrm{sc}} V_{\mathrm{oc}}}. \tag{2.21}$$

This fill factor is an indication of how square the J-V characteristic is and gives direct insights on how effectively the incident light is converted to electrical power. Consequently, a larger fill factor indicates that the device operates more efficiently. Therefore, to maximize the energy conversion efficiency and overall performance of the PV cell, one must simultaneously optimize the short-circuit current, open-circuit voltage, and fill factor [104].

2.3.2 Near-Field Thermophotovoltaic Systems

NFTPV systems, which combine NFRHT detailed in Section 2.2.1 and the PV effect discussed in Section 2.3.1, have the potential to enable performances that greatly overcome those of current solid-state heat-to-electricity conversion systems [1–5]. In TPV systems, photons emitted by a hot object in the far-field cross a vacuum gap to be absorbed by a PV cell, generating electrical power. While TPV systems can seem like interesting technology for waste heat recovery, they require a hot radiator temperature much too high for most practical applications, as the radiative heat flux is constrained by the blackbody limit. The radiator temperature (< 1000 K [6]) of most waste heat recovery applications is generally not high enough to generate sufficient photon flux and shift the peak wavelength to higher energies [6], resulting in modest power densities (i.e., less than 0.2 W/cm^2 at 900 K [29]). However, by reducing the separation between the hot radiator and the PV cell, such that the two bodies are in the near-field regime, the radiative heat flux can be substantially increased beyond the blackbody limit, leading to a significant improvement in the performance of the system.

Theoretical works [1–5] have shown that by utilizing evanescent coupling, both high efficiencies and power densities can be achieved, up to 40% and 11 W/cm^2 at 900 K [2]. Moreover, the performance of NFTPV systems can be further enhanced by relying on sur-

face modes. As discussed in Section 2.2.1, surface modes enable thermal emission in narrow spectral bands. In other words, these resonances can result in quasi-monochromatic radiative heat transfer [26, 55]. Therefore, if a NFTPV radiator can be tailored to support a surface mode that confines the radiative heat transfer in a spectral distribution just above the bandgap of the PV cell, remarkably high conversion efficiencies and power densities can be achieved, up to 60% and 96 W/cm^2 at 1200 K [4].

As discussed in Chapter 1, NFTPV technology requires highly specialized PV cells. Planck's distribution indicates that the radiator temperature in waste heat recovery applications ($<$ 1000 K [6]) is generally too low to generate sufficient photon flux above the bandgap of a conventional Si PV cell (i.e., 1.12 eV). As a result, conventional Si PV cells are unsuitable for NFTPV since they would yield poor conversion efficiency and power density, as most of the thermal radiation reaching the PV cell would have insufficient energy to excite electron-hole pairs. Therefore, NFTPV systems require specialized narrow bandgap PV cells. Nonetheless, simply having narrow bandgap PV cells is insufficient; NFTPV applications also demand room temperature operation. Although ultra narrow bandgap PV cells, such as InSb (with $E_g = 0.17$ eV), offer great potential for high efficiency energy conversion, these devices have such narrow bandgaps that room-temperature thermal energy can easily excite electrons across the bandgap. This parasitic excitation increases both noise level and dark current, deteriorating the performance of the device [53]. Consequently, these devices require impractical liquid nitrogen cooling, making them unsuitable for NFTPV applications. InAs stands out as a more suitable alternative for the temperature range of waste recovery applications [2, 59, 78] due to its bandgap (0.35 eV), which is well aligned with the Planck spectrum.

In addition to tailored bandgaps, NFTPV systems also benefit from thinner PV cells, which enhance the carrier collection efficiency and limit parasitic free carrier absorption [78]. Even for low-bandgap material such as InAs, the blackbody distribution at waste heat recovery temperatures ($<$ 1000 K [6]) indicates that most photons fall below the

bandgap. Therefore, a key challenge in achieving high efficiencies in NFTPV systems is reducing parasitic subgap absorption [58, 59, 78], as it does not produce electron-hole pairs but increases the internal temperature of the device, degrading performance [59, 76] or increasing cooling requirements. Tuning the spectral emission of the radiator could significantly reduce subgap absorption, however, very little work has been reported on optimized radiators in the field. Alternatively, theoretical studies have demonstrated that replacing the PV cell substrate, in which most of the subgap absorption occurs [78], with a broadband back reflector could significantly improve performance [78, 105]. The main purpose of the substrate is to provide mechanical support [99], and, therefore, it is not crucial to the device's performance. As a result, it can be replaced with a broadband back reflector without compromising functionality.

2.4 Dielectric Functions

The dielectric function of a material describes its response to an electromagnetic field; it is therefore of great importance in NFRHT modeling. The dielectric function ε is represented as a complex-valued function

$$\varepsilon(\omega) = \varepsilon'(\omega) + i\varepsilon''(\omega). \tag{2.22}$$

The modeling of the dielectric function strongly depends on the properties of the material. There are three mechanisms that contribute to the dielectric function: intraband transitions, lattice vibrations, and interband transitions. We address these mechanisms in Sections 2.4.1, 2.4.2, and 2.4.3, respectively. Additionally, we cover the dielectric function of semiconductors, in Section 2.4.4. Finally, in Section 2.4.5, we discuss the dielectric models of various materials employed in this work.

2.4.1 Intraband Absorption

The intraband contribution involves the excitation of an electron to another state within either the valence or conduction band. When a medium is exposed to an electromagnetic field, the field can interact with electrons in the medium and impart energy to them, causing electrons to oscillate about their equilibrium position. In the atomic structure, electrons behave as though they are bound to the nuclei by an elastic force. The larger nuclei are considered stationary as they are unable to respond to the rapid fluctuations in electromagnetic waves of the optical spectrum. As an electromagnetic field excites an electron, some of the energy transmitted to the electron is dissipated through radiative processes (i.e., emission of photons from excited electrons) or collisions with neighbouring particles (i.e., including interactions with phonons) [83, 106]. Therefore, the behavior of excited electrons can be modeled as damped harmonic oscillators, with a frictional force proportional to velocity [106]. The equation of motion for an electron exposed to an electric field $\overrightarrow{\mathbf{E}}$, as depicted in Fig. 2.8, is given by

$$m_0 \frac{\mathrm{d}^2 \overrightarrow{\mathbf{r}}}{\mathrm{d}t^2} + m_0 \gamma \frac{\mathrm{d}\overrightarrow{\mathbf{r}}}{\mathrm{d}t} + K\overrightarrow{\mathbf{r}} = -e\overrightarrow{\mathbf{E}}, \tag{2.23}$$

where m_0 is the electronic mass [9.109×10^{-31} kg], $\overrightarrow{\mathbf{r}}$ is the displacement of the charge from the rest position, γ is the damping coefficient, K is the effective spring constant, and e is the elementary charge [1.6022×10^{-19} C].

The dielectric function ε of a material is determined from the polarization $\overrightarrow{\mathbf{P}}$, which, in this context, is given by the sum of dipole moments [83]

$$\overrightarrow{\mathbf{P}} = -N_{\mathrm{dip}} e \overrightarrow{\mathbf{r}}, \tag{2.24}$$

where N_{dip} is the number of elementary dipoles per unit volume. The microscopic dipoles generally align with the field direction, causing the polarization vector to be parallel to $\overrightarrow{\mathbf{E}}$. This allows to express the polarization as a function of $\overrightarrow{\mathbf{E}}$

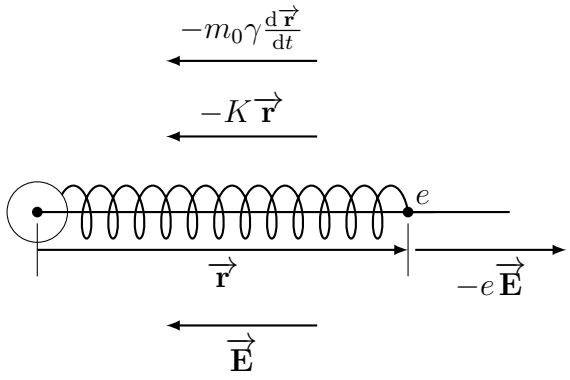

Figure 2.8: Representation of the forces acting on a bound electron when an electric field is applied (similar to Fig. 1 of Chapter 25 of Ref. 83).

$$\vec{\mathbf{P}} = \varepsilon_0 \chi \vec{\mathbf{E}}, \tag{2.25}$$

where χ is the electric susceptibility [106]. The electric displacement $\vec{\mathbf{D}}$ of the medium is determined by the electric field $\vec{\mathbf{E}}$ and polarization $\vec{\mathbf{P}}$

$$\vec{\mathbf{D}} = \varepsilon_0 \vec{\mathbf{E}} + \vec{\mathbf{P}}. \tag{2.26}$$

Therefore, one can write

$$\vec{\mathbf{D}} = \varepsilon_0 \left(1 + \chi\right) \vec{\mathbf{E}}. \tag{2.27}$$

Alternatively, the electric displacement can also be written in terms of the dielectric function

$$\vec{\mathbf{D}} = \varepsilon_0 \varepsilon \vec{\mathbf{E}}. \tag{2.28}$$

Consequently, the dielectric function can be expressed as a function of the electric susceptibility [106]

$$\varepsilon = 1 + \chi. \tag{2.29}$$

In some materials the dielectric function in the high-frequency limit does not converge to 1. In such cases, Eq. 2.29 must be modified to include a high-frequency dielectric constant ε_∞ [107]

$$\varepsilon = \varepsilon_\infty + \chi. \tag{2.30}$$

Employing the relations given in Eqs. 2.23, 2.24, 2.25, and 2.30, one can derive the Lorentz model [106] given by

$$\varepsilon(\omega) = \varepsilon_\infty \left(1 + \frac{N_{\text{dip}} e^2}{\varepsilon_0 \varepsilon_\infty m_0} \sum_{j=1}^{m} \frac{f_j}{\omega_j^2 - \omega^2 - i\omega\gamma_j}\right), \tag{2.31}$$

where m represents the total number of Lorentzian oscillators, each characterized by its respective damping coefficient γ_j, resonant frequency ω_j, and oscillator strength f_j. The sum in equation Eq. 2.31 arises from the presence of multiple oscillators with distinct resonant frequencies within an optical medium [106]. The Lorentz model accurately describes the intraband contribution of materials where bound electrons play a predominant role, such as in insulating materials.

In the case of free electrons, since they are not bound to any atoms, they do not experience any restoring forces. The dipole oscillator model, described in Eq. 2.23, is still valid in this case, however, we must set $K = 0$ [106]. For such a case, the derivation results in the Drude model

$$\varepsilon(\omega) = \varepsilon_\infty \left(1 - \frac{\omega_{\text{p}}^2}{\omega\left(\omega + i\gamma_{\text{F}}\right)}\right), \tag{2.32}$$

where γ_{F} is the free carrier damping coefficient and ω_{p} denotes the plasma frequency given by

$$\omega_{\mathrm{p}} = \sqrt{\frac{Ne^2}{\varepsilon_0 \varepsilon_\infty m_{\mathrm{e}}^*}}, \tag{2.33}$$

where N is the carrier density and m_{e}^* represents the electron effective mass. Even though there are bound electrons in conducting materials such as metals, the presence of a large number of free carriers allows their contribution to greatly dominate. Consequently, the dielectric function of metals is often effectively described by the Drude model [108]. Note that, by simply adjusting the effective mass and damping coefficient, the Drude model can also effectively characterize the behavior of holes in semiconductors [106, 109].

One can combine the Drude and the Lorentz model to form the Drude-Lorentz, incorporating contributions from both free carriers and bound electrons

$$\varepsilon(\omega) = \varepsilon_\infty \left(1 - \frac{\omega_{\mathrm{p}}^2}{\omega\left(\omega + i\gamma_{\mathrm{F}}\right)} + \frac{N_{\mathrm{dip}} e^2}{\varepsilon_0 \varepsilon_\infty m_0} \sum_{j=1}^{m} \frac{f_j}{\omega_j^2 - \omega^2 - i\omega\gamma_j} \right). \tag{2.34}$$

This model accurately describes the behavior observed in intraband transitions within materials where both the contributions from free carriers and bound electrons are substantial. Note that the parameters in Eq. 2.34 are generally chosen to match experimental data to ensure an accurate representation of the material's optical properties.

2.4.2 Lattice Absorption

Lattice absorption arises from interactions with the vibrational modes of a material's lattice structure. As discussed in Section 2.4.1, the nuclei are too massive to respond to the rapid fluctuations in electromagnetic waves of the optical spectrum. However, in the infrared spectral region, slower fluctuations can cause ions to vibrate with respect to their equilibrium position [110]. In a solid, atoms are bound to their equilibrium positions by the cohesive forces that maintain the crystal structure. When displaced from their equilibrium positions, atoms experience a restoring force and vibrate at characteristic frequencies determined by the phonon modes (i.e., vibrational modes of atoms in a lattice)

of the crystal. Therefore, vibrations of charged atoms within the lattice generate an oscillating dipole moment, in exactly the same way as the oscillations of bound electrons. Consequently, the main optical properties of phonons can be explained to a large extent by the classical dipole oscillator model discussed in Section 2.4.1 [106].

Electromagnetic waves can only interact with charged atoms, therefore, lattice absorption is only relevant in crystals that exhibit some ionic character. The key question is whether the oscillations of neighbouring atoms toward and away from each other, as seen with phonons, generate an oscillating dipole. This is clearly the case in ionic crystals. However, for covalent materials, polarity must be considered. In polar covalent crystals, electrons are not shared equally, leading to an uneven charge distribution, enabling dipole oscillations. Therefore, lattice absorption is only negligible in non-polar covalent crystals, where the structure consists of neutrally charged atoms equally sharing electrons between neighbouring nuclei [106].

Phonons can be classified as either acoustic or optical based on the behavior of atoms in the crystal lattice, and as longitudinal or transverse depending on the direction of the atomic oscillation with respect to the direction of the wave propagation. In the case of interaction with light, optical phonons typically play a more significant role in polar materials, while acoustic phonons primarly contribute to scattering processes in non-polar materials [106]. However, only optical phonons can directly interact with light, as the in-phase motion of atoms in acoustic phonons does not produce a significant dipole moment [111]. Additionally, as electromagnetic waves are transverse, they only exert driving forces to the transverse vibrations of the crystal, consequently, they can only couple to transverse optical (TO) phonons. These TO phonons exclusively absorb light at their resonant frequency, therefore, only photons of specific wavelengths can be absorbed by the lattice and generate a TO phonon [106].

From the classical dipole oscillator model one can derive a formula for the contribution of lattice vibrations which takes a very similar form to the Lorentz model [112]

$$\varepsilon(\omega) = \varepsilon_\infty \left(1 + \sum_{j=1}^{M} \frac{f_{\mathrm{P},j}\omega_{\mathrm{TO},j}^2}{\omega_{\mathrm{TO},j}^2 - \omega^2 - i\omega\gamma_{\mathrm{P},j}}\right), \tag{2.35}$$

where M represents the total number of phonon modes, each characterized by its respective damping coefficient $\gamma_{\mathrm{P},j}$, TO phonon resonant frequency $\omega_{\mathrm{TO},j}$, and oscillator strength $f_{\mathrm{P},j}$. The sum in equation Eq. 2.35 arises from the presence of multiple TO phonon modes with distinct resonant frequencies within an optical medium [112].

Combining the Lyddane-Sachs-Teller relationship with Eq. 2.35, one can remove the oscillator strength in favour of the more easily measured and predicted longitudinal optical (LO) phonon resonant frequency $\omega_{\mathrm{LO},j}$ [106]. The Lyddane-Sachs-Teller relationship provides a relation between the LO and TO phonon frequencies in an ionic crystal through the dielectric constants [112]

$$\frac{\varepsilon\,(0)}{\varepsilon_\infty} = \prod_{j=1}^{M} \frac{\omega_{\mathrm{LO},j}^2}{\omega_{\mathrm{TO},j}^2}. \tag{2.36}$$

Thus, Eq. 2.35 simplifies to

$$\varepsilon(\omega) = \varepsilon_\infty \left(1 + \sum_{j=1}^{M} \frac{\omega_{\mathrm{LO},j}^2 - \omega_{\mathrm{TO},j}^2}{\omega_{\mathrm{TO},j}^2 - \omega^2 - i\omega\gamma_{\mathrm{P},j}}\right). \tag{2.37}$$

Here, LO phonons play a role in the dielectric response since the medium can support longitudinal waves at frequencies where the complex dielectric constant is null [106].

2.4.3 Interband Absorption

While lattice absorption typically only occurs in the infrared spectrum, intraband transitions persist at higher frequencies, however, interband transitions become increasingly significant at larger energy levels and may even become predominant in certain materials. Consequently, the distinction between insulators, which typically have low electrical conductivity due to their large bandgaps, and metals, which exhibit high conductivity due to their abundance of free electrons, begins to break down at higher fre-

quencies [113].

Interband absorption originates from the excitation of electrons from the valence band to an empty state in the conduction band. As explained in Section 2.3.1, the bandgap energy E_g of a material corresponds to the energy required to excite an electron from the valence band to the conduction band. Interband transition is, therefore, only possible whenever the photon energy exceeds the bandgap energy E_g of the material [107]. In the case of an interband transition, as illustrated in Fig. 2.9a, the energy of the final state in the conduction band E_f can be derived from the conservation of energy

$$E_f = E_i + \hbar\omega, \tag{2.38}$$

where E_i is the initial energy of the electron in the valence band.

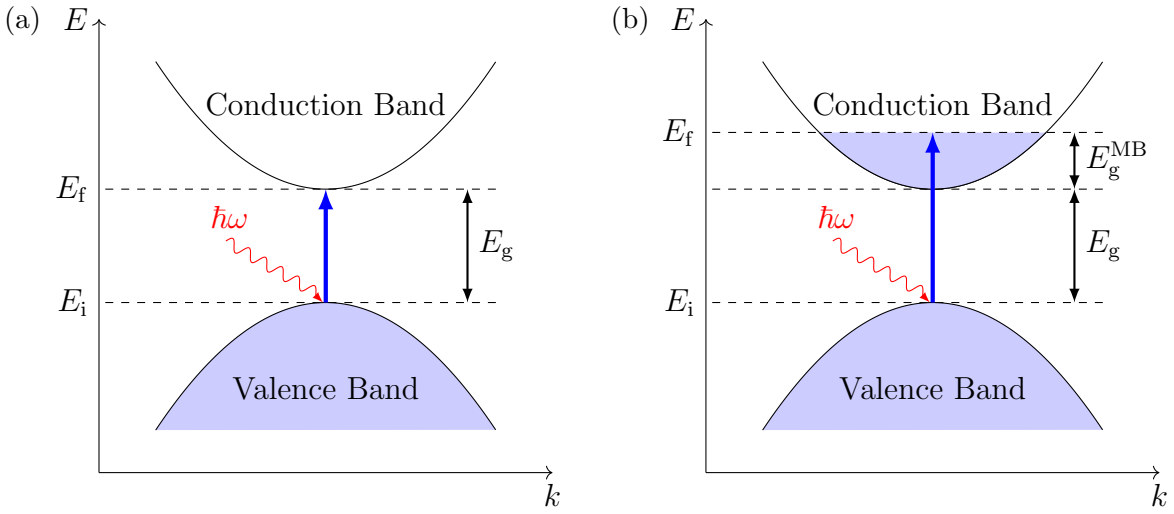

Figure 2.9: (a) Representation of the interband transition of an electron from its initial state in the valence band to an unoccupied state in the conduction band (similar to Fig. 4 of Ref. 114). (b) In the case of heavily n-doped semiconductors, additional electrons are introduced in the conduction band, filling up states near the band edge, resulting in a Moss-Burstein shift (similar to Fig. 3 of Ref. 115).

Interband transitions occur in all solids. In large bandgap materials, such as semiconductors and insulators, interband transitions are particularly significant as they occur at energies where free carrier effects are negligible. In contrast, in low or zero bandgap

materials, such as metals, interband transitions typically occur at frequencies where free carrier effects remain important [112]. Although they still play an important role in metals [106], the high free carrier density often causes interband transitions to be overshadowed by free carrier absorption [112].

The interband absorption coefficient α_{IB} quantifies the absorption of light through interband transitions in the material. This coefficient is directly linked to the imaginary part of the interband refractive index n''_{IB}

$$n''_{\mathrm{IB}}(\omega) = \frac{\alpha_{\mathrm{IB}}(\omega)c_0}{2\omega}. \tag{2.39}$$

Since the refractive index is a complex quantity, the real part of the interband refractive index n'_{IB} is also necessary to fully describe the optical response. This quantity can be determined from n''_{IB} using the Kramers-Kronig relations [106]

$$n'_{\mathrm{IB}}(\omega) = 1 + \frac{2}{\pi}\mathcal{P}\int_0^\infty \frac{\Omega n''_{\mathrm{IB}}(\Omega)}{\Omega^2 - \omega^2}\mathrm{d}\Omega, \tag{2.40}$$

where $\mathcal{P}$ denotes the Cauchy principal value of the integral. The interband dielectric function $\varepsilon_{\mathrm{IB}}$ can then be expressed as

$$\varepsilon_{\mathrm{IB}}(\omega) = \left(n'_{\mathrm{IB}}(\omega) + in''_{\mathrm{IB}}(\omega)\right)^2. \tag{2.41}$$

The interband dielectric function can be combined with the lattice and intraband contributions by summing the susceptibility from each contribution and only including the high-frequency dielectric constant once. This approach is further discussed in Section 2.4.4.

In the simplest case, the interband contribution can be modeled by considering only a discrete number of energy levels, while the neglected contributions are accounted for by the high-frequency dielectric constant [112]. In such case, the interband absorption coefficient can be found by computing the sum over all possible transitions. However, for

a more realistic description of the optical properties of the material, one must consider the distribution of energy levels as continuous [106]. In this scenario, the interband absorption coefficient is expressed as a relatively complex relation derived from the optical properties of the material.

Note that, as depicted in Fig. 2.9a, the conduction and valence bands are typically modeled as parabolic functions of the electron wavevector k. However, in reality, some regions of the conduction and valence bands deviate from a simple quadratic relationship between energy and momentum. For certain materials, these deviations are significant enough that the non-parabolic behavior must be considered in the interband absorption calculations [116].

Beyond a certain doping concentration, narrow bandgap materials experience a shift in the effective bandgap, as energy states near the band edges become occupied [117]. In a heavily n-doped semiconductor, additional electrons are introduced into the conduction band, filling up the states near the band edge, as depicted in Fig. 2.9b. This prevents optical absorption from the valence band to the conduction band at energy E_{g}, as the states at the bottom of the conduction band are already filled. As a result, the effective bandgap experienced by electrons is increased. The minimal photon energy required to induce interband transitions rises by $E_{\mathrm{g}}^{\mathrm{MB}}$, which corresponds to the energy difference between the conduction band edge and its lowest unoccupied state. Consequently, the interband absorption is shifted to higher energies as the doping concentration increases [115]. This phenomenon, known as the Moss-Burstein shift [118], can be modeled by incorporating a scaling factor for the interband absorption within the dielectric model. The approach employed to determine this shift may vary depending on the specific properties and characteristics of the material. This phenomenon is similarly observed in heavily p-doped semiconductors, in which the surplus of holes results in unoccupied states in the valence band, causing a shift in the effective bandgap [119]. However, the Moss-Burstein effect is primarily of interest in n-type semiconductors [120].

2.4.4 Semiconductors

The intrinsic optical properties of semiconductors are governed by the three fundamental physical mechanisms: lattice vibrations, interband transitions, and the influence of free carriers [116], which we discussed in Sections 2.4.1–2.4.3. Therefore, the dielectric function of semiconductors can be estimated by combining the interband dielectric function with the Drude model and the lattice vibration contribution model detailed in Eq. 2.37. One can combine these models by summing the susceptibility from each contribution, given by

$$\chi_{\mathrm{FC}}(\omega) = \varepsilon_{\infty}\left(-\frac{\omega_{\mathrm{p}}^{2}}{\omega\left(\omega + i\gamma_{\mathrm{F}}\right)}\right), \tag{2.42}$$

$$\chi_{\mathrm{Lattice}}(\omega) = \varepsilon_{\infty}\left(\frac{\omega_{\mathrm{LO}}^{2} - \omega_{\mathrm{TO}}^{2}}{\omega_{\mathrm{TO}}^{2} - \omega^{2} - i\omega\gamma_{\mathrm{P}}}\right), \tag{2.43}$$

$$\chi_{\mathrm{IB}}(\omega) = \varepsilon_{\mathrm{IB}}(\omega) - \varepsilon_{\infty}, \tag{2.44}$$

where χ_{FC} is the susceptibility due to free carrier absorption, χ_{Lattice} is the susceptibility due to lattice vibrations, and χ_{IB} is the susceptibility due to interband transitions. Here, ω_{LO} and ω_{TO} are, respectively, the longitudinal and transverse optical phonon frequencies and γ_{P} is the phononic damping coefficient. Note that, in Eq. 2.43, there is no summation over the phonon modes, as the single harmonic oscillator model can adequately describe the optical properties of semiinsulating crystals in the Reststrahlen region (i.e., region of high reflectivity and strong absorption that lies between the TO and LO phonon frequencies of a polar crystal) [116]. Therefore, the total dielectric function is given by

$$\varepsilon(\omega) = \varepsilon_{\infty} + \chi_{\mathrm{FC}}(\omega) + \chi_{\mathrm{Lattice}}(\omega) + \chi_{\mathrm{IB}}(\omega). \tag{2.45}$$

2.4.5 Employed Dielectric Models

In this section, we elaborate on the dielectric models of various materials employed in this work. We discuss the dielectric function of InAs in Section 2.4.5.1, that of Si in Section 2.4.5.2, that of SiN in Section 2.4.5.3, and that of SiO_2 in 2.4.5.4.

2.4.5.1 Indium Arsenide

The dielectric function of InAs is based on the model described in Ref. 117, with a few modifications to improve both accuracy and computational speed. Firstly, the model has been modified to correct for the overestimation of free carrier absorption, which is discussed later in this section. Secondly, the model employs the updated parameters from Ref. 78. Finally, instead of calculating the real part of the interband refractive index n'_{IB} using the Kramers-Kronig relations, as done in Ref. 117, the model approximates $n'_{\mathrm{IB}} = \sqrt{\varepsilon_\infty}$, following the approach of Ref. 78, to improve the computational speed. The impact of this approximation is shown to be negligible in Ref. 78 and is subsequently verified within the scope of Objective 4.

Given that the bandgap of InAs (0.35 eV) lies in the infrared spectrum, the interband contribution must be taken into consideration. The interband absorption model considers a continuous distribution of energy levels. The model also includes a non-parabolicity correction taken from Ref. 121, since both the valence and conduction band of InAs deviate significantly from a simple quadratic relationship. Given that InAs has a relatively low bandgap, a Moss-Burstein shift model, taken from Ref. 120, is also included.

Since InAs is a III-V semiconductor, the shared electrons lie slightly closer to the Group V atoms than the Group III atoms, giving the bond a partially ionic character [106]. Hence, due to its polar character, it is imperative to consider the contributions from both lattice vibrations and free carriers, in addition to the interband contribution. Therefore, the model described in Ref. 117 takes the form of Eq. 2.45.

A comparison with InAs absorption data, taken from Ref. 122, uncovered an overes-

timation of free carrier absorption in the dielectric function described in Ref. 117. More precisely, this comparison, available in Chapter 6 (Fig. 6.1a), demonstrates that the traditional Drude model significantly overestimates free carrier absorption in InAs at energies near the bandgap. Such overestimation could lead to inaccurate predictions of NFTPV performances since above-bandgap absorptivity originating from free carrier absorption does not generate collectible electron-hole pairs. Additionally, parasitic subgap heating could have a considerable effect on the overall performance of the device. Therefore, we address this overestimation by incorporating an alternative model, described in Ref. 123, derived from ionized impurity scattering. This model substitutes the imaginary component of the Drude model, in the case of highly n-doped InAs, for frequencies exceeding the plasma frequency. Further discussions of this modification can be found in Chapter 6. The resulting dielectric function is shown in Fig. 2.10 for the case of n-doped InAs at 300 K with a doping level of $N_{\mathrm{d}} = 5 \times 10^{17}$ cm^{-3}. Note that the resonance located just below 0.03 eV arises from a phonon resonance.

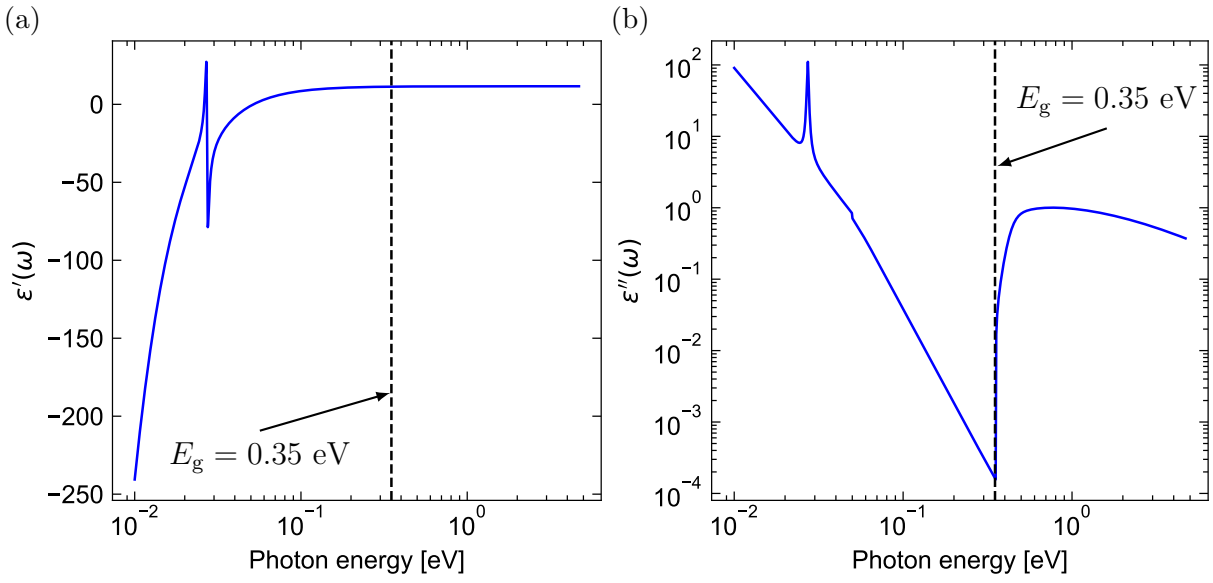

Figure 2.10: (a) Real and (b) imaginary part of the dielectric function of n-doped InAs at 300 K and $N_{\mathrm{d}} = 5 \times 10^{17}$ cm^{-3}.

2.4.5.2 Silicon

The model used for the dielectric function of Si is a combination of the work described in Refs. 109, 124, 125, and 126. The free carrier contribution is approximated by a Drude model described in Ref. 109 while using the model described in Ref. 124 to compute the mobility, decay rates, and donor and acceptor contributions. On the other hand, the interband and lattice vibrations contributions are accounted for by the model described in Ref. 125, in which the interband absorption is approximated by a semi-empirical discrete energy levels model described in Ref. 126. In the case of Si, lattice vibrations contribute very little to the dielectric function due to the weakness of the phonon oscillators [109], resulting from the non-polar covalent nature of the structure [106]. The resulting dielectric function is shown in Fig. 2.11 for the case of p-doped Si at 300 K and $N_{\mathrm{d}} = 5 \times 10^{19}$ cm^{-3}.

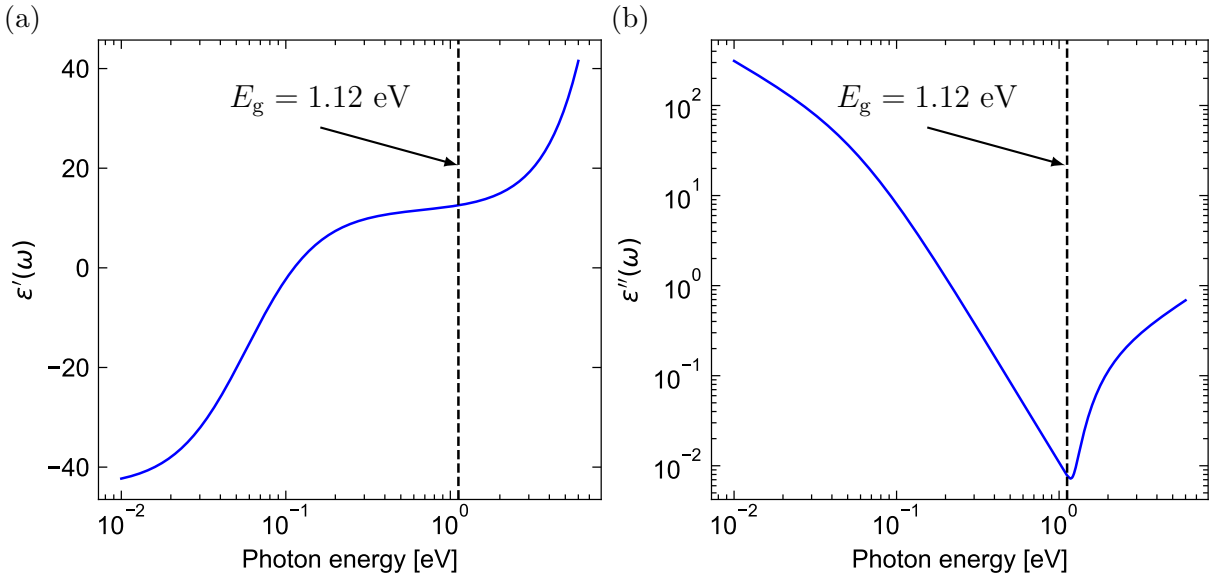

Figure 2.11: (a) Real and (b) imaginary part of the dielectric function of p-doped Si at 300 K and $N_{\mathrm{d}} = 5 \times 10^{19}$ cm^{-3}.

2.4.5.3 Silicon Nitride

The dielectric function of SiN is approximated by the model described in Ref. 127. As we focus solely on the infrared spectrum, excluding the interband contribution is

adequate here, given that SiN possesses a large bandgap (ranging from 2.09 to 4.56 eV, depending on the NH_3/SiH_4 ratio [128]) located beyond the infrared range. In this case, we only consider intrinsic SiN, rendering the free carrier contribution insignificant. As in the case of InAs, the bonds in the SiN structure are partially ionic, which implies that the contribution of lattice vibrations must be considered. Consequently, the dielectric function of SiN is effectively represented by the classical oscillator model detailed in Eq. 2.35. The resulting dielectric function of SiN is shown in Fig. 2.12.

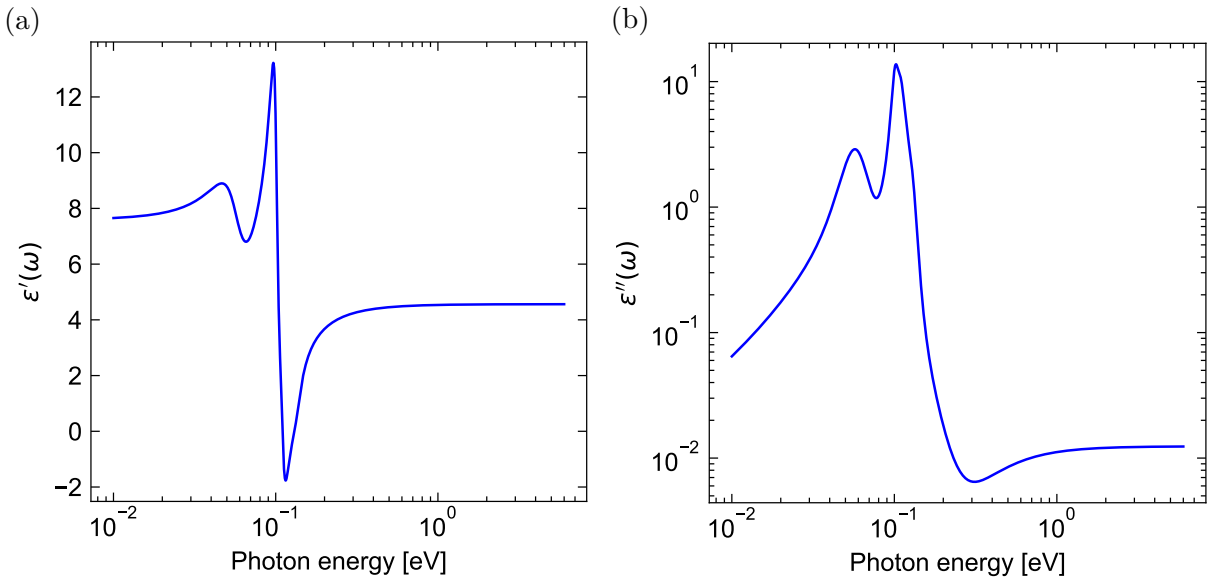

Figure 2.12: (a) Real and (b) imaginary part of the dielectric function of SiN.

2.4.5.4 Silicon Dioxide

The dielectric function of SiO_2, employed in Chapter 4 to simulate a BK7 lens, is modeled by curve-fitting the data from Ref. 129 obtained from silica glass samples of various types. The resulting dielectric function of SiO_2 is shown in Fig. 2.13.

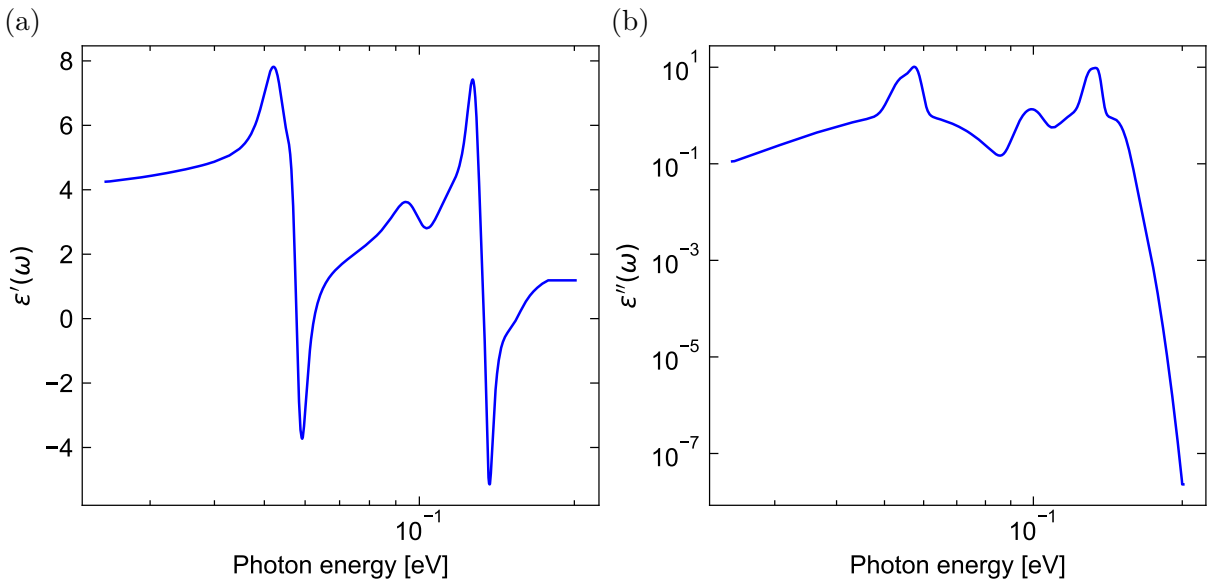

Figure 2.13: (a) Real and (b) imaginary part of the dielectric function of SiO_2.

2.5 Nanomechanical Resonators

Nanomechanical resonators are described as continuous mechanical structures, such as beams, strings, plates, or membranes, that vibrate at a specific frequency when excited by an external source. SiN membranes are a very versatile subcategory of nanomechanical resonators used in many applications, including nanomaterials [130] and optomechanics research [131–133]. These membranes have recently attracted a lot of attention in the field of thermal-radiation sensing. The sharp resonance of the mechanical modes of these resonators enables high resolution radiation sensing [69, 75]. When exposed to radiation, thermal expansion induces stress relaxation, resulting in a shift of the mechanical resonance frequency. The temperature shift of the membrane (proportional to absorbed radiation) can be inferred in real-time by measuring this shift in the resonance frequency using a fiber interferometer [134]. Similarly, these resonators are also employed to measure forces [135], as the application of a force induces additional stress in the membrane, resulting in a shift of the mechanical resonance frequency.

The projected frequency shift Δf can be approximated from the average temperature

change $\Delta\overline{T_{\mathrm{m}}}$ of the resonator using Eq. 2.46 [73].

$$\Delta f = -\frac{\alpha E f_0}{2\sigma_0 (1-\nu)} \Delta\overline{T_{\mathrm{m}}}, \tag{2.46}$$

where α is the thermal expansion coefficient of SiN, E is the Young modulus, f_0 is the resonance frequency of the membrane at room temperature, σ_0 is the temperature-independent component of the in-plane stress, and ν is the Poisson ratio. Unfortunately, this relation is only valid under non-localized heating. When localized effects take place, such as localized absorption, conduction-dominated conditions, or large temperature variations, this approximation can lead to up to 40% error [66, 136]. As shown in Ref. 66, the radiative thermal coupling properties of square membranes of side length L are well approximated by that of circular membranes of effective radius $r_{\mathrm{eff}} = 1.252\frac{L}{2}$. Therefore, to account for the non-uniform temperature distribution, we can numerically solve the motion equation in polar coordinates for a thin membrane under tensile stress [137]

$$\frac{1}{r}\frac{\partial}{\partial r}\left(\left(\sigma_0 + \sigma_r\left(r, T_{\mathrm{m}}\left(r\right)\right)\right) r \frac{\partial u(r,t)}{\partial r}\right) - \rho\frac{\partial^2 u(r,t)}{\partial t^2} = 0, \tag{2.47}$$

where $\sigma_r(r, T_{\mathrm{m}})$ is the position-dependent component of the in-plane stress, ρ is the density of SiN, and $u(r,t)$ represents the out-of-plane displacement of the membrane. The position-dependent component of the in-plane stress (σ_r) is given as a function of the temperature profile [138]

$$\sigma_r(r, T_{\mathrm{m}}) = -\alpha E\left[\frac{1}{r^2}\int_0^r r\Delta T_{\mathrm{m}}(r)\mathrm{d}r + \frac{1+\nu}{1-\nu}\frac{\Delta\overline{T_{\mathrm{m}}}}{2}\right], \tag{2.48}$$

where $\Delta T_{\mathrm{m}} = T_{\mathrm{m}} - T_{\infty}$.

Our research group's expertise lies in the field of nanomechanical resonators. More precisely, our group has published on infrared [66, 139] and terahertz [75] radiation sensing using SiN membranes, as well as on investigating fluctuation noise [67, 140] within SiN membranes. Given our expertise on these devices, we have opted to use these resonators

as a tool for NFRHT sensing. Additionally, since nanomechanical resonators allow to measure both temperature and forces simultaneously, they could offer the opportunity to investigate many new phenomena occurring between two objects at sub-wavelength distances.

2.6 Casimir Forces

Casimir forces, predicted in 1948 by Casimir and Polder [141], are attractive forces occurring between closely spaced conducting surfaces, attributed to the presence of electromagnetic modes in the cavity. The two surfaces act like mirrors, reflecting the virtual photons filling the "empty" cavity [142]. Therefore, the cavity restricts the wavelengths of virtual photons that can be supported to discrete values. As in the case of a laser cavity, only standing waves with half-wavelengths that can "fit" an integer number of times in the gap between the two surfaces can exist in the cavity [89]. If this condition is not respected, after a few reflections, photons of the same wavelength are no longer in-phase, and destructive interference occurs [83]. As the thickness of the cavity decreases, the number of electromagnetic modes decreases, and therefore the electromagnetic energy decreases. Consequently, more virtual photons are present in the area outside the cavity than in the cavity itself, resulting in an attractive force between the two plates [89].

The first experimental demonstration of the Casimir forces was performed in 1958 by Sparnaay [143]. Since then, a few dozen experimental measurements of the Casimir forces have been reported [144]. Measurement platforms typically employ sensitive force transducers, such as micro-cantilevers or micro-electromechanical systems (MEMS), like the SiN nanomechanical resonators [135] used in this work.

In 1956, Lifshitz [145] extended the original Casimir force model to simulate real materials by means of the fluctuation-dissipation theorem. While the Lifshitz theory remains the most advanced, it is formulated for systems at thermal equilibrium. Some theoretical studies [22, 146, 147] have explored corrections to Casimir forces out of thermal

equilibrium. However, only one experimental demonstration of the thermal effects of the Casimir-Lifshitz interaction has been reported [148]. This work could only provide measurements at large distances ($\sim 10\,\mu\text{m}$), where the thermal component predominates.

In this work, we adopt the theoretical framework from Ref. 146 to model the Casimir forces, incorporating both equilibrium and nonequilibrium thermal effects. This model evaluates the total pressure acting between two planar semi-infinite bodies (media 1 and 3) separated by a vacuum gap (medium 2), in a configuration similar to Fig. 2.5. The total pressure due to Casimir forces is expressed as the sum of contributions from zero-point ($T = 0$) fluctuations $P_0(d)$ and thermal fluctuations $P_{\text{th}}^{\text{neq}}(T_1, T_3, d)$

$$P^{\text{neq}}(T_1, T_3, d) = P_0(d) + P_{\text{th}}^{\text{neq}}(T_1, T_3, d). \tag{2.49}$$

The zero-point fluctuations contribution is given by

$$P_0(d) = \frac{\hbar}{2\pi^2 c^3} \int_0^\infty \int_1^\infty p^2 \xi^3 \sum_{\gamma=\text{TE,TM}} \frac{r_{21}^\gamma r_{23}^\gamma e^{2ik_z d}}{1 - r_{21}^\gamma r_{23}^\gamma e^{2ik_z d}} \text{d}p\text{d}\xi, \tag{2.50}$$

where ξ denotes the imaginary angular frequency and $p = \sqrt{1 + c^2 k_\rho^2/\xi^2}$. The Fresnel reflection coefficients r_{21}^γ and r_{23}^γ are computed using Eqs. 2.16 and 2.17.

The thermal pressure under nonequilibrium conditions is expressed as the sum of two terms, each corresponding to a configuration where only one of the two materials is at nonzero temperature

$$P_{\text{th}}^{\text{neq}}(T_1, T_3, d) = P_{\text{th}}^{\text{neq}}(T_1, 0, d) + P_{\text{th}}^{\text{neq}}(0, T_3, d). \tag{2.51}$$

Each term can be expressed as a function of the equilibrium thermal pressure $P_{\text{th}}^{\text{eq}}(T, d)$ and an asymmetric component $\Delta P_{\text{th}}(T, d)$

$$P_{\text{th}}^{\text{neq}}(T, 0, d) = P_{\text{th}}^{\text{eq}}(T, d)/2 + \Delta P_{\text{th}}(T, d), \tag{2.52}$$

$$P_{\rm th}^{\rm neq}(0,T,d) = P_{\rm th}^{\rm eq}(T,d)/2 - \Delta P_{\rm th}(T,d). \tag{2.53}$$

The Lifshitz pressure at thermal equilibrium $P_{\rm th}^{\rm eq}(T,d)$ is given by

$$P_{\rm th}^{\rm eq}(T,d) = \frac{k_{\rm B}T}{16\pi d^3}\int_0^\infty x^2\left[\frac{(\varepsilon_{10}+1)(\varepsilon_{30}+1)}{(\varepsilon_{10}-1)(\varepsilon_{30}-1)}e^x - 1\right]^{-1}{\rm d}x, \tag{2.54}$$

where $\varepsilon_{10} = \varepsilon_1(0)$ and $\varepsilon_{30} = \varepsilon_3(0)$ are the static dielectric constants of the materials. The quantity $\Delta P_{\rm th}(T,d)$ accounts for the nonequilibrium asymmetry and can be expressed as the sum of the contributions from the propagating $\Delta P_{\rm th}^{\rm prop}(T,d)$ and evanescent $\Delta P_{\rm th}^{\rm evan}(T,d)$ waves

$$\Delta P_{\rm th}(T,d) = \Delta P_{\rm th}^{\rm prop}(T,d) + \Delta P_{\rm th}^{\rm evan}(T,d). \tag{2.55}$$

The contribution from each mode is given by

$$\Delta P_{\rm th}^{\rm prop}(T,d) = -\frac{\hbar}{4\pi^2}\int_0^\infty \frac{1}{e^{\hbar\omega/k_{\rm B}T}-1}\int_0^{k_{\rm v}}\sum_{\gamma={\rm TE,TM}}\left(|r_{23}^\gamma|^2 - |r_{21}^\gamma|^2\right)$$
$$\left(\frac{1}{|1-r_{21}^\gamma r_{23}^\gamma e^{2ik_z d}|^2} - \frac{1}{1-|r_{21}^\gamma r_{23}^\gamma|^2}\right)k_z k_\rho {\rm d}k_\rho {\rm d}\omega, \tag{2.56}$$

$$\Delta P_{\rm th}^{\rm evan}(T,d) = \frac{\hbar}{2\pi^2}\int_0^\infty \frac{1}{e^{\hbar\omega/k_{\rm B}T}-1}\int_{k_{\rm v}}^\infty \sum_{\gamma={\rm TE,TM}}\frac{{\rm Im}\,(r_{21}^\gamma)\,{\rm Re}\,(r_{23}^\gamma) - {\rm Im}\,(r_{23}^\gamma)\,{\rm Re}\,(r_{21}^\gamma)}{|1-r_{21}^\gamma r_{23}^\gamma e^{2ik_z d}|^2}$$
$${\rm Im}\,(k_z)\,e^{-2d{\rm Im}(k_z)}k_\rho {\rm d}k_\rho {\rm d}\omega. \tag{2.57}$$

We employ this model in Section 4.2, using the Derjaguin approximation [97] to simulate Casimir forces between an optical lens and a SiN resonator.

3. Summary of Experimental Platforms and Outlook

In this chapter, we summarize the evolution of the experimental platforms developed in this work. Platforms 1 and 2, detailed in Sections 3.1 and 3.2, respectively, are employed for NFRHT measurements, discussed in Chapter 4. On the other hand, Platform 3, presented in Section 3.3, is used in an unsuccessful attempt to perform NFTPV measurements, described in Chapter 5. Finally, Platform 4, outlined in Section 3.4, is proposed in Chapter 5 as an alternative to address the limitations encountered with Platform 3. Note that the content of this chapter is further discussed in later chapters (i.e., Chapters 4 and 5); this chapter serves as a summary of the experimental platforms.

3.1 Platform 1: 1-axis Near-Field Radiative Heat Transfer Measurement with SiN Resonators

Platform 1, shown in Fig. 3.1, represents the first iteration of our NFRHT platform, employed to achieve Objectives 1 and 2, as discussed in Chapter 4. More specifically, this platform is employed to study NFRHT between a heated glass half sphere and a SiN membrane. Platform 1 was designed with an emphasis on flexibility to facilitate experimental testing of new materials for NFRHT. One of the key advantages of Platform 1, as opposed to most NFRHT platforms, is that it relies entirely on standard components that are commercially available.

In Platform 1, we employ SiN membranes as our sensing element. Such membranes are routinely used in nanomaterials [130] and optomechanics research [131–133] and are commercially available from multiple suppliers. Here, employing nanomechanical resonators

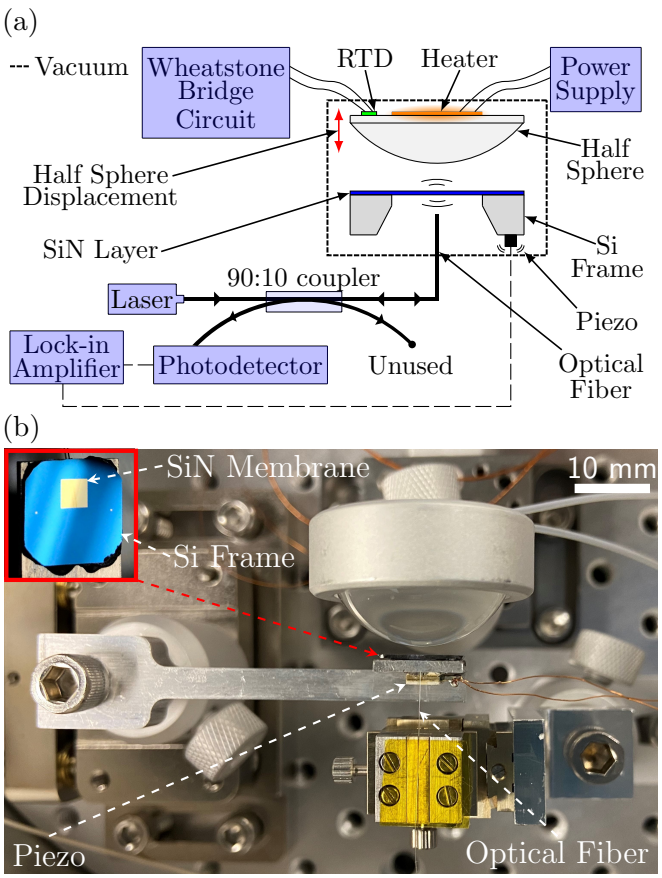

Figure 3.1: (a) Schematic and (b) photograph of Platform 1. This figure is a reproduction of Figs. 4.1a and 4.1b.

as our sensing element further differentiates Platform 1 from other NFRHT platforms. Unlike most NFRHT platforms, where the use of custom devices complicates the testing of new materials, this platform could facilitate the exploration of many new interesting materials for NFRHT, given that materials are routinely deposited on nanomechanical resonators. We also demonstrate in Ref. 136 that nanomechanical resonators enable a temperature resolution (i.e., 1.2×10^{-6} K) unparalleled in previous NFRHT experiments.

The temperature of the membrane is measured in real-time with an optical fiber interferometer [134] (see Fig. 3.1a), by measuring the shift of its mechanical resonance frequency due to thermal expansion [139, 149]. To suppress fluidic damping and convective heat transfer, the platform is positioned in a custom-designed high vacuum chamber operating at a typical pressure of 2×10^{-6} Torr. The membrane used for the experiment

is made of low stress SiN (built-in stress $\sim 100\,\mathrm{MPa}$) with a nominal dimension of 3 mm in side length and $t_{\mathrm{SiN}} = 100$ nm thickness. The membrane was fabricated in-house, but similar devices are commercially available. The Si frame of the membrane is mounted on an aluminum support (see Fig. 3.1b) using nickel paste (Pelco®), enabling good thermal conduction for maintaining the frame at room temperature. A piece of piezoelectric ceramic (Thorlabs shear piezoelectric chip), mounted on the back of the aluminum support, is used to drive the membrane at its resonance frequency.

As illustrated in Fig. 3.1a, our experimental approach uses a glass half sphere as a hot surface (Thorlabs BK7 lens, 12.7 mm radius) onto which a metal-ceramic heater is attached. The half sphere is used to simplify the alignment procedure, allowing the use of a single-axis positioner. The half sphere is brought closer to the SiN membrane using a vacuum positioner actuated with an inertia drive (New Focus Picomotor™).

Unfortunately, as further discussed in Chapter 4, due to the limited alignment capability (i.e., one-axis alignment, 25 nm step size, open-loop control), we were unable to achieve measurements in the deep sub-wavelength regime (i.e., regime dominated by surface resonance coupling). Additionally, our theoretical analysis demonstrated that, at smaller distances, saturation of the membrane temperature and dilution of the near-field signal would limit the temperature shift observed in large resonators, such as the one employed in this platform ($L = 3$ mm).

3.2 Platform 2: 5-axis Near-Field Radiative Heat Transfer Measurement with SiN Resonators

Platform 2, shown in Fig. 3.2, represents the second iteration of our NFRHT platform, employed to achieve Objectives 1 and 2, as discussed in Chapter 4. This platform is an improved version of Platform 1, with enhanced alignment capability and refined geometries, enabling the full investigation of the potential of nanomechanical resonators for

NFRHT. Platform 2 not only enables the performance of deep sub-wavelength NFRHT measurements without requiring custom-fabricated micro-devices, but it also provides the opportunity to measure NFRHT and the Casimir effect simultaneously.

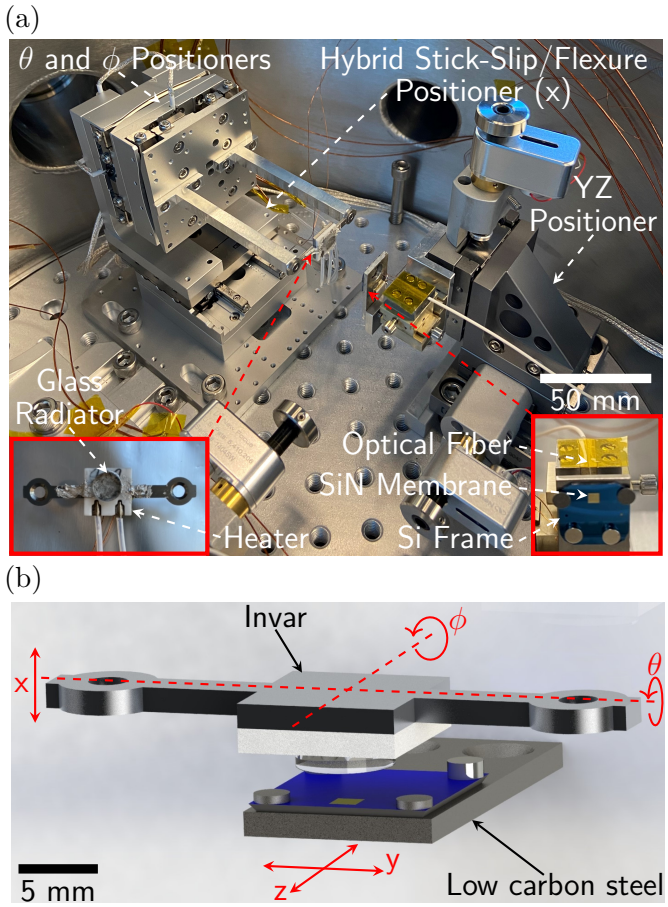

Figure 3.2: (a) Photograph of Platform 2 showing the resonator and radiator in a vertical orientation, and (b) render of Platform 2 in a horizontal configuration. This figure is a reproduction of Fig. 4.10.

In Platform 2, we replace the single-axis positioner employed in Platform 1 with a high-resolution 5-axis positioning system (see Fig. 3.2a), enabling the alignment of the two surfaces in the y, z, θ, and ϕ direction, as shown in Fig. 3.2b. The separation (x) between the two surfaces is controlled by a closed-loop hybrid linear stage (Smaract DLS-5252) that combines the advantage of long travel range (30 mm) stick-slip positioners and high-resolution piezo scanners, enabling a resolution of 1 nm over a 35 µm slip-free range. The y and z positions of the membrane can be modified using open-loop inertia

drives (New Focus Picomotor^{TM}) with 25 nm per step resolution. The θ and ϕ alignment is controlled by closed-loop stick-slip stages (Smaract SGO-60.5 and SGO-77.5), with $2\,\mu^{\circ}$ resolution. The use of a spherical radiator eliminates the need for the θ and ϕ alignment axes in the current experiment, although their use is possible in future plane-plane experiments.

Apart from the 5-axis positioning system, Platform 2 relies on the same components as Platform 1; however, some aspects have been optimized. The platform now features a smaller glass radiator (i.e., 6 mm radius) with a larger radius of curvature (15.5 mm). This geometry limits the parasitic heating of the environment while also increasing the effective near-field heat transfer area. The platform also relies on a smaller SiN membrane (i.e., 1.7 mm in side length) to limit the saturation and dilution effects observed with Platform 1 (see Fig. 5 of Ref.[136]). Additionally, the glass radiator and metal ceramic heater are now mounted on a custom-machined Invar plate, which, due to its low thermal conductivity and low thermal expansion coefficient compared to other metals, minimizes required heating power and mechanical deformation. Finally, the Si frame of the membrane is now mounted on a low carbon steel support (see Fig. 3.2b) using 4 magnets, enabling a good thermal contact for maintaining the Si frame at room temperature, while limiting the mechanical damping compared to adhesive mounting.

3.3 Platform 3: Unsuccessful Near-Field Thermophotovoltaic Measurement

Platform 3, shown in Fig. 3.3, represents the third iteration of our experimental platform, used in an attempt to achieve Objective 3, as discussed in Chapter 5. This platform is a modified version of Platform 2, adapted for NFTPV measurements. Platform 3 supports the integration of InAs cells and features a specialized Si radiator tailored for NFTPV measurements. While we now employ custom devices for the radiator, this

platform remains flexible as it enables the implementation of cells of various materials and geometries.

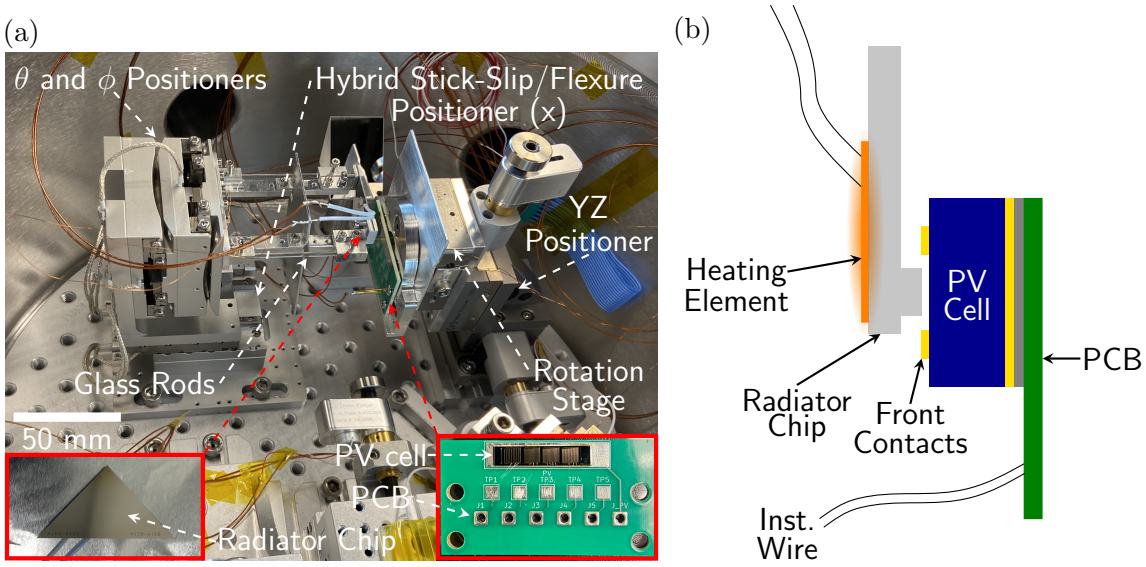

Figure 3.3: (a) Photograph and (b) illustration of Platform 3. This figure is a reproduction of Fig. 5.1.

Platform 3 relies on the same high-precision positioning system employed in Platform 2, but now allows integration of printed circuit boards (PCBs) on which the PV cells are mounted (see Fig. 3.3). Here, we employ InAs PV cells provided by Myles Steiner and Eric Tervo's team at the National Renewable Energy Laboratory (NREL). The PV cells are mounted on a PCB using silver epoxy (M.G. Chemicals Silver Conductive Epoxy Adhesive). The low curing temperature of this adhesive (i.e., 65 °C) minimizes the damage sustained by the cell during the mounting process. Additionally, the bond formed by this adhesive proved to be robust enough to withstand the pressure applied during wire bonding. An additional rotation stage (Thorlabs PDR1V) is introduced to enable the alignment of the front contact electrodes with the radiator chip.

As shown in Fig. 3.3, Platform 3 features a specialized Si radiator tailored for NFTPV measurements. This Si radiator consists of a triangular chip, where most of the substrate is etched (i.e., to a depth of $\sim 5\,\mu m$) via reactive ion etching (RIE), except for a small area of a few hundred microns. This unetched region will be strategically aligned with

the front contact electrodes of the PV cell and positioned to operate within the near-field of the cell, as shown in Fig. 3.3b. The etched area is coated with platinum to lower its emissivity, therefore, reducing the parasitic far-field radiation. The chip is heated by a metal ceramic heater attached to its back side using silver paste (PELCO® High Performance Silver Paste), as illustrated in Fig. 3.3b.

The performance of NFTPV measurements requires radiator temperatures (i.e., up to 700 K) that are significantly higher than those observed in Platforms 1 and 2 (i.e., below 400 K). Therefore, Platform 3 had to be adapted for higher temperature scans. Firstly, aluminum sheets, acting as heat shields, are placed in front of the positioners to minimize parasitic heating. Additionally, the radiator chip is supported by glass rods, thereby reducing conduction between the radiator chip and the positioners. These measures were necessary to maintain the temperature of the positioners below the threshold value.

Unfortunately, as further discussed in Chapter 5, the geometry of our radiator significantly limited the capabilities of Platform 3, preventing NFTPV measurements from being conducted with this platform. In fact, the large thermal mass of the radiator at higher temperatures (i.e., 700 K) caused significant damage to the PV cell upon contact, precluding further high-temperature scans. Moreover, non-localized heating made it difficult to distinguish between contact with the radiator tip and the radiator substrate, further complicating the alignment process. Additionally, contact detection through deflection monitoring is not feasible with this radiator. Finally, the PV cell must be cooled to mitigate the effect of parasitic subgap radiation.

3.4 Platform 4: Future Near-Field Thermophotovoltaic Measurement

Platform 4, shown in Fig. 3.4, is a proposed design for the fourth iteration of our experimental platform, which will be employed to achieve Objective 3, as discussed in

Chapter 5. This proposed platform is a revised version of Platform 3, featuring an improved radiator design. Platform 4 will hopefully allow to overcome the shortcomings encountered with Platform 3 and enable NFTPV measurements.

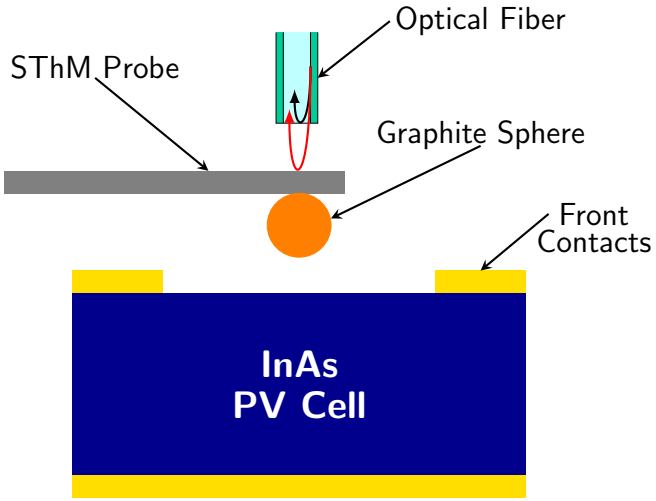

Figure 3.4: Illustration of Platform 4. This figure is a reproduction of Fig. 5.9.

In Platform 4, we propose a major redesign of our experimental platform to facilitate the alignment of the radiator with the PV cell. We suggest addressing the limitations encountered with Platform 3 by replacing our radiator chip with a graphite sphere glued onto a scanning thermal microscope (SThM) probe (BRUKER® VITA-HE-NANOTA-200) using a ceramic adhesive (RESBOND™ 989F) that can withstand temperatures up to 1920 K, as illustrated in Fig. 3.4. The micrometer-sized heating element will enable higher temperature measurements and significantly simplify the alignment process. Similar to Platforms 1 and 2, contact detection is enabled by a fiber interferometer measuring the vibrational response of the mechanically excited probe. We also plan on integrating a thermoelectric cooler to maintain the PV cell at a constant temperature, thereby minimizing the effect of parasitic subgap radiation. Finally, the graphite spherical surface will eliminate the need for angular alignment.

Despite the complex design of the radiator and the restrictions imposed on its material, Platform 4 can still be regarded as a flexible platform, as it enables the testing of

many new interesting PV materials. In fact, the geometry of the heating element will facilitate the integration of PV cells of various geometries. Additionally, although we will be limited to materials that can be shaped into microspheres, using a spherical radiator will simplify the alignment procedure, enabling the rapid testing of various PV samples.

4. Near-Field Radiative Heat Transfer with Nanomechanical Resonators

This chapter discusses the development of a flexible experimental NFRHT platform (i.e., Objective 1) and the use of nanomechanical resonators for NFRHT measurements (i.e., Objective 2). In Section 4.1, we present our first NFRHT article [136], which focuses on achieving Objective 1 while using nanomechanical resonators as radiation sensors in an attempt to address Objective 2. Unfortunately, the limited alignment capabilities and unoptimized geometries of the experimental platform, referred to as Platform 1 in Chapter 3, significantly constrained the minimal achievable separation and prevented us from fully realizing Objective 2. In Section 4.2, we present our second NFRHT article [150], in which we attempt to perform deep sub-wavelength NFRHT measurements and fully explore the potential of nanomechanical resonators, relying on a new experimental platform, referred to as Platform 2 in Chapter 3, featuring improved alignment capabilities and refined geometries. The numerical model developed to analyze the NFRHT measurements obtained from Platforms 1 and 2 is presented in Section 2.2.2 and is further discussed in the main text and supplementary information of each manuscript.

4.1 High Resolution Measurement of Near-Field Radiative Heat Transfer Enabled by Nanomechanical Resonators

This section is a reproduction of our first NFRHT article [136], published in *Applied Physics Letters* in 2021, which focuses on the development of a flexible platform for experimentally testing new materials for NFRHT. The platform developed in this work, referred to as Platform 1 in Chapter 3, represents the first iteration of our experimental NFRHT platform.

4.1.1 Impact

This manuscript presents the following novelties:

1. Performed NFRHT measurements using SiN membranes as radiation sensors.
2. Developed a NFRHT platform relying entirely on commercially available components.
3. Reported NFRHT measurements with an unprecedented resolution (i.e., 1.2×10^{-6} K).

4.1.2 Author Contribution

Mathieu Giroux: As the lead graduate student associated with this project, I designed the platform, performed the measurements, and developed the numerical model. Additionally, I was the lead author of this article.

Chang Zhang: As a graduate student at the University of Ottawa, Chang helped with the development of the numerical model.

Nikaya Snell: As a graduate student at the University of Ottawa, Nikaya provided me with training on the lock-in amplifier interface.

Gengyang Mu: As a graduate student at the University of Ottawa, Gengyang led the fabrication of the SiN membranes used in this work.

Michel Stephan: As an undergraduate student at the University of Ottawa, Michel helped with the design of the platform.

Raphael St-Gelais: As the principal investigator of the project and a professor at the University of Ottawa, Dr. St-Gelais led the conceptualization of the project, guided my research, provided detailed feedback throughout this project, and assisted in editing the manuscript.

4.1.3 Article Content

High Resolution Measurement of Near-Field Radiative Heat Transfer enabled by Nanomechanical Resonators

Mathieu Giroux[a], Chang Zhang[a], Nikaya Snell[a], Gengyang Mu[a], Michel Stephan[a], and Raphael St-Gelais[a,b]

[a]Department of Mechanical Engineering, University of Ottawa, Ottawa K1N 6N5, Ontario, Canada
[b]Department of Physics, University of Ottawa, Ottawa K1N 6N5, Ontario, Canada

Abstract

Near-field radiative heat transfer (NFRHT) research currently suffers from an imbalance between numerous theoretical studies, as opposed to experimental reports that remain, in proportion, relatively scarce. Existing experimental platforms all rely on unique custom-built devices on which it is difficult to integrate new materials and structures for studying the breadth of theoretically proposed phenomena. Here we show high-resolution NFRHT measurements using, as our sensing element, silicon nitride freestanding nanomembranes—a widely available platform routinely used in materials and cavity optomechanics research. We measure NFRHT by tracking the high mechanical quality (Q) factor ($> 2 \times 10^6$) resonance of a membrane placed in the near-field of a hemispherical hot object. We find that a high Q-factor enables a temperature resolution (1.2×10^{-6} K) that is unparalleled in previous NFRHT experiments. Results are in good agreement with a custom-built model combining heat transport in nanomembranes and the effect of non-uniform stress/temperature on the resonator eigenmodes.

Near-field radiative heat transfer (NFRHT) has attracted a lot of attention over the past years for potential applications such as energy conversion [1, 6, 8, 117, 151], active thermal control [9–12], or for more fundamental studies on the effect of various material platforms [13–17], material geometries [18], or external fields [19]. Near-field thermal radiation consists of evanescent electromagnetic coupling that occurs between two bodies at subwavelength distances, greatly increasing the radiative exchange beyond the blackbody limit [21, 22, 152]. As demonstrated theoretically [3, 4], this enhancement could allow conversion of heat to electricity with a higher efficiency than any existing portable solid-state solution. In addition, by concentrating heat into a narrow spectral bandwidth [23–26], near-field thermal radiation could be used to better control the heat flux [18], thus potentially enabling active thermal control devices such as thermal transistors [11, 27].

While many theoretical works have been reported on near-field thermal radiation, experimental progress is relatively scarce due to important technical challenges, i.e., maintaining objects at small distances while avoiding contact, under important temperature gradients. Different approaches have been reported over the years. Some rely on nanotips [12, 16, 26, 32, 33, 60] or microspheres [34–37, 53, 61, 62, 153] to avoid alignment issues [154], others rely on more complex systems using active parallelism control [38–46, 155], and others use static systems with spacers [7, 47–52]. Current experimental platforms all rely on unique, custom-built systems, on which it is difficult to integrate new materials to experimentally study and confirm existing theoretical work on NFRHT. There is consequently a substantial imbalance between a large body of theoretically investigated phenomena [1–4, 9–11, 13–15, 17, 18, 21–26, 117], and of relatively modest experimental capabilities. Due to their highly custom nature, experimental platforms are typically reported only once in the scientific literature and are rarely used again as a systematic tool for studying other NFRHT effects. Moreover, a large proportion of these platforms used SiO_2 only [65]. Although, SiO_2 is efficient for NFRHT experiments, many materials

with attractive properties such as graphene [63], thin-film metals [13], multilayers [64], lossy materials [18], hyperbolic materials [14, 19], and metamaterials [15] remain largely untested.

Here, we show high-resolution NFRHT measurements using, as our sensing element, silicon nitride (SiN) membranes (Fig. 4.1)—a widely available platform routinely used in nanomaterials [130] and optomechanics research [131–133]. Such membranes are commercially available from multiple suppliers, therefore, resulting in a reproducible and flexible experimental platform. Moreover, emerging materials are routinely deposited on SiN membranes for transmission electron microscopy (TEM) analysis. Protocols for depositing materials on SiN are, therefore, well developed, making SiN an ideal substrate for testing new materials for NFRHT research.

Our experimental approach, illustrated in Fig. 4.1a, uses a glass half sphere as a hot surface (Thorlabs BK7 lens, 12.7 mm radius) onto which a metal-ceramic heater is attached. The half sphere is used to simplify alignment, allowing the use of a single-axis positioner. Additionally, the glass half sphere could potentially be coated to test different materials. The half sphere is brought closer to the SiN membrane using a vacuum positioner actuated with an inertia drive (New Focus Picomotor$^{\text{TM}}$). The temperature of the membrane is measured in real-time with an optical fiber interferometer [134], by measuring the shift of its mechanical resonance frequency due to thermal expansion [139, 149]. To suppress fluidic damping and convective heat transfer, the resonator and the glass half sphere are positioned in a custom-designed high vacuum chamber operating at a typical pressure of 2×10^{-6} Torr. The membrane used for the current experiment is made of low stress SiN (built-in stress $\sim$100 MPa) with nominal dimensions of 3 mm in side length and $t_{\text{SiN}} = 100$ nm thickness. The membrane was fabricated in-house, but comparable devices can be purchased commercially from various suppliers. The silicon (Si) frame of the membrane is mounted on an aluminum support [see Fig. 4.1b] using nickel paste (Pelco®), enabling a good thermal conduction for maintaining the frame at

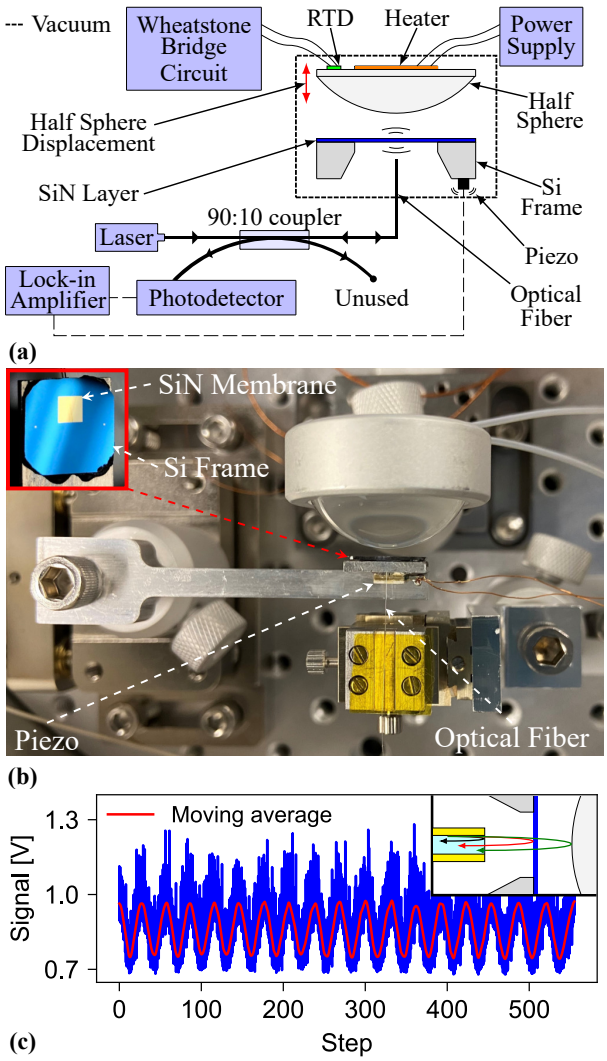

Figure 4.1: (a) Schematic of the experimental NFRHT measurement platform. (b) Photograph of the NFRHT measurement platform inside the vacuum chamber. (c) Interferometric measurement of the half sphere displacement, yielding 25.3 nm per actuator step in this particular instance. Inset: schematic of the reflected optical signals at the tip of the optical fiber (black), the resonator surface (red), and the surface of the half sphere (green).

room temperature. A piece of piezoelectric ceramic (Thorlabs shear piezoelectric chip), mounted on the back of the aluminum support, is used to drive the membrane at its resonance frequency.

The glass half sphere is heated by a metal-ceramic heater connected to a power supply, which is actively controlled from a computer. We rely on the linear variation of the resistance to track the temperature of the metal-ceramic heater and actively control

its temperature with a closed-loop custom proportional integral differential (PID) control algorithm. The temperature of the glass half sphere is also measured with a resistance temperature detector (RTD), which is connected to a modified Wheatstone bridge circuit, relying on the Wien-bridge oscillator principle [156] to reduce noise. At the beginning of the heating process, the PID adjusts the heater to a stable temperature, which takes approximately 200 s (i.e., Fig. 4.6, blue curve, in supplementary material Section 4.1.4.1). After about 1000 s, the temperature of the whole system is stable (see supplementary material Section 4.1.4.1), and the near-field heat transfer measurement can begin.

The optical fiber interferometer plays the double role of measuring the membrane resonance frequency [134] (and, thus, its temperature) and of calibrating the open-loop positioner stage displacement. In a typical implementation of such an optical fiber interferometer [134], reflection of the laser signal occurs at two interfaces: the tip of the optical fiber [Fig. 4.1c, black arrow] and the surface of the resonator (red arrow). However, in our case, reflection also occurs at the surface of the half sphere (green arrow). This creates two interference signals (i.e., fiber-sphere and fiber-resonator) that can easily be demultiplexed, given that the resonator signal is centered at a much higher frequency—typically 83 kHz for eigenmode order (m, n) = (2, 2) with the current resonator dimensions. As the sphere is displaced, the slower fiber-sphere interference signal shows a periodic pattern [Fig. 4.1c] that allows calibration of the stage displacement, considering our laser (RIO ORION$^{\text{TM}}$) wavelength of 1563.52 nm. The actuator displacement is measured for every scan, yielding typical values in the $24-25.5$ nm/step range. The membrane resonance frequency is tracked by phase locking (PLL) of the lock-in amplifier (Zurich Instrument Ltd. model MFLI) oscillator to the membrane resonance mode order (m, n) = (2, 2) [157]. The heating effect of the laser is shown to be negligible (see supplementary material Section 4.1.4.3).

Raw data scans are presented in Fig. 4.2a for a half sphere displacement velocity of one step per second toward the membrane. As expected, scans without heating of the half

sphere (i.e., $\Delta T = 0$ K) produce no noticeable frequency shift, while scans at $\Delta T = 10$ K show clear frequency shifts, until contact occurs and resonance mode tracking is lost. In the case of this data set, a frequency shift of $\sim$19 Hz was measured before contact.

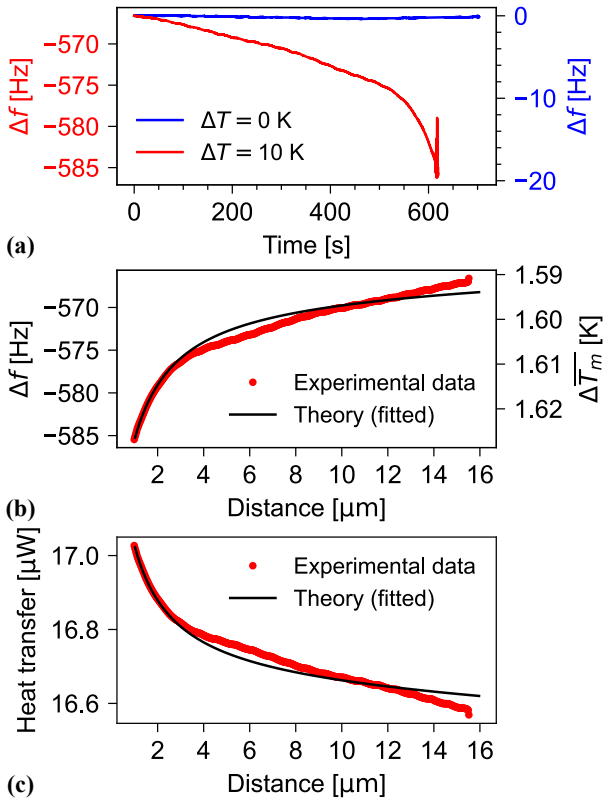

Figure 4.2: (a) Raw data scans at room temperature (blue) and under a temperature gradient of 10 K (red) for a half sphere displacement velocity of 1 step per second towards the membrane. The 10 K gradient scan shows a frequency shift of $\sim$19 Hz confirming near-field thermal coupling, in contrast with the $\Delta T = 0$ K control scan (b) Experimental (red) and theoretical (black) (fitted horizontally and vertically) resonance frequency shift as a function of separation for a 10 K thermal gradient. The fit suggests a minimal separation of $\sim$980 nm before sphere-membrane contact. The -570 Hz initial shift at large distances results from far-field radiative coupling. (c) Experimental (red) and theoretical (black) (fitted horizontally and vertically) heat transfer as a function of separation for a 10 K thermal gradient.

We compare the experimental frequency shift from Fig. 4.2a with a theoretical model that combines heat diffusion inside the membrane, multilayer NFRHT calculations [5, 93], as well as the effect of non-uniform stress obtained by solving the motion equation [137] in the membrane. As shown in Ref. 66, the radiative thermal coupling properties of

square membranes of side length L are well approximated by that of circular membranes of effective radius $r_{\text{eff}} = 1.252\frac{L}{2}$. We, therefore, approximate our square membrane to a circular membrane of radius $r_{\text{eff}} = 1.878$ mm. The membrane temperature profile $T_{\text{m}}(r)$ is obtained by numerically solving the heat diffusion equation

$$k_{\text{SiN}}\nabla^2 T_{\text{m}}(r) + \dot{q}_{\text{gen}}(r, T_{\text{m}}) = 0, \tag{4.1}$$

where k_{SiN} is the thermal conductivity of SiN. The internal generation term $\dot{q}_{\text{gen}}$ is given as a function of the radius r by NFRHT calculations

$$\dot{q}_{\text{gen}}(r, T_{\text{m}}) = G_{\text{NF}}(r) \cdot \left(T_{\text{sphere}} - T_{\text{m}}(r)\right)/t_{\text{SiN}} + \dot{q}_{\text{FF}_{\text{front}}}(T_{\text{m}}(r)) + \dot{q}_{\text{FF}_{\text{back}}}(T_{\text{m}}(r)), \tag{4.2}$$

where T_{sphere} is the glass half sphere temperature. In Eq. 4.2, G_{NF}, in $\text{W/m}^2 \cdot \text{K}$, accounts for NFRHT coupling of evanescent waves and is calculated using the NFRHT algorithm given in Ref. 5 with the permittivity of the glass half sphere taken from Ref. 129 and that of SiN taken from Ref. 127. Far-field radiative heat transferred to the back side of the membrane is computed using the emissive power law [82]; $\dot{q}_{\text{FF}_{\text{back}}}(r) = \epsilon_{\text{SiN}}\sigma(T_\infty^4 - T_{\text{m}}^4(r))/t_{\text{SiN}}$, where the emissivity ϵ_{SiN} is taken from Ref. 66, σ is the Stefan-Boltzmann constant, and $T_\infty = 293$ K is the environment temperature. The far-field radiative heat transferred to the front side of the membrane $\dot{q}_{\text{FF}_{\text{front}}}$ is calculated using the conventional far-field thermal radiation formalism [82] detailed in supplementary material Section 4.1.4.2. To account for the sphere curvature, we use the proximity approximation (also known as the Derjaguin approximation [97]). Each point on the sphere is approximated to a flat surface with a distance $d(r) = d_0 + R - \sqrt{R^2 - r^2}$, where d_0 is the distance at the sphere apex and R is the radius of the sphere. The approximation is proven to be valid for NFRHT [35], especially for large radius objects like ours. Solving Eqs. 4.1 and 4.2 numerically gives the temperature profile, from which we extract the resonance

frequency shift by numerically solving the motion equation in spherical coordinates for a thin membrane under tensile stress [137]

$$\frac{1}{r}\frac{\partial}{\partial r}\left(\left(\sigma_0+\sigma_r(r,T_{\mathrm{m}})\right)r\frac{\partial u(r,t)}{\partial r}\right)-\rho\frac{\partial^2 u(r,t)}{\partial t^2}=0, \tag{4.3}$$

where σ_0 and $\sigma_r(r,T_{\mathrm{m}})$ are, respectively, the temperature-independent ($\sigma_0 \approx 100$ MPa) and the position-dependent components of the in-plane stress, ρ is the density of SiN, and $u(r,t)$ represents the out-of-plane displacement of the membrane. The position-dependent component of the in-plane stress (σ_r) is given as a function of the temperature profile [138]

$$\sigma_r(r,T_{\mathrm{m}})=-\alpha E\left[\frac{1}{r^2}\int_0^r r\Delta T_{\mathrm{m}}(r)\mathrm{d}r+\frac{1+\nu}{1-\nu}\frac{\Delta\overline{T_{\mathrm{m}}}}{2}\right], \tag{4.4}$$

where α is the thermal expansion coefficient of SiN, E is the Young modulus, ν is the Poisson ratio, and $\Delta T_{\mathrm{m}} = T_{\mathrm{m}} - T_\infty$. $\overline{T_{\mathrm{m}}}$ denotes the temperature average over the membrane area, such that $\Delta\overline{T_{\mathrm{m}}} = \overline{T_{\mathrm{m}}} - T_\infty$.

In Fig. 4.2b, the data is in good agreement with the theoretical model [Eqs. 4.1-4.4]. The experimental and theoretical data were fitted together by proceeding to horizontal translation of the experimental data and vertical translation of the theoretical model. The horizontal translation accounts for uncertainty on the initial sphere-membrane distance, while the vertical translation accounts for uncertainty of the glass half sphere surface temperature and for drift in ambient temperature in the vacuum chamber. The fit suggests that we have reached a minimal distance of $\sim$980 nm, which is larger than the state of the art experiments [16, 40, 41]. Attraction forces, surface contamination, and sphere-membrane misalignment could be responsible for the imposed gap limit. It is also possible that shocks originating from the inertia drive actuator cause collapsing of the membrane with the half sphere at small separations. Upgrading of our positioners from inertia drive to flexure stages in the near future will eliminate this possibility. From

a fundamental standpoint, we would ultimately be limited by the positioner step size (24−25.5 nm) which is greater than thermomechanical fluctuations in the membrane (< 1 nm). The latter is most likely the ultimate fundamental resolution of our platform, but we are still far from approaching it. At distances larger than $\sim 3\,\mu$m, the frequency shift from the experimental data is slightly larger than the one computed by the theoretical model. A larger infrared material absorption coefficient than considered in the simulation, increasing the contribution of the propagating wave, could explain this discrepancy [40]. Figure 4.2c presents the data in a more conventional manner for NFRHT, i.e., in terms of heat transfer power vs distance. The heat transfer power is obtained using Eqs. 4.1-4.4 to infer $G_{\mathrm{NF}}(r)$ from the measured frequency shift, and then by integrating over the membrane area.

We find that one of the main advantages of our approach is the very high temperature resolution enabled by the use of a high mechanical quality factor (Q-factor) sensor. By measuring the Allan deviation of the frequency signal and converting it to temperature resolution, we obtain [Fig. 4.3a] what we believe is an unprecedented resolution in the context of experimental NFRHT. We measure a resolution of 1.2×10^{-6} K at low averaging time, while the highest experimentally reported resolution in NFRHT measurements is 2×10^{-5} K using thermocouples [16]. Theoretical analyses claim that bi-material deflection could also achieve similar performances [65], but this was not confirmed experimentally. High resolution in a frequency-shift mechanical sensor directly results from the narrow linewidth of the resonance peaks (i.e., low dissipation, high mechanical Q-factor) [158]. Our Q-factor was measured at room temperature and under a temperature gradient of 10 K and, in both cases, $\mathrm{Q} > 2 \times 10^6$ was obtained [see Fig. 4.3b]. In contrast with this very high resolution at low averaging time, performances are limited by drift at larger averaging time [see Fig. 4.3a]. We find that the drift contribution is worse when the half sphere is heated. For this reason, drift currently prevents us from performing conclusive distance scans [i.e., as in Fig. 4.2b] for $\Delta T > 10$ K.

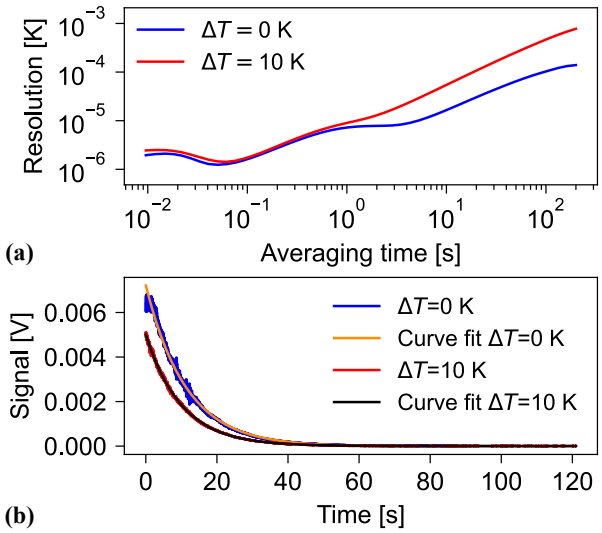

Figure 4.3: (a) Resolution of the resonator as a function of averaging time computed from the measured Allan deviation of the PLL frequency signal at both room temperature (blue) and under a temperature gradient of 10 K (red). The lowest obtained resolution is 1.2×10^{-6} K, which is unprecedented in NFRHT measurements. The resolution is limited by drift at higher averaging time, and we note that drift is worse in the presence of a 10 K thermal gradient. (b) Measured mechanical ringdown for mode (2, 2) at room temperature (blue) and under a temperature gradient of 10 K (red). The Q-factor extracted from the exponential fit is comparable at $\Delta T = 0$ K (2.9×10^6) and for $\Delta T = 10$ K (2.6×10^6).

The most important source of uncertainty in our experiment results from the single-axis positioner, which does not allow for active alignment, under vacuum, of the sphere apex with the center of the membrane. In Fig. 4.4a, we quantify the effect of possible sphere-membrane misalignment by computing the membrane average temperature variation ($\Delta\overline{T_{\mathrm{m}}}$) by solving Eqs. 4.1 and 4.2 with an offset of 1 mm. We find that this offset decreases the predicted frequency shift, thus, potentially explaining the relatively large minimum gap achieved in Fig. 4.2b. Planned implementation of a five-axis positioner should alleviate this uncertainty in the near future.

Rather than solving Eqs. 4.3 and 4.4 numerically, it would be convenient to express a simple linear relation that converts the frequency shift (Δf) to the average change in the membrane temperature ($\Delta\overline{T_{\mathrm{m}}}$). This is done by assuming that T_{m} is position independent in Eq. 4.4, from which we obtain the following relation [73]:

$$\Delta\overline{T_{\mathrm{m}}} = -\frac{2\sigma_0(1-\nu)}{\alpha E f_0}\Delta f, \tag{4.5}$$

where f_0 is the resonance frequency of the membrane at room temperature. In Fig. 4.4b, we compare the frequency obtained by solving Eq. 4.3 to the one obtained from Eq. 4.5. By not considering the effect of non-uniform temperature and stress, Eq. 4.5 yields a systematic underestimation of the frequency shift, reaching 40% at the smallest separation considered here (10 nm).

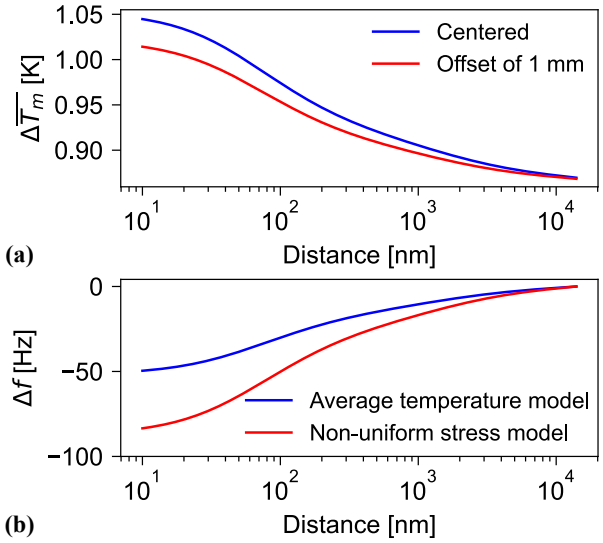

Figure 4.4: Error analysis. (a) Computed near-field coupling of the SiN membrane for a perfectly aligned case (blue), and for a 1 mm misalignment between the sphere apex and the membrane center (red). The offset decreases the expected frequency shift, which may affect the minimal distance inferred from Fig. 4.2b. (b) Predicted frequency shift from Eqs. 4.1-4.4 (red) compared with the approximation of a uniform membrane temperature [Eq. 4.5] (blue). The comparison shows a growing discrepancy as we move deeper in the near-field regime, yielding up to a 40% error at the smallest gap (10 nm).

Significant optimization of our sphere-membrane approach will be possible in future work. As shown in Fig. 4.5a, our $L = 3$ mm membrane results in a very small relative increase in temperature compared to a $L = 0.5$ mm membrane. A first reason for this effect is weak thermal conduction in large-area SiN membranes. Large-area membranes consequently reach a large temperature in the far-field (i.e., a weaker thermal gradient), while small-area membranes remain closer to room temperature by offering a shorter

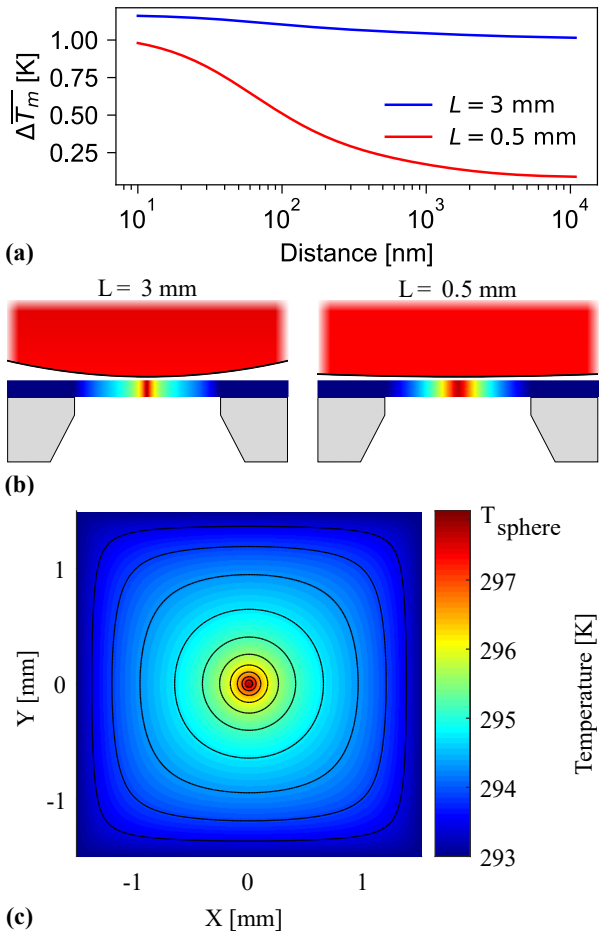

Figure 4.5: (a) Calculated temperature variation of the SiN membrane for the case of a $L = 3$ mm (blue) and $L = 0.5$ mm (red) membrane. Larger membranes result in a much smaller temperature increase due to saturation and dilution effects (see the main text). (b) Schematic of the half sphere and membrane showing the computed temperature profile of the SiN resonator at a separation of 10 nm in the case of a $L = 3$ mm (left) and $L = 0.5$ mm (right) membranes. The curvature of the half sphere is scaled proportionally to the size of the membrane. (c) Two-dimensional view of the simulated SiN membrane temperature profile for a $L = 3$ mm membrane at a separation of 10 nm. The temperature at the center of the membrane is close to the sphere temperature, illustrating the saturation effect for large membrane sizes.

path to the Si frame. Furthermore, at very small distances, near-field thermal radiation is predicted to saturate the membrane temperature at the sphere apex, thus resulting in an even weaker thermal gradient. This effect is worse in large membranes compared to smaller membranes that have higher thermal conduction [see simulated profiles in Figs 4.5b and 4.5c]. Finally, the ratio of area exposed to near-field vs far-field radiation is

lower in large membranes, thus greatly diluting the near-field signal. The sole advantage of a large membrane, therefore, appears to be simplification of the alignment procedure, enabling the use of a single-axis positioner in the present case.

We have demonstrated NFRHT measurements using nanomechanical resonators, as well as a clear path for substantial improvements by optimizing the resonator dimension. Our approach notably enables the highest reported temperature resolution (1.2×10^{-6} K) in the context of NFRHT measurements. We expect that the wide availability of free-standing SiN substrates will make our platform a go-to approach for studying new materials for NFRHT. Coupling mechanical oscillators with near-field thermal radiation could also open new interesting research avenues. For example, mechanical oscillations coupled with near-field thermal radiation could be used for implementing systems that rely on temperature oscillations for converting heat to electricity, exploiting for example pyroelectric materials [159, 160]. Ultra-low dissipation of SiN mechanical oscillators could also allow simultaneous characterization of Casimir forces [148] and NFRHT.

See the supplementary material for the analysis of the temperature stabilization of the platform, details on the far-field radiation model and details on the laser heating effect.

This work was funded by the Natural Sciences and Engineering Research Council of Canada (NSERC), the Ontario Graduate Scholarship (OGS), the New Frontiers in Research Fund (NFRF), and by start-up funds from the Faculty of Engineering at the University of Ottawa.

4.1.4 Supplementary Information

4.1.4.1 Temperature Stabilization

Fig. 4.6 shows the temperature stabilization of different components in the platform. The temperature of the heater (blue curve) is controlled by a PID controller and, there-

fore, reaches a stable temperature very quickly ($t \approx 200$ sec). On the other hand, the RTD (black curve), measuring the temperature of the half sphere, and the membrane (red curve), measuring the temperature in the far-field, take longer to stabilize ($t \approx 1000$ sec) due to the large thermal capacitance of the half sphere. After the system reaches steady state, the heater and RTD temperature are superimposed, thus confirming good thermal contact between the heater, the glass sphere, and the RTD.

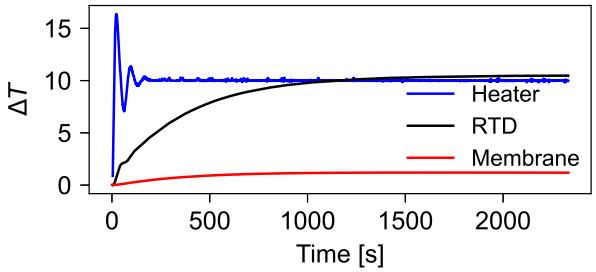

Figure 4.6: Initial temperature calibration and stabilization before NFRHT measurements. The heater temperature (blue) is actively stabilized to $\Delta T = 10$ K. The membrane (in the far-field) and a RTD placed on the half sphere are stable after $t \approx 1000$ sec.

4.1.4.2 Far-Field Radiation Model

The far-field radiative heat transferred to the front side of the membrane $\dot{q}_{\mathrm{FF}_{\mathrm{front}}}$ can be computed from the equivalent thermal circuit, represented in Fig. 4.7, for the three surrounding surfaces: the environment (point 3), the half sphere (point A) and the SiN membrane (point B). This model approximates the environment to a blackbody, consequently, neglecting the photons reflected on the environment surface travelling back to the half sphere or membrane surface.

R_1 and R_2 are, respectively, the surface resistances of the half sphere and of the SiN membrane, calculated as [82]:

$$R_1 = \frac{1 - \epsilon_{\mathrm{Glass}}}{A_1 \epsilon_{\mathrm{Glass}}}, \tag{4.6}$$

$$R_2 = \frac{1 - \epsilon_{\mathrm{SiN}}}{A_2 \epsilon_{\mathrm{SiN}}}, \tag{4.7}$$

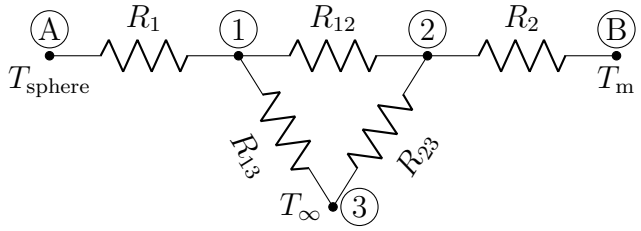

Figure 4.7: Equivalent thermal circuit of the far-field radiation between the half sphere (point A), the membrane (point B), and the environment (point 3). In this case, the environment is considered a blackbody. R_1 and R_2 are the surface resistances and R_{12}, R_{13}, and R_{23} are the space resistances accounting for the view factors.

where ϵ_{Glass} is the emissivity of the glass half sphere, A_1 is the surface area of the sphere (the area of a full sphere is used to agree with the view factor model, see supplementary material Section 4.1.4.2.1), and A_2 is the surface area of the SiN membrane. R_{12}, R_{13}, and R_{23} are the space resistances between the half sphere, the SiN membrane, and the environment accounting for the view factors (supplementary material Section 4.1.4.2.1). The space resistances are given as:

$$R_{12} = \frac{1}{A_1 F_{12}}, \tag{4.8}$$

$$R_{13} = \frac{1}{A_1 F_{13}}, \tag{4.9}$$

$$R_{23} = \frac{1}{A_2 F_{23}}, \tag{4.10}$$

where F_{12} is the view factor from the half sphere to the SiN membrane, F_{13} is the view factor from the half sphere to the environment, and F_{23} is the view factor from the SiN membrane to the environment. At nodes A, B, and 3 the equivalent potential applied to the circuit is equal to the blackbody emissive powers (E_{b}):

$$E_{\text{bA}} = \sigma T_{\text{sphere}}^4, \tag{4.11}$$

$$E_{\mathrm{bB}} = \sigma T_{\mathrm{m}}^4, \tag{4.12}$$

$$E_{\mathrm{b3}} = \sigma T_{\infty}^4. \tag{4.13}$$

A relation for the potential at node 2 (P_2) can be derived from the application of the Kirchhoff current law at node 1 and 2, yielding the following equations:

$$\frac{E_{\mathrm{bA}} - P_1}{R_1} + \frac{P_2 - P_1}{R_{12}} + \frac{E_{\mathrm{b3}} - P_1}{R_{13}} = 0, \tag{4.14}$$

$$\frac{E_{\mathrm{bB}} - P_2}{R_2} + \frac{P_1 - P_2}{R_{12}} + \frac{E_{\mathrm{b3}} - P_2}{R_{23}} = 0, \tag{4.15}$$

where P_1 is the potential at node 1. Solving this analytically gives us the following relation for the potential at node 2:

$$P_2 = \frac{\begin{array}{r} E_{\mathrm{bA}}R_{13}R_2R_{23} + E_{\mathrm{bB}}R_1R_{12}R_{23} + E_{\mathrm{bB}}R_1R_{13}R_{23} + E_{\mathrm{bB}}R_{12}R_{13}R_{23} + \\ E_{\mathrm{b3}}R_1R_{12}R_2 + E_{\mathrm{b3}}R_1R_{13}R_2 + E_{\mathrm{b3}}R_1R_2R_{23} + E_{\mathrm{b3}}R_{12}R_{13}R_2 \end{array}}{\begin{array}{r} R_1R_{12}R_2 + R_1R_{12}R_{23} + R_1R_{13}R_2 + R_1R_{13}R_{23} + R_1R_2R_{23} \\ + R_2R_{12}R_{13} + R_{12}R_{13}R_{23} + R_{13}R_2R_{23} \end{array}}. \tag{4.16}$$

Using Ohm's law at the resistance R_2 and Eq. 4.16, one can compute the heat absorbed by unit volume due to radiation at the front side of the SiN membrane $\dot{q}_{\mathrm{FF}_{\mathrm{front}}}$:

$$\dot{q}_{\mathrm{FF}_{\mathrm{front}}} = \frac{P_2 - E_{\mathrm{bB}}}{R_2 t_{\mathrm{SiN}}}. \tag{4.17}$$

4.1.4.2.1 View Factor Model

The view factor from the half sphere to the SiN membrane is computed using the tabulated relation from Ref. 161 for a sphere of radius R and a disk of radius r_{eff} separated by a distance d_0, yielding the following equation:

$$F_{12} = \frac{1}{2}\left(1 - \frac{1}{\sqrt{1+\frac{1}{h^2}}}\right), \tag{4.18}$$

where $h = \frac{d_0+R}{r_{\text{eff}}}$. Using the principle of reciprocity,

$$A_1 F_{12} = A_2 F_{21}, \tag{4.19}$$

allows us to find the view factor for the radiation from the membrane to the half sphere F_{21}. Finally, the view factors for the radiation going from the sphere to the environment (F_{13}) and from the membrane to the environment (F_{23}) are computed using the enclosure summation:

$$F_{13} = 1 - F_{12}, \tag{4.20}$$

$$F_{23} = 1 - F_{21}. \tag{4.21}$$

4.1.4.3 Laser Heating Effect

We performed additional measurements to confirm that temperature variation due to the laser heating is negligible. SiN is expected to have low absorption as it is often used as a waveguide material in this wavelength range [162]. The wavelength of our laser (RIO ORION$^{\text{TM}}$) is 1563.52 nm. As shown in Fig. 4.8, the normal spectral emissivity (i.e., the absorption) of SiN at such wavelength is close to zero.

Our laser output power is $P = 10.7$ mW, with a factory-calibrated stability of $\pm 0.3\%$ for an ambient temperature variation of ± 1 °C, which is within the specs of our lab environment. Therefore, the maximal power variation is expected to be 0.064 mW. To measure the effect of such power variation, we measure, in Fig. 4.9, the effect of varying the laser power by 0.06 mW. To do so, we used a tunable laser (JDS Uniphase SWS15101) with which we can fine tune the output power, and we set the wavelength to

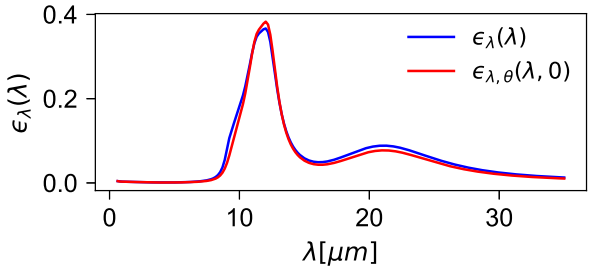

Figure 4.8: Normal (red) and hemispherical (blue) spectral emissivity for freestanding SiN membranes at room temperature computed from Ref. 127.

1563.52 nm. We use a 1.5 mm membrane for this particular measurement due to sample availability, but we expect the measured temperature shifts to be even smaller for larger, less responsive membranes.

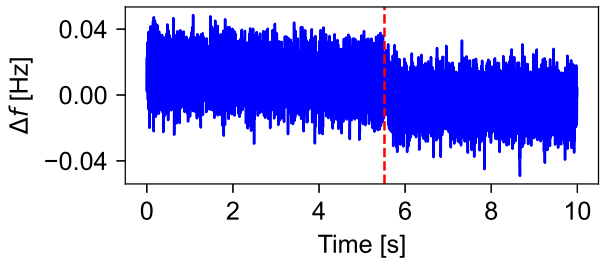

Figure 4.9: Frequency variation due to a 0.06 mW increase of the laser power. The power was changed at a time corresponding to the dotted red line. The resonance frequency drops by approximately 0.01 Hz.

According to the data in Fig. 4.9, the frequency variation due to a ±0.3% laser power variation would be approximately ±0.005 Hz. This corresponds to a temperature stability of ±18 µK, if we assume in first approximation that the temperature of the membrane is position independent (i.e., using Eq. 4.5 of the manuscript). This is negligible compared to our temperature resolution (see Fig. 4.3a), as long as the ±0.3% power fluctuations occur on a timescale larger than 1 second.

4.2 Measurement of Near-Field Radiative Heat Transfer at Deep Sub-Wavelength Distances using Nanomechanical Resonators

This section is a reproduction of our second NFRHT article [150], published in *Nano Letters* in 2023, which investigates the potential of nanomechanical resonators for NFRHT measurements. Relying on the second iteration of our experimental NFRHT platform, referred to as Platform 2 in Chapter 3, this study focuses on the performance of NFRHT measurements in the deep sub-wavelength regime using nanomechanical resonators.

4.2.1 Impact

This manuscript presents the following novelties:

1. Performed NFRHT measurement in the deep sub-wavelength regime using nanomechanical resonators.

2. Demonstrated that nanomechanical resonators create opportunities for simultaneously measuring both NFRHT and the Casimir effect.

4.2.2 Author Contribution

Mathieu Giroux: As the lead graduate student associated with this project, I designed the platform, performed the measurements, and developed the numerical model. Additionally, I was the lead author of this article.

Michel Stephan: As a graduate student at the University of Ottawa, Michel helped with the design of the platform.

Maxime Brazeau: As a graduate student at the University of Ottawa, Maxime assisted with the atomic force microscopy (AFM) measurements.

Sean Molesky: As a professor at Polytechnique Montréal, Dr. Molesky provided detailed feedback and helped with the conceptualization of the project.

Alejandro W. Rodriguez: As a professor at Princeton, Dr. Rodriguez helped with the conceptualization of the project.

Jacob J. Krich: As a professor at the University of Ottawa, Dr. Krich provided detailed feedback and helped with the conceptualization of the project.

Karin Hinzer: As a professor at the University of Ottawa, Dr. Hinzer provided detailed feedback and helped with the conceptualization of the project.

Raphael St-Gelais: As the principal investigator of the project and a professor at the University of Ottawa, Dr. St-Gelais led the conceptualization of the project, guided my research, provided detailed feedback throughout this project, and assisted in editing the manuscript.

4.2.3 Article Content

Measurement of Near-Field Radiative Heat Transfer at Deep Sub-Wavelength Distances using Nanomechanical Resonators

Mathieu Giroux[a], Michel Stephan[a], Maxime Brazeau[a], Sean Molesky[b,c], Alejandro W. Rodriguez[c], Jacob J. Krich[d], Karin Hinzer[e], and Raphael St-Gelais[a,d]

[a]Department of Mechanical Engineering, University of Ottawa, Ottawa K1N 6N5, Ontario, Canada
[b]Department of Engineering Physics, Polytechnique Montreal, Montreal, Quebec H3T 1J4, Canada
[c]Department of Electrical and Computer Engineering, Princeton University, Princeton, New Jersey 08544, United States
[d]Department of Physics, University of Ottawa, Ottawa, Ontario K1N 6N5, Canada
[e]SUNLAB, School of Electrical Engineering and Computer Science, University of Ottawa, Ottawa, Ontario K1N 6N5, Canada

Abstract

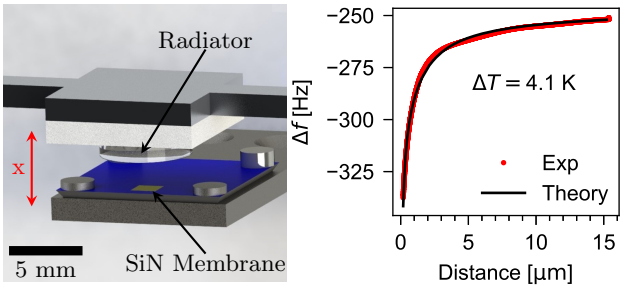

Near-field radiative heat transfer (NFRHT) measurements often rely on custom microdevices that can be difficult to reproduce after their original demonstration. Here we study NFRHT using plain silicon nitride (SiN) membrane nanomechanical resonators—a widely available substrate used in applications such as electron microscopy and optomechanics, and on which other materials can easily be deposited. We report measurements down to a minimal distance of 180 nm between a large radius of curvature (15.5 mm) glass radiator and a SiN membrane resonator. At such deep sub-wavelength distance, heat transfer is dominated by surface polariton resonances over a $(0.25\ \mathrm{mm})^2$ effective area, which is comparable to plane-plane experiments employing custom microfabricated devices. We also discuss how measurements using nanomechanical resonators create opportunities for simultaneously measuring near-field radiative heat transfer and thermal radiation forces (e.g., thermal corrections to Casimir forces).

Near-field radiative heat transfer (NFRHT) has demonstrated great theoretical potential [3, 4, 9–11, 18, 27] for applications such as energy conversion [1, 6, 8, 117, 151] and heat transfer control [9–12]. NFRHT consists of evanescent radiative thermal coupling occurring between two bodies at sub-wavelength distances. This evanescent coupling enables radiative heat transfer exceeding conventional laws of thermal radiation by orders of magnitude [20–22] while being concentrated over a narrow spectral bandwidth [23–26].

Despite this large amount of promising theoretical work, technical challenges of precision alignment at high temperatures often limit experimental progress on NFRHT. Several approaches have been reported to mitigate or overcome experimental difficulties. While some used nanotips [12, 16, 26, 32, 33, 60] or microspheres [34–37, 53, 61, 62] to eliminate the need to maintain parallelism between the coupled surfaces, others relied on more customized designs to study NFRHT between parallel surfaces using active parallelism control [38–46] or custom nanofabricated static device [7, 47–52]. The development of static devices is key for achieving practical application of NFRHT. However,

their custom-fabricated nature makes it difficult to integrate various new materials [13–15, 18, 19, 63, 64] to experimentally study and confirm existing theoretical work on NFRHT. Since the majority of reported NFRHT experiments also employ custom nanodevices [7, 12, 16, 32, 34, 38–41, 47–53], experimental capabilities for investigating new materials for NFRHT remains limited. There is consequently a substantial imbalance between a large body of theoretically investigated phenomena and relatively modest experimental capabilities in the field of NFRHT research.

In an effort to address this imbalance, we previously proposed an alternative [136] where the sensing element—a silicon nitride (SiN) membrane nanomechanical resonator—is a commonly available [163, 164] substrate material onto which other materials are routinely deposited, for example, in transmission electron microscopy. The high mechanical quality factor of these resonators and their high temperature sensitivity notably enabled the demonstration of a temperature resolution (1.2×10^{-6} K) unprecedented in the context of NFRHT measurements [136]. However, we did not achieve NFRHT in the deep sub-wavelength regime—where the thermal radiative heat transfer is dominated by surface polariton (SP) resonances—due to limited flexibility of our preliminary alignment platform (i.e., one-axis alignment, 25 nm step size, open-loop control). Other than potentially allowing material characterization, resonator-based sensing could offer a unique opportunity for measuring thermal radiation forces occurring in the context of near-field radiative heat transfer [89, 146]. SiN resonators already allow, within the framework of optomechanics, strong coupling between radiation forces and mechanical excitation [165]. Likewise, SiN based devices have been used to measure Casimir forces before [135] but not its out-of-equilibrium thermal contribution [146].

In this work, we present SiN membrane resonators as a platform for measuring NFRHT in the deep sub-wavelength regime and quantify their performance limits using a custom-built 5-axis positioning system (see Fig. 4.10a). Our positioning system enables the alignment of two surfaces in the y, z, θ, and ϕ direction, as shown in Fig. 4.10b. The

separation (x) between the two surfaces is controlled by a closed-loop hybrid linear stage (Smaract DLS-5252) that combines the advantages of long travel range (30 mm) stick-slip positioners and high-resolution piezoscanners, enabling a resolution of 1 nm over a 35 µm slip-free range. The y and z positions of the membrane can be modified using open-loop inertia drives (New Focus Picomotor) with 25 nm per step resolution. The θ and ϕ alignment of our platform is controlled by closed-loop stick-slip stages (Smaract SGO-60.5 and SGO-77.5), with 2 µ° resolution.

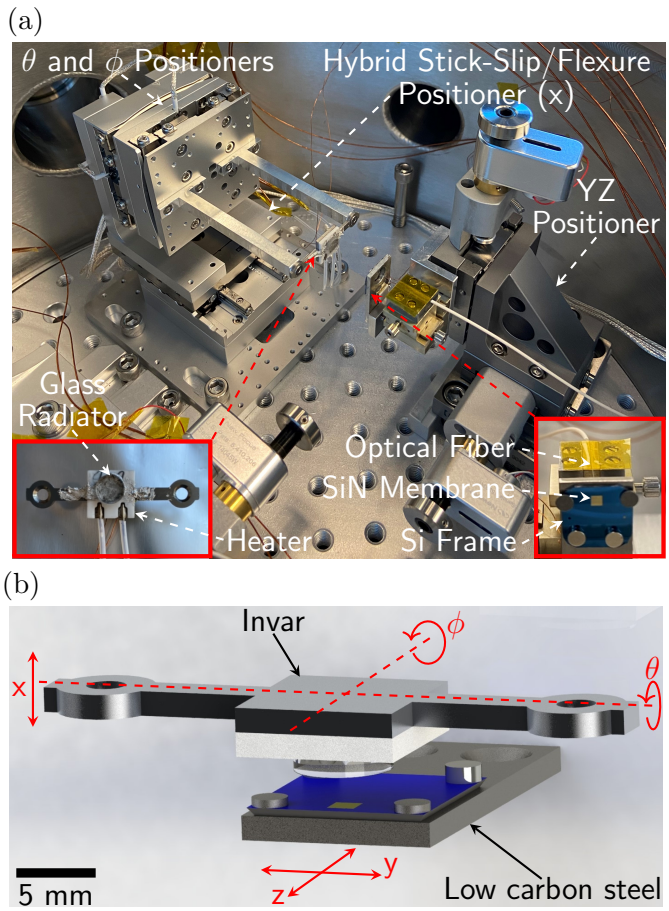

Figure 4.10: (a) NFRHT measurement apparatus inside the vacuum chamber. (b) Render of the NFRHT measurement platform showing both surfaces and the axes of motion used for the positioning. The glass radiator is mounted onto a metal ceramic heater, which is itself mounted on an Invar plate that minimizes required heating power and mechanical deformation. Silver paste is used as a conductive adhesive, which also helps dissipate any spurious electrostatic charges in the glass radiator. The SiN membrane resonator is mounted on a low carbon steel plate using 4 magnets, providing thermal grounding while limiting mechanical damping.

Other than the 5-axis positioning system, our platform relies on relatively simple components that are commercially available. The hot surface of our system is a BK7 glass lens (see Fig. 4.10a) attached to a metal ceramic heater. The large radius of curvature of the glass radiator (15.5 mm), relative to previous probe-tip experiments [12, 16, 26, 32–37, 53, 60–62], allows a large effective near-field heat transfer area (defined later in discussion related to Fig. 4.13c) that is comparable to our membrane size and to previous microscale plate-plate experiments [6, 40, 41, 52, 65, 166, 167]. The metal ceramic heater and spherical radiator are mounted on a custom-machined Invar plate, which, due to its low thermal conductivity and low thermal expansion coefficient compared to other metals, minimizes required heating power and mechanical deformation. The use of a spherical radiator eliminates the need for the θ and ϕ alignment axes in the current experiment, although their use is possible in future plane-plane experiments.

To measure the near-field radiation signal we rely on a low stress SiN membrane (built-in stress ~ 60 MPa, inferred from the mechanical resonance eigenfrequencies) with nominal dimensions of 1.7 mm in side length and $t_{\mathrm{SiN}} = 100$ nm thickness. The SiN membrane used in this platform was fabricated in-house [168], but comparable devices are available commercially [163, 164]. The temperature of the membrane is inferred in real time through an optical interferometer [134, 136] that measures shifts of the membrane mechanical resonance frequency due to thermally induced stress relaxation (i.e., material expansion) [139, 149]. The membrane resonance frequency is tracked by phase locking (PLL) the internal oscillator of a lock-in amplifier (Zurich Instrument MFLI) to the membrane eigenfrequency [157]. The lock-in oscillator signal (set to an amplitude of 80 mV) is sent to a piece of piezoelectric ceramic (Thorlabs shear piezoelectric chip, PN:PL5FBP3) that actuates the membrane at its resonance frequency by acoustic coupling through the membrane-chip mount. The silicon frame of the membrane is mounted on a low carbon steel support (see Fig. 4.10b) using 4 magnets, enabling good thermal contact for maintaining the silicon frame at room temperature, while limiting

the mechanical damping compared to adhesive mounting. To suppress fluidic damping and convective heat transfer, the system is placed in a custom-designed high-vacuum chamber operating at a typical pressure of 2×10^{-6} Torr.

We predict the NFRHT signal between the radiator and the membrane using a model—discussed in greater detail in Supporting Information Section 4.2.4.1 and Ref. 136—that combines the heat diffusion equation inside the membrane (Eq. 4.34) [66], multilayer NFRHT calculations [5, 93], and the mechanical effects of nonuniform stress in the resonator obtained by solving the motion equation (Eq. 4.36) [137]. Far-field radiative heat transfer between the back side of the membrane and the surrounding is computed using conventional radiative heat transfer for small objects with large surroundings [82]. Far-field radiative heat transfer between the front side of the membrane and the radiator is calculated using the conventional far-field thermal radiation formalism [82] including geometrical view factors. In the near-field, we account for the curvature of the glass radiator using the proximity approximation (also known as the Derjaguin approximation [97]) shown in Eq. 4.22. The permittivity of the glass radiator is taken from Ref. 129 and that of SiN is taken from Ref. 127.

Using this model, we compute a relative frequency sensitivity ($\Delta f/f_0$) of the membrane to temperature (and absorbed radiation) of -7400 ± 900 ppm/K (-710 ± 90 ppm/μW), under far-field radiation. With a fundamental eigenmode frequency of ~ 58.5 kHz for our current membrane, the absolute frequency sensitivity is -433 ± 53 Hz/K (-41 ± 5 Hz/μW). In the near-field, these numbers change slightly due to a different temperature spatial distribution in the membrane. For example, at 200 nm near-field distance, the sensitivity is evaluated at -449 ± 55 Hz/K (-45 ± 5.5 Hz/μW) for our radiator geometry. The uncertainties result from the uncertainties in the material constants of SiN ($\alpha = 2.2 \pm 0.1 \times 10^{-6}$ K^{-1} [169–171], $\nu = 0.27 \pm 0.03$ [169, 171, 172], $E = 300 \pm 30$ GPa [169–173], and $\rho = 3100 \pm 100$ kg/m^3 [169, 171, 173]), for which values are not reported with more than two significant figures. Here α is the coefficient of thermal expansion, ν

is the Poisson ratio, E is the Young modulus, and ρ is the density.

In the current geometry, mechanical frequency shifts due to Casimir forces are predicted to be much smaller than those due to NFRHT. The Casimir force (F_{cas}) and spring constant ($k_{\mathrm{cas}} = \partial F_{\mathrm{cas}}/\partial x$) are computed in Supporting Information Section 4.2.4.2 using the model in Ref. 146. At a typical separation achieved in this work ($\sim$ 200 nm), the estimated shift (Δf_{cas}) of resonance frequency (f_0) due to Casimir forces is $\frac{\Delta f_{\mathrm{cas}}}{f_0} \approx \frac{k_{\mathrm{cas}}}{8\pi^2 m_{\mathrm{eff}} f_0^2} \approx 20$ ppm. In comparison, typical temperature-induced frequency shifts (see Fig. 4.11c) are on the order of 1300 ppm. We therefore neglect Casimir forces in the current work. However, we note that shifts on the order of 20 ppm can typically be resolved by our SiN membrane sensors, which have demonstrated stability smaller than 0.01 ppm in Ref. 67. If we can distinguish the contributions to frequency shifts due to Casimir and to NFRHT, our approach could provide a unique opportunity for measuring the never-demonstrated corrections to Casimir forces out of thermal equilibrium [146].

During the experiment, the proportional, integral, and derivative (PID) parameters of our closed-loop x-axis positioning system (see Fig. 4.10b) are set to an overdamped mechanical response, preventing overshoot and oscillations of the positioner. This slow overdamped response also enables sampling of multiple temperature readings during displacement between two set points. During a typical $\tau_{\mathrm{positioner}} \sim 2$ s displacement between two set points, as shown in Fig. 4.11a, the membrane temperature is sampled 3350 times, yielding a temperature sampling every ~ 0.1 nm, even though the distance between the set points is 100 nm. We consider that the membrane remains in quasi-steady-state during these displacements since its characteristic thermal response time ($\tau_{\mathrm{th}} \approx 0.066$ s [140]) is much smaller than the positioner response time ($\tau_{\mathrm{positioner}} \sim 2$ s). For even finer approaches, we use the same procedure but in 10 nm steps instead of 100 nm. These finer steps are typically used at smaller separation ($\lesssim 3\,\mu$m) to prevent accidental contact.

Transverse alignment (i.e., in YZ) of the apex of the glass radiator with the center

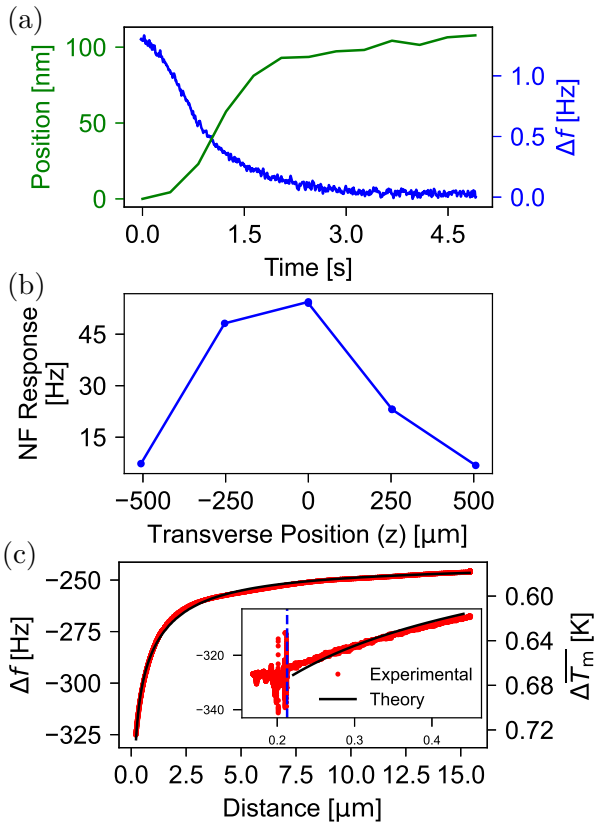

Figure 4.11: (a) Overdamped displacement response of the hybrid positioner as a function of time (in green). The frequency data (in blue) illustrates how we sample approximately 3350 points during a displacement between two set points separated by 100 nm. (b) Near-field (NF) response as a function of the transverse radiator position (z) demonstrating how we align the radiator apex with the membrane. The optimal position (where the near-field signal is maximized) is located at a z position of 0 µm with an uncertainty of ±125 µm. (c) Experimental (red) and theoretical (black) (fitted horizontally and vertically) resonance frequency shift as a function of separation for a $\Delta T = 4.0$ K temperature difference between the membrane and radiator. The fit suggests a minimal separation of ~ 210 nm. The initial shift of ~ 250 Hz at large distances results from the far-field radiative coupling. Inset: fluctuations at smaller distances lead to loss of mechanical resonance, past the minimum gap of 210 nm. The dotted blue line identifies the position at which the resonance is lost.

of the membrane is critical for maximizing the membrane response to near-field radiation. Misalignment was the main limiting factor in our original 1-axis positioner concept demonstration [136], but it is now no longer an issue with our 5-axis alignment platform. As the apex of the glass radiator is misaligned from the membrane center position, it becomes increasingly coupled to the silicon frame, thus, greatly reducing the near-field

signal measured by the membrane. We rely on this effect to align the glass radiator apex with the membrane center. While actively recording the membrane frequency, we moved the glass radiator forward until the membrane mechanical resonance is lost. We then retracted the glass radiator by 15 µm. Afterward, we use our Y (and Z) stage to adjust the horizontal (and vertical) positions of the hot surface by 250 µm and repeat the approach procedure while measuring the near-field signal. We repeat this procedure until the near-field radiation signal—i.e., the frequency shift before loss of resonance—is maximized (see Fig. 4.11b). Once this procedure is completed, the apex of the glass radiator is aligned with the center of the membrane with an estimated accuracy of ±125 µm. With such uncertainty, our model [136] predicts negligible near-field signal degradation (less than 1% attenuation of the temperature signal compared to perfect alignment). We note that, due to the low temperature difference between the two surfaces ($\Delta T = 4.1$ K for the measurement in Fig. 4.11b), measuring the small shifts in temperature induced by 250 µm misalignments ($\Delta T_{\mathrm{m}} \approx 0.014$ K) requires a high-resolution radiation sensor, like the SiN membrane (1.2×10^{-6} K [136]) employed here.

Comparison of measured data with the model described above (Fig. 4.11c, Fig. 4.12) suggests that we reach a minimal distance $d_{\mathrm{min}} = 180$ nm (see $\Delta T = 4.1$ K scan in Fig. 4.12) between the membrane and the hot surface before we lose track of the membrane mechanical resonance (see typical loss of tracking in Fig. 4.11c inset). The fit of the experimental data to the theoretical model accounts for three unknowns: (1) the radiator-membrane initial (far-field) distance, (2) the uncertainty of the far-field radiation intensity caused by the variety of materials present around the radiator (see Fig. 4.10a inset), and (3) the temperature at the surface of the glass radiator. In Fig. 4.11c, shifting the experimental data along the distance (horizontal) axis accounts for the first unknown. Likewise, shifting along the frequency shift (vertical) axis accounts for the second unknown while also correcting for slow frequency drift due to ambient temperature variation in the vacuum chamber. Finally, for the third unknown, fitting of the glass radiator sur-

face temperature in the theoretical model results in an $\sim 50\%$ reduction compared to the temperature measured inside the metal ceramic heater. This reduction is most likely due to heat dissipation in the metal mount (see Fig. 4.10b).

Our platform currently enables scans at temperature differences up to $\Delta T = 25.5$ K ($T_{\mathrm{Rad}} = 322.5$ K and $T_{\mathrm{m}} = 297.0$ K), which is comparable to other macroscale NFRHT platforms reviewed in Ref. 65. For all scans with $\Delta T \leq 25.5$ K, the tip of the radiator reaches deep sub-wavelength distances (see d_{min} values in Fig. 4.12) where the thermal radiative heat transfer is dominated by SP resonances. Compared to previous membrane work, a smaller membrane (1.7 mm vs 3 mm in Ref. 136) was found to enable measurements at higher temperatures (25.5 K vs 10 K in Ref. 136). The smaller membrane resulted in a better thermal ground from the silicon frame, allowing the membrane temperature to remain lower and less affected by far-field radiation. Still, the large size of our radiator is eventually limiting the maximum reachable temperature difference in our NFRHT measurement, as is also the case in other macroscale platforms [65]. At temperature differences greater than 25.5 K, fluctuations and drift, induced by parasitic heating of the surroundings, eventually prevent continuous tracking of the membrane resonance frequency. This issue could possibly be mitigated by use of high-stress SiN resonators that are less temperature sensitive, or by using smaller heaters/membranes that produce/capture less parasitic far-field radiation.

Due to the high resolution of our radiation sensor and positioning system, the accuracy of our minimum-distance results (d_{min} in Fig. 4.12) is limited mainly by the uncertainty on material constants of SiN. During a sampling time typical of the displacement time between two set points (~ 2.5 s), the root-mean-square fluctuations of the x-axis position and frequency shift are, respectively, 3.6 nm and 0.026 Hz. These small fluctuations result in virtually noise-free curves (see Fig. 4.11c and Fig. 4.12) that can be fitted with our theoretical model to find the minimum distance achieved with a negligible influence from fluctuation noise. In contrast, the minimum distance extracted from this

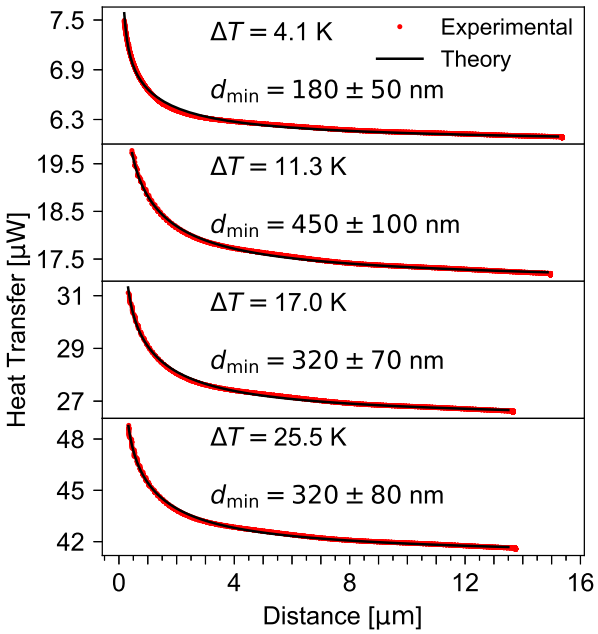

Figure 4.12: Experimental (red) and theoretical (black) (fitted horizontally and vertically) radiative heat transfer as a function of separation for different radiator-membrane temperature differences (ΔT) showing good correspondence with the theoretical model. The comparison with the theoretical model suggests that we have reached the deep subwavelength regime for all ΔT values. The minimal separation $d_{\min}$ achieved is identified in each plot.

fit varies strongly with the uncertainties for the material constants of SiN (α, ν, E, ρ). These propagated uncertainties result in a 50 nm uncertainty of the minimal distance achieved, for a 4.1 K temperature difference. More information on uncertainty calculation is presented in Supporting Information: (Section 4.2.4.3) position and frequency stability analysis, (Section 4.2.4.4) separate optical measurement of the positioner response, and (Section 4.2.4.5) propagation of uncertainty between SiN material constants and minimum distance achieved.

Reaching minimal distances in the 180-450 nm range (see Fig. 4.12) implies that we transitioned into a regime where the radiative heat transfer is quasi-monochromatic, as is desirable in most NFRHT applications. As shown in Fig. 4.13a and Fig. 4.13b the calculated spectral radiative heat flux, at 180 nm and $\Delta T = 4.1$ K, is dominated by a transverse magnetic polarization resonance at an angular frequency of $\omega = 9.24 \times 10^{13}$ rad/s.

This resonance originates from surface polariton (SP) resonances in the glass radiator, since its parallel wavevector k_ρ exceeds both material light lines (given by $\mathrm{Re}(n)k_\mathrm{v}$ [174], where k_v is the magnitude of the wavevector in vacuum and n is the refractive index of the material). In Fig. 4.13c, we quantify the contribution of each of the components of the radiative heat flux at the tip of the radiator as a function of the separation. A similar analysis for the heat flux over the full area of the resonator is available in Supporting Information Section 4.2.4.6. At a separation of 180 nm, the SP reaches a contribution of $91.4 \pm 4\%$ at the tip of the radiator, where the heat flux is therefore dominated by SP modes. We also show in Supporting Information Section 4.2.4.7 that the 100 nm thickness of the membrane enhances the relative polariton contribution to heat transfer by a factor of 30% compared to bulk SiN, at a separation of 180 nm. Temperature-independent versions of the plots in Fig. 4.13a and Fig. 4.13b are also reproduced in Supporting Information Section 4.2.4.8 (i.e., the mode transmission only, not weighted by the Plank mean oscillator energy). Plots of the spectral heat flux for all gaps reported in Fig. 4.12 can also be found in Supporting Information Section 4.2.4.9.

Considering the minimal distances (d_min) achieved and the contribution of each radiative heat flux component (Fig. 4.13c), we infer a deep sub-wavelength effective area of $(0.25\ \mathrm{mm})^2$ and a near-field heat transfer effective area of $(0.96\ \mathrm{mm})^2$. We define the former as the projected area of the radiator (at the apex) that is closer than 825 nm to the membrane (i.e., the distance in Fig. 4.13c where the SP contribution becomes dominant). Interestingly, the resulting $(0.25\ \mathrm{mm})^2$ is comparable to microscale plate-plate NFRHT experiments [6, 40, 41, 52, 65, 166, 167]. Within this area, the total heat transfer is enhanced by a factor of 9 over the far-field intensity (see extended discussion in Supporting Information Section 4.2.4.6). We also note that membranes with areas of $(0.25\ \mathrm{mm})^2$ are a standard commercial product [164]. With such dimension, the entirety of the membrane area could be deep sub-wavelength-coupled to our radiator, as in a plate-plate experiment but without the need for θ, ϕ alignment. Predicted results for

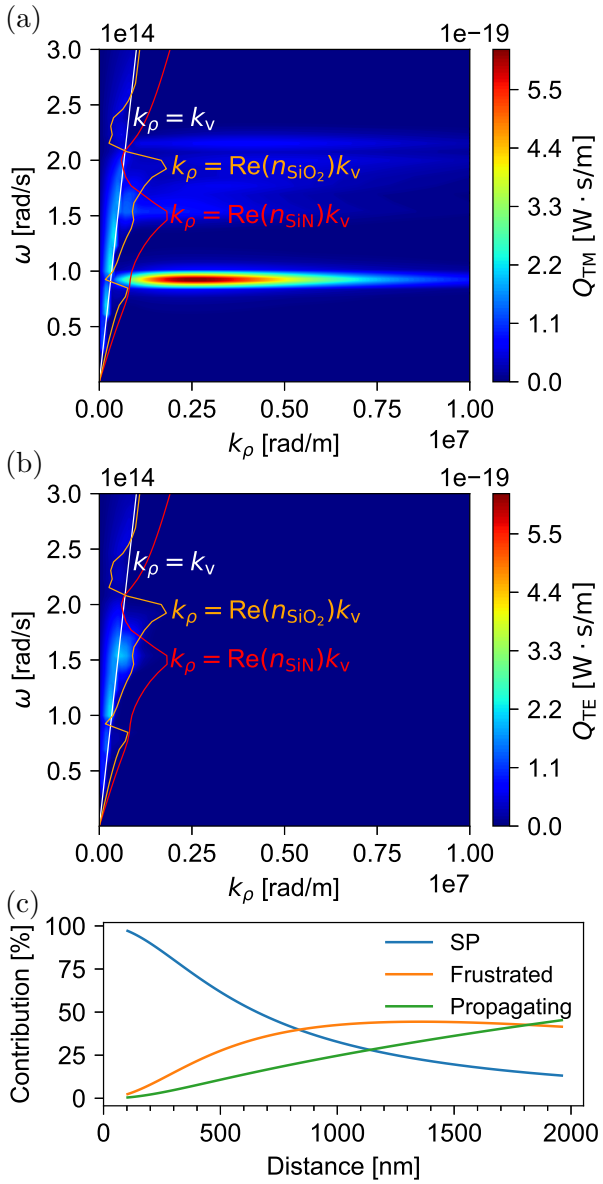

Figure 4.13: (a, b) Calculated radiative heat flux, at the radiator apex, per unit angular frequency, ω, and parallel wavevector, k_ρ, at 180 nm separation and a temperature difference of 4.1 K for (a) transverse magnetic (TM) and (b) transverse electric (TE) polarization. The propagating modes ($k_\rho < k_v$) and the frustrated modes ($k_v < k_\rho < \min\left(\mathrm{Re}(n_{SiO_2})k_v, \mathrm{Re}(n_{SiN})k_v\right)$) have modest contributions (1.8% and 6.8%, respectively), while the SP mode ($k_\rho > \min(\mathrm{Re}(n_{SiO_2})k_v, \mathrm{Re}(n_{SiN})k_v)$) (accounting for 91.4% of the total radiative heat flux) is the dominating mode. (c) Contribution of each of the components of the radiative heat flux, at the tip of the radiator, as a function of distance for a 4.1 K temperature difference.

such membrane size are presented in Supporting Information Section 4.2.4.6, showing that in this case SP contributions largely dominate over propagating mode contributions over the full area of the resonator. Conversely, we obtain the $(0.96\ \text{mm})^2$ area by calculating the projection of the radiator apex that is within a distance smaller than Wien's wavelength ($\lambda_{\text{Th}} = 9.7\,\mu\text{m}$) from the membrane (i.e., the distance where near-field enhancement starts occurring due to frustrated waves). The resulting $(0.96\ \text{mm})^2$ is significantly larger than in all previous sphere-plane experiments [34–37, 53, 61, 62], while also being comparable to our membrane size (1.7 mm side length).

Several factors could explain why we cannot measure near-field heat transfer at radiator-membrane distances below 180 nm. From Fig. 4.11c, we note that, after mechanical resonance is intermittently lost, tracking of the frequency still averages over values that follow the general near-field trend. It is therefore possible that contact did not occur between the membrane and radiator, but that something else causes loss of frequency tracking. This hypothesis is strengthened by measurement of the surface flatness of the radiator and SiN (Fig. 4.14), which show no asperities large enough for preventing near-field alignment beyond 180 nm. In Fig. 4.14a, particles are detected on SiN, which are probably due to the fabrication process. Fig. 4.14b shows the presence of longer engraved patterns on the surface of the radiator. Both are, however, much smaller than 180 nm.

Reasons, other than contact, that could cause a loss of frequency tracking are numerous and present interesting investigation directions. We first note that the resonator vibration amplitude (set to $\sim$ 2 nm in the far-field by a 80 mV constant-amplitude modulation) sometimes drops (by up to 90%) as the system transitions from far-field to near-field coupling, making resonator frequency more difficult to track. This vibration dampening could originate either from parasitic effects (e.g., trapped charges on the membrane and/or radiator) or phenomena such as delayed thermal-Casimir forces [146] or bolometric backaction [175]. Additionally, in the deep sub-wavelength regime, spurious fluctuations of the membrane-radiator distance are strongly coupled to the membrane

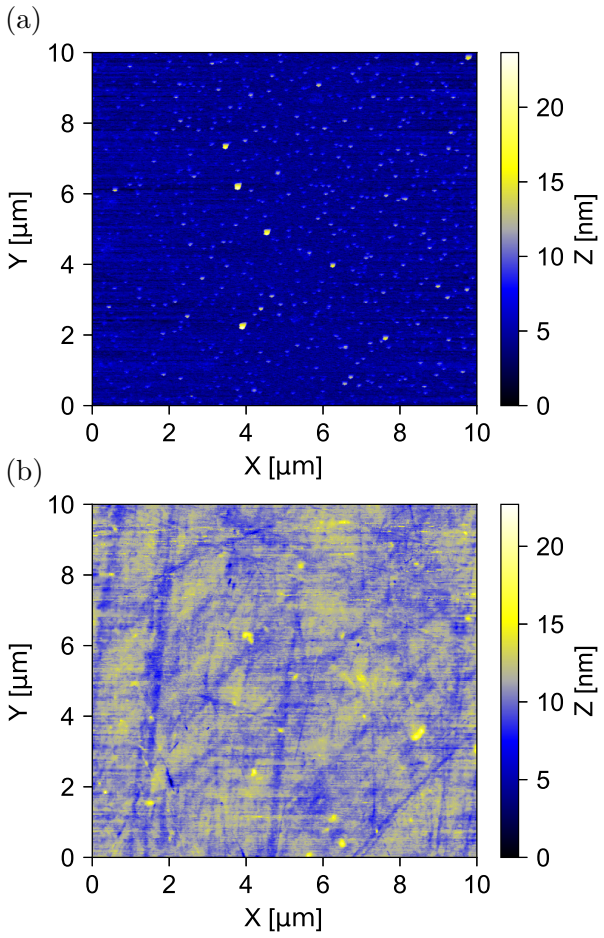

Figure 4.14: Atomic force microscopy measurements of (a) the SiN layer and (b) the radiator over a 100 µm^2 surface area. Roughness on the order of $\sim$ 24 and $\sim$ 23 nm is observed in respective samples. SiN measurements are taken on SiN supported by the Si frame (i.e., not on the structurally released SiN) to prevent membrane destruction.

temperature (and hence to resonance frequency), potentially affecting PLL frequency tracking. Sources of such distance fluctuations include resonator actuation ($\sim$ 2 nm), fluctuation of the positioner (measured optically to $\sim$ 2.5 nm over a 25 Hz bandwidth, see Supporting Information Section 4.2.4.4), and thermomechanical fluctuation noise in the membrane ($\langle x \rangle = \sqrt{\frac{k_B T}{m_{\text{eff}} \omega_0^2}} = 0.012$ nm). It is possible that smaller membrane dimensions (i.e., resulting in a stiffer membrane) could reduce several of these spurious effects (e.g., fewer trapped charges, fewer thermomechanical fluctuations, less deformation due to stiction forces). This remains to be confirmed experimentally but could allow measurement limited by the surface quality of our materials (i.e., at gaps $<$ 50 nm according

to Fig. 4.14).

We have demonstrated that widely available SiN membrane resonators can enable near-field radiative heat transfer measurement in the deep sub-wavelength regime, over a $(0.25\ \text{mm})^2$ effective area, without custom nanofabricated devices. Such membrane size is widely available and can be used in future work to achieve deep sub-wavelength NFRHT measurement without the need for custom fabricated microdevices. We therefore expect that the reproducibility and flexibility of our platform will facilitate investigation of new materials for NFRHT—such as graphene [63], thin-film metals [13], multilayers [64], lossy materials [18], hyperbolic materials [14, 19], and metamaterials [15]—which can all be easily deposited on SiN membranes. The fact that nanomechanical resonators are sensitive to both force and temperature also creates an opportunity to investigate thermal corrections to the Casimir effect.

Associated Content

The Supporting Information is available free of charge at `https://pubs.acs.org/doi/10.1021/acs.nanolett.3c02049`.

> Theoretical model for mechanical frequency shifts due to NFRHT; Casimir forces estimation; stability analysis of positioner and SiN frequency; optical verification of the positioner displacement; uncertainty analysis; relative contributions of propagating, frustrated, and surface modes to total heat transfer; hybridization of surface polariton resonances in thin film SiN; Radiative heat transfer transmission coefficients; spectral distribution of radiative heat transfer.

Acknowledgments

This work was funded by the Natural Sciences and Engineering Research Council of Canada (No. NSERC CGS-D and No. NSERC 497981), the Ontario Graduate Scholarship (OGS), the New Frontiers in Research Fund (No. NFRFE-2019-00334), and by start-up funds from the Faculty of Engineering at the University of Ottawa.

4.2.4 Supplementary Information

4.2.4.1 Theoretical Model for Mechanical Frequency Shifts due to Near-Field Radiative Heat Transfer

In our model, the near-field radiative heat transfer (NFRHT) coupling of evanescent waves is computed using the NFRHT algorithm described in Ref. 5. For these calculations, the permittivity of the glass radiator is taken from Ref. 129 and that of SiN is taken from Ref. 127. We rely on the proximity approximation (also known as the Derjaguin approximation [97]) to account for the curvature of the glass radiator. This approximation is proven to be valid for NFRHT [35], especially for relatively large objects such as the glass radiator. Each point on the curved surface is approximated to a flat surface for which the distance from the membrane is

$$d(r) = d_0 + R - \sqrt{R^2 - r^2}, \tag{4.22}$$

where d_0 is the distance at the radiator apex and R is the radius of curvature of the radiator.

The far-field radiative heat transfer between the back side of the membrane and the surroundings $\dot{q}_{\mathrm{FF_{back}}}$ is computed using conventional radiative heat transfer for small objects with large surroundings [82],

$$\dot{q}_{\mathrm{FF_{back}}}(r) = \epsilon_{\mathrm{SiN}}\sigma\left(T_\infty^4 - T_{\mathrm{m}}^4(r)\right)/t_{\mathrm{SiN}} \tag{4.23}$$

where σ is the Stephan-Boltzmann constant, $T_\infty = 293$ K is the environment temperature, $T_{\mathrm{m}}(r)$ is the temperature profile of the membrane, t_{SiN} is the thickness of the SiN membrane, and ϵ_{SiN} is the emissivity of SiN, taken from Ref. 66. Here we divide the radiative heat transfer by the thickness of the SiN membrane to obtain a quantity in unit volume.

The far-field radiative heat transferred to the front side of the membrane $\dot{q}_{\mathrm{FF}_{\mathrm{front}}}$ is computed using the conventional far-field thermal radiation formalism [82] including geometrical view factors. We approximate our platform to the equivalent thermal circuit shown in Fig. 4.15, from which we can compute the radiative heat transfer between the three surfaces: the glass radiator (point A), the membrane (point B), and the surroundings (point 3). Here the surroundings are approximated to a blackbody.

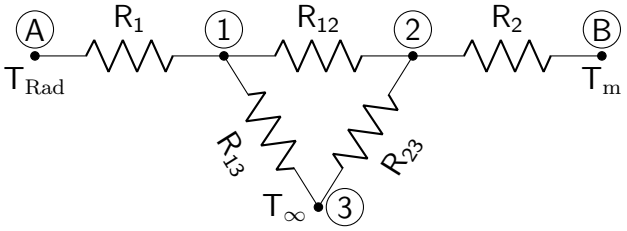

Figure 4.15: Equivalent thermal circuit for the far-field radiation between the glass radiator (point A), the membrane (point B) and the surroundings (point 3). R_1 and R_2 are, respectively, the surface resistances of the radiator and membrane and R_{12}, R_{13}, and R_{23} are the space resistances accounting for the view factors.

The surface resistance of the glass radiator R_1 and of the SiN membrane R_2 can be computed as [82]:

$$R_1 = \frac{1-\epsilon_{\mathrm{Glass}}}{A_1\epsilon_{\mathrm{Glass}}} \qquad \text{and} \qquad R_2 = \frac{1-\epsilon_{\mathrm{SiN}}}{A_2\epsilon_{\mathrm{SiN}}}, \tag{4.24}$$

where $\epsilon_{\mathrm{Glass}}$ is the emissivity of the glass radiator, A_1 is the surface area of the radiator (in this case we use the surface area of a full sphere to agree with the view factor model), and A_2 is the surface area of the SiN membrane. The space resistance R_{ij} between the surfaces are given as:

$$R_{ij} = \frac{1}{A_i F_{ij}}, \tag{4.25}$$

where F_{ij} is the view factor between surface i and surface j. The view factor from the radiator to the SiN membrane F_{12} is computed using the tabulated relations from

Ref. 176. We approximate our platform to a sphere-disk configuration for which the view factor F_{12} can be expressed as:

$$F_{12} = \frac{1}{2}\left(1 - \frac{1}{\sqrt{1+\frac{1}{h^2}}}\right), \tag{4.26}$$

where $h = \frac{d_0+R}{r_{\text{eff}}}$. Using the principle of reciprocity and the enclosure summation, one can compute the view factors F_{21}, F_{13}, and F_{23} as follows:

$$F_{21} = \frac{A_1 F_{12}}{A_2}, \qquad F_{13} = 1 - F_{12}, \qquad F_{23} = 1 - F_{21}. \tag{4.27}$$

The potential applied to the circuit, at nodes A, B, and 3, is equivalent to the black-body emissive power E_{b};

$$E_{\text{bA}} = \sigma T_{\text{Rad}}^4, \qquad E_{\text{bB}} = \sigma T_{\text{m}}^4, \qquad E_{\text{b3}} = \sigma T_{\infty}^4, \tag{4.28}$$

where T_{Rad} is the temperature of the radiator. Applying the Kirchhoff current law at nodes 1 and 2 yields the following relations:

$$\frac{E_{\text{bA}} - P_1}{R_1} + \frac{P_2 - P_1}{R_{12}} + \frac{E_{\text{b3}} - P_1}{R_{13}} = 0, \tag{4.29}$$

$$\frac{E_{\text{bB}} - P_2}{R_2} + \frac{P_1 - P_2}{R_{12}} + \frac{E_{\text{b3}} - P_2}{R_{23}} = 0, \tag{4.30}$$

where P_1 and P_2 are the potentials at node 1 and node 2, respectively. Using the relations described in Eq. 4.29 and Eq. 4.30, we can derive a relation for the potential at node 2

$$P_2 = \frac{\begin{array}{c} E_{\mathrm{bA}}R_{13}R_2R_{23} + E_{\mathrm{bB}}R_1R_{12}R_{23} + E_{\mathrm{bB}}R_1R_{13}R_{23} + E_{\mathrm{bB}}R_{12}R_{13}R_{23} \\ + E_{\mathrm{b3}}R_1R_{12}R_2 + E_{\mathrm{b3}}R_1R_{13}R_2 + E_{\mathrm{b3}}R_1R_2R_{23} + E_{\mathrm{b3}}R_{12}R_{13}R_2 \end{array}}{\begin{array}{c} R_1R_{12}R_2 + R_1R_{12}R_{23} + R_1R_{13}R_2 + R_1R_{13}R_{23} \\ + R_1R_2R_{23} + R_2R_{12}R_{13} + R_{12}R_{13}R_{23} + R_{13}R_2R_{23} \end{array}}. \tag{4.31}$$

Finally, by applying Ohm's law at resistance R_2, one can compute the radiative heat absorbed at the front side of the membrane by unit volume $\dot{q}_{\mathrm{FF}_{\mathrm{front}}}$

$$\dot{q}_{\mathrm{FF}_{\mathrm{front}}} = \frac{P_2 - E_{\mathrm{bB}}}{R_2 t_{\mathrm{SiN}}}. \tag{4.32}$$

The total thermal radiative heat transfer can be computed by combining the three components discussed so far: G_{NF} representing the NFRHT coupling of evanescent waves, $\dot{q}_{\mathrm{FF}_{\mathrm{back}}}$ representing the far-field radiation to the back side of the membrane, and $\dot{q}_{\mathrm{FF}_{\mathrm{front}}}$ representing the far-field radiation to the front side of the membrane. Therefore, the total heat flux is considered as an internal generation term $\dot{q}_{\mathrm{gen}}$ which is computed as

$$\dot{q}_{\mathrm{gen}}(r, T_{\mathrm{m}}) = G_{\mathrm{NF}}(r, T_{\mathrm{m}}) \cdot (T_{\mathrm{Rad}} - T_{\mathrm{m}}(r))/t_{\mathrm{SiN}} + \dot{q}_{\mathrm{FF}_{\mathrm{front}}}(T_{\mathrm{m}}(r)) + \dot{q}_{\mathrm{FF}_{\mathrm{back}}}(T_{\mathrm{m}}(r)). \tag{4.33}$$

Using this internal generation term, we numerically solve the heat diffusion equation, in the form of Eq. 4.34, in MATLAB®, using finite element method to obtain the membrane temperature profile $T_{\mathrm{m}}(r)$.

$$k_{\mathrm{SiN}} \nabla^2 T_{\mathrm{m}}(r) + \dot{q}_{\mathrm{gen}}(r, T_{\mathrm{m}}) = 0, \tag{4.34}$$

where k_{SiN} is the thermal conductivity of SiN. With the obtained membrane temperature profile, we can compute the position-dependent component of the in-plane stress σ_r using Eq. 4.35 [138].

$$\sigma_r(r, T_\mathrm{m}) = -\alpha E\left[\frac{1}{r^2}\int_0^r r\Delta T_\mathrm{m}(r)\mathrm{d}r + \frac{1+\nu}{1-\nu}\frac{\Delta\overline{T_\mathrm{m}}}{2}\right], \tag{4.35}$$

where α is the thermal expansion coefficient of SiN, E is the Young modulus, ν is the Poisson ratio, $\Delta T_\mathrm{m} = T_\mathrm{m} - T_\infty$, and $\Delta\overline{T_\mathrm{m}} = \overline{T_\mathrm{m}} - T_\infty$ where $\overline{T_\mathrm{m}}$ denotes the temperature average over the membrane area.

Finally, we compute the resonance frequency shift of our SiN membrane by solving the motion equation of a thin membrane under tensile stress,

$$\frac{1}{r}\frac{\partial}{\partial r}\left(\left(\sigma_0 + \sigma_r(r, T_\mathrm{m}(r))\right) r\frac{\partial u(r,t)}{\partial r}\right) - \rho\frac{\partial^2 u(r,t)}{\partial t^2} = 0, \tag{4.36}$$

where σ_0 is the built-in stress at room temperature, ρ is the density of SiN, and $u(r,t)$ is the out-of-plane displacement of the membrane. More precisely, we numerically solve the motion equation in MATLAB® using finite element method and compute the eigenvalues to obtain the resonance frequency. Note that we are solving the motion equation in spherical coordinates since we approximate our square membrane of side length $L = 1.7$ mm to a circular membrane of radius $r_\mathrm{eff} = 1.252\frac{L}{2} = 1.0642$ mm. This approximation is proven to be valid to accurately estimate the thermal coupling properties of square membranes [66].

4.2.4.2 Casimir Forces Estimation

In this section we estimate Casimir forces and their effect on measurements. We compute the Casimir force using the algorithm described in Ref. 146 which includes the out of equilibrium thermal contribution. Since we are using a curved surface, we rely on the proximity approximation [97] to compute the Casimir forces over the entire surface area of the resonator. The results can be observed in Fig. 4.16 where the Casimir force is plotted as a function of the distance. At our minimal distance of 180 nm, an attractive force of about 115 pN acts on the resonator.

To compute the effective spring constant ($k_\mathrm{cas} = \frac{\partial F_\mathrm{cas}}{\partial x}$) induced by the Casimir forces

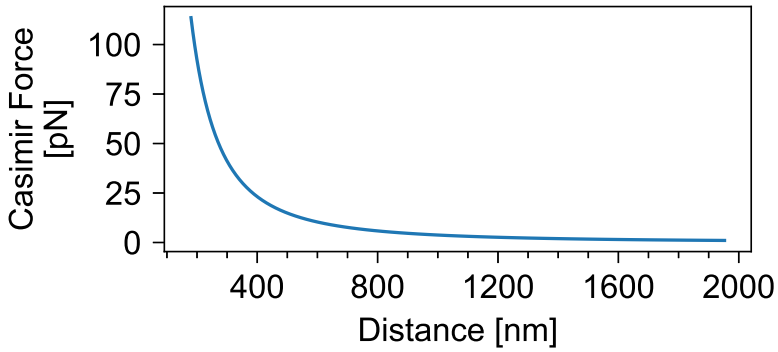

Figure 4.16: Casimir force as a function of distance for a 4.1 K temperature difference.

F_{cas} on the resonator, we performed the numerical derivative of the data showed in Fig. 4.16 with respect to the distance x. We plot the results in Fig. 4.17 which shows that, at a distance of 180 nm, the spring constant is $k_{\text{cas}} = 1.2 \times 10^{-3}$ N/m.

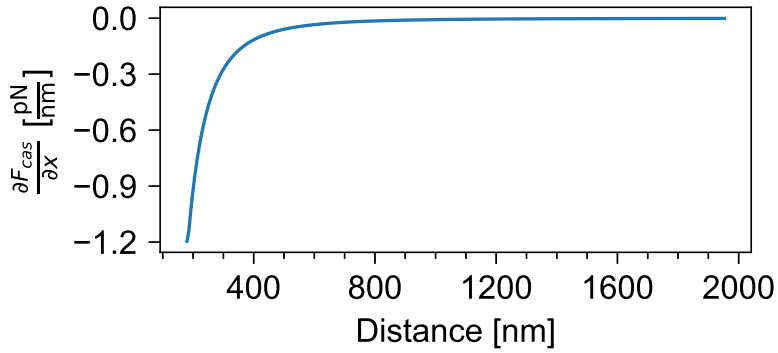

Figure 4.17: Numerical derivative of the Casimir force with respect to the distance $\frac{\partial F_{\text{cas}}}{\partial x}$ as a function of distance x for a 4.1 K temperature difference.

To predict the effect of k_{cas} on the resonator eigenfrequency, we use the conventional formula for the natural frequency of a resonator ($f = \frac{1}{2\pi}\sqrt{\frac{k}{m}}$) and apply a linearization ($\partial f \approx \Delta f$ and $\partial k \approx \Delta k$):

$$\frac{\Delta f}{f_0} = \frac{1}{2}\frac{\Delta k}{k},$$

where Δf is the frequency shift due to the Casimir forces, $f_0 \approx 58.5$ kHz is the room temperature resonant frequency, $\Delta k = k_{\text{cas}}$ would be the change in the spring constant due to the Casimir forces, and k would be the effective spring constant of the resonator

which is given by:

$$k = 4\pi^2 m_{\text{eff}} f_0^2$$

where $m_{\text{eff}} = \frac{1}{4} m_0$ is the effective mass of the resonator, with $m_0 = \rho L^2 t_{\text{SiN}} = 8.96 \times 10^{-10}$ kg. Using these relations we can derive the frequency shift due to the Casimir forces as:

$$\Delta f = \frac{k_{\text{cas}}}{2\pi^2 m_0 f_0}$$

$$\Delta f = \frac{1.2 \times 10^{-3}}{2\pi^2 \cdot 8.96 \times 10^{-10} \cdot 58500} = 1.2 \text{ Hz}$$

In comparison, we measure frequency shifts on the order of 75 Hz due to NFRHT. We can therefore neglect Casimir forces in this work. We note however that 1.2 Hz is typically a resolvable quantity using our SiN resonator sensors [67]. Casimir forces could therefore be measured if we can somehow distinguish them from the thermally-induced frequency shifts caused by NFRHT.

4.2.4.3 Stability Analysis of Positioner and SiN Frequency

In this section, we analyze the standard deviation of the measured resonance frequency and position. We compute the standard deviation over a 2.5 second sample (after reaching stability) of our measurement at each displacement, as illustrated in Fig. 4.18.

For the positioner, the standard deviation of the signal from the positioner optical encoder yields a median value of 3.6 nm. Likewise, the standard deviation of the membrane frequency yields a median value of 0.026 Hz, equivalent to 438 pW of heating power. Since these values are much smaller than the uncertainty resulting from the material constants, we consider their impact to be negligible and do not include these values in our uncertainty analysis.

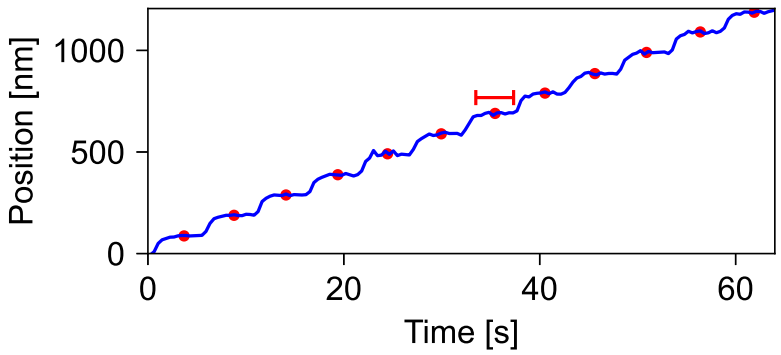

Figure 4.18: Illustration of the sampling period of 2.5 seconds centered at the midpoint of the stable plateau after each displacement.

4.2.4.4 Optical Verification of the Positioner Displacement

In this section, we show optical measurement of the positioner response performed with an optical interferometer. An optical fiber pointed at a reflective surface of the positioner was used to measure the interference signal resulting from the displacement of the positioner. In Fig. 4.19, we show the optical signal measured as we ask the positioner to make 5 nm steps in open-loop mode. The data in Fig. 4.19, measured while using a 25 Hz bandwidth, shows fluctuations of ~ 2.5 nm in amplitude.

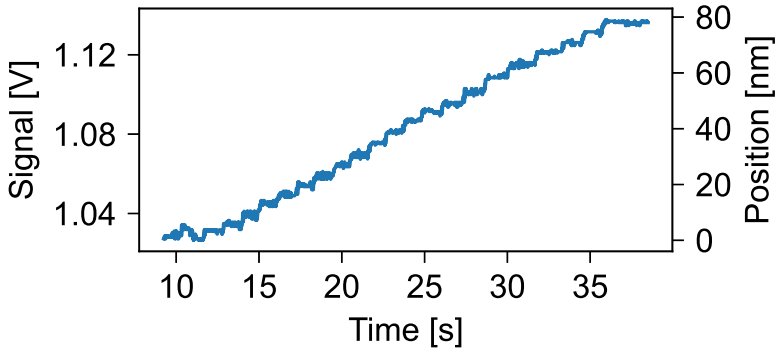

Figure 4.19: Optical measurement of the positioner response as we ask for 5 nm displacements in open-loop mode.

The variation of the voltage signal ΔV was converted to displacement Δd by relying on the basic working principles of an optical interferometer. We assume that we remain in a quasi-linear regime for the voltage fluctuation which allows to express the displacement as a function of the voltage in the form of Eq. 4.37 [134].

$$\Delta d = \frac{\lambda \Delta V}{2\pi \left(V_{\max} - V_{\min}\right)} \tag{4.37}$$

Here, $V_{\max}$ and $V_{\min}$ correspond to the maximum (constructive interference) and minimum (destructive interference) voltage value of the interference signal and $\lambda = 1563.52$ nm corresponds to the wavelength of our laser (RIO ORION$^{\text{TM}}$). Since the amplitude of these fluctuations is much smaller than the uncertainty resulting from the material constants, we consider their impact to be negligible and do not include this value in our uncertainty analysis.

4.2.4.5 Uncertainty Analysis

Due to the high resolution of our radiation sensor and positioning system, the accuracy of our minimum distance results is limited mostly by the uncertainty on material constants of SiN, which are not reported with more than two significant figures [9, 169–171, 173]. To compute the uncertainty on the frequency shift we assume the errors are uncorrelated and propagate the uncertainty as

$$\delta_f = \sqrt{\left(\frac{\partial f}{\partial \alpha}\delta_\alpha\right)^2 + \left(\frac{\partial f}{\partial \nu}\delta_\nu\right)^2 + \left(\frac{\partial f}{\partial E}\delta_E\right)^2 + \left(\frac{\partial f}{\partial \rho}\delta_\rho\right)^2}, \tag{4.38}$$

where δ_i denotes the uncertainty on the value i, f is the resonance frequency of the SiN membrane, $\alpha = 2.2 \pm 0.1 \times 10^{-6}$ K^{-1} is the coefficient of thermal expansion of SiN, $\nu = 0.27 \pm 0.03$ is the Poisson ratio of SiN, $E = 300 \pm 30$ GPa is the Young modulus of SiN, and $\rho = 3100 \pm 100$ kg/m^3 is the density of SiN. Using the formalism described in Ref. 66 one can approximate the thermally induced resonance frequency shift Δf as

$$\Delta f \approx -\frac{\alpha E f_0}{2\sigma_0 \left(1 - \nu\right)} \Delta \overline{T_{\text{m}}}, \tag{4.39}$$

where $f_0 \approx 58.5$ kHz is the membrane resonance frequency at room temperature, σ_0 is the built-in stress at room temperature, and $\overline{T_{\text{m}}}$ denotes the temperature average over

the membrane area, such that $\Delta\overline{T_{\mathrm{m}}} = \overline{T_{\mathrm{m}}} - T_{\infty}$. The built-in stress at room temperature σ_0 can be computed from the membrane resonance frequency at room temperature f_0, the density ρ, the side length of the resonator L, and the vibrational mode shape (n, j).

$$\sigma_0 = \frac{4 f_0^2 \rho L^2}{(n^2 + j^2)} \tag{4.40}$$

Therefore, combining Eq. 4.39 and Eq. 4.40 allows to express the frequency shift as a function of only the material constants and the membrane temperature for the vibrational mode shape $(1, 1)$,

$$\Delta f \approx -\frac{\alpha E}{4 f_0 \rho L^2 (1-\nu)} \Delta\overline{T_{\mathrm{m}}}. \tag{4.41}$$

Using Eq. 4.41 we can compute the partial derivative of the frequency shift with respect to each material constant,

$$\frac{\partial f}{\partial \alpha} = -\frac{E}{4 f_0 \rho L^2 (1-\nu)} \Delta\overline{T_{\mathrm{m}}}, \tag{4.42}$$

$$\frac{\partial f}{\partial \nu} = -\frac{\alpha E}{4 f_0 \rho L^2 (1-\nu)^2} \Delta\overline{T_{\mathrm{m}}}, \tag{4.43}$$

$$\frac{\partial f}{\partial E} = -\frac{\alpha}{4 f_0 \rho L^2 (1-\nu)} \Delta\overline{T_{\mathrm{m}}}, \tag{4.44}$$

$$\frac{\partial f}{\partial \rho} = \frac{\alpha E}{4 f_0 \rho^2 L^2 (1-\nu)} \Delta\overline{T_{\mathrm{m}}}. \tag{4.45}$$

By plugging Eq. 4.42-4.45 into Eq. 4.38 we find

$$\delta_f = \left| -\frac{\alpha E}{4 f_0 \rho L^2 (1-\nu)} \Delta\overline{T_{\mathrm{m}}} \right| \sqrt{\left(\frac{\delta_\alpha}{\alpha}\right)^2 + \left(\frac{\delta_\nu}{1-\nu}\right)^2 + \left(\frac{\delta_E}{E}\right)^2 + \left(-\frac{\delta_\rho}{\rho}\right)^2}. \tag{4.46}$$

Eq. 4.46 can therefore be simplified to

$$\delta_f = |\Delta f| \sqrt{\left(\frac{\delta_\alpha}{\alpha}\right)^2 + \left(\frac{\delta_\nu}{1-\nu}\right)^2 + \left(\frac{\delta_E}{E}\right)^2 + \left(-\frac{\delta_\rho}{\rho}\right)^2}. \tag{4.47}$$

Using Eq. 4.47 we can compute the uncertainty on the frequency shift as

$$\delta_f = |\Delta f| \sqrt{\left(\frac{0.1 \times 10^{-6}\ \mathrm{K}^{-1}}{2.2 \times 10^{-6}\ \mathrm{K}^{-1}}\right)^2 + \left(\frac{0.03}{1-0.27}\right)^2 + \left(\frac{30\ \mathrm{GPa}}{300\ \mathrm{GPa}}\right)^2 + \left(-\frac{100\ \mathrm{kg/m^3}}{3100\ \mathrm{kg/m^3}}\right)^2}$$

$$\delta_f = 0.1216\,|\Delta f|\,.$$

Due to near-field radiation, the frequency shift Δf varies with the separation between the two surfaces d. Unfortunately, no simple analytical function can describe the behavior of the frequency shift Δf as a function of the distance d. Therefore, to obtain the uncertainty on the minimal separation, we compute the trend numerically and perform a curve fit for each temperature difference (see Fig. 4.20). Since we are fitting the theoretical model along the frequency shift (vertical) axis to account for uncertainty of far-field radiation intensity from the glass radiator and heater, only the uncertainty on the near-field frequency shift is relevant. Therefore, in Fig. 4.20, we fit a relation for the frequency shift due to the near-field radiation signal Δf_{NF}. We fit the curves in Fig. 4.20 to a simple empirical model that agrees well with the data and allows partial derivatives to be calculated explicitly. Note that the equations shown in Fig. 4.20 are used to compute the distance d in µm.

We can use the functions obtained from the curve fit, shown in Fig. 4.20, to compute the partial derivative that can later be used for the uncertainty calculation. For example, here is how we derive the uncertainty formula for the case of the 4.1 K temperature difference.

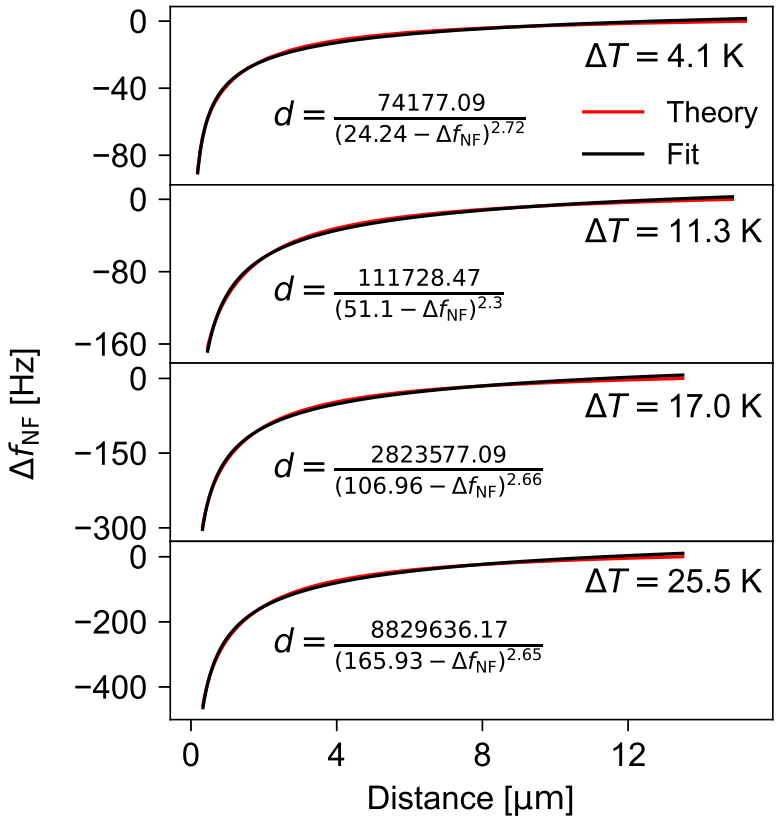

Figure 4.20: Curve fit of the separation as a function of the thermally induced frequency shift for each temperature difference.

$$d = \frac{74177.09}{(24.24 - \Delta f_{\mathrm{NF}})^{2.72}}$$

$$\frac{\partial d}{\partial f} = \frac{201761.68}{(24.24 - \Delta f_{\mathrm{NF}})^{3.72}}$$

$$\delta_d = \left|\frac{\partial d}{\partial f}\delta_f\right| = \left|\frac{201761.68}{(24.24 - \Delta f_{\mathrm{NF}})^{3.72}} 0.1216\,|\Delta f_{\mathrm{NF}}|\right|$$

$$\delta_d = \left|\frac{0.3309 d}{24.24/\Delta f_{\mathrm{NF}} - 1}\right| \tag{4.48}$$

For the uncertainty on the surface polariton (SP) mode contribution, we also had to perform a curve fit since no simple analytical function allows to express the SP mode

contribution as a function of the distance d. The curve fit can be seen in Fig. 4.21. Note that once again, here, the relation is given for the distance in µm.

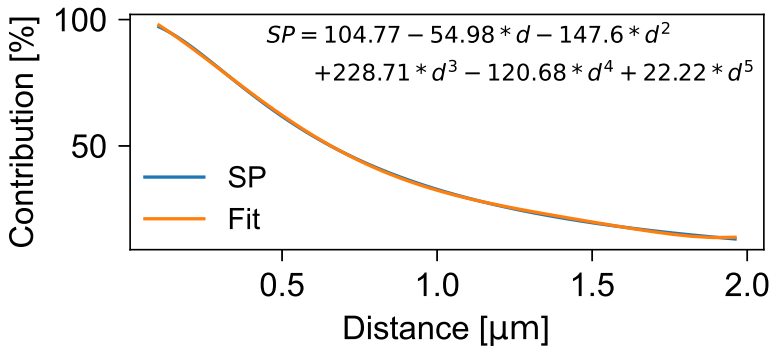

Figure 4.21: Curve fit of the SP mode contribution as a function of the separation.

Once again, we can use the function obtained from the curve fit to calculate the uncertainty of the SP contribution.

$$\frac{\partial SP}{\partial d} = -54.98 - 295.2d + 686.13d^2 - 482.72d^3 + 111.11d^4$$

$$\delta_{SP} = \left| \frac{\partial SP}{\partial d} \delta_d \right|$$

$$\delta_{SP} = \left| \left(-54.98 - 295.2d + 686.13d^2 - 482.72d^3 + 111.11d^4\right) \frac{0.3309d}{24.24/\Delta f_{\mathrm{NF}} - 1} \right|$$

$$\delta_{SP} = \left| \frac{-18.19d - 97.68d^2 + 227.04d^3 - 159.73d^4 + 36.77d^5}{(24.24/\Delta f_{\mathrm{NF}} - 1)} \right| \tag{4.49}$$

Therefore, using Eq. 4.48 and Eq. 4.49, we can compute an uncertainty of ±50 nm on the minimal distance and an uncertainty of ±4% on the SP contribution for the case of the 4.1 K temperature difference. Using the same formalism as described above, we can compute the uncertainty on the minimal distance at all temperature differences. The results are shown in Table 4.1.

Table 4.1: Uncertainty on the minimal separation for each temperature differences

ΔT [K]	δ_d [nm]
4.1	50
11.3	100
17.0	70
25.5	80

4.2.4.6 Relative Contributions of Propagating, Frustrated, and Surface Modes to Total Heat Transfer

In this section, we discuss the contribution of each component of the heat flux occurring over the full resonator area (rather than only at the radiator tip in the main text). Fig. 4.22a shows the contribution of each of the components of the heat flux as a function of the separation for the case of a 4.1 K temperature difference. At the minimal separation of 180 nm, the surface polariton (SP) and frustrated modes have contributions of 10.6% and 7.9%, respectively, while the propagating mode is dominant with a contribution of 81.5%. These proportions vary strongly with the membrane dimension. Fig. 4.22b shows that if we changed our membrane side length to 0.25 mm the SP contribution would be much more important. More precisely, 68.4% of the heat transfer would be caused by SP at a 180 nm separation.

Using a smaller membrane would also increase the enhancement due to near-field radiation compared to far-field radiation. Fig. 4.23 shows that for a membrane with a 0.25 mm side length there would be a 9-fold enhancement of the heat transfer, at the minimal separation of 180 nm.

To further visualize the enhancement of the radiative heat flux due to near-field radiation, in Fig. 4.24, we show the heat flux of each of the heat transfer modes normalized to the far-field intensity for a membrane side length of 0.25 mm. Note that the far-field intensity is 13 times smaller than the blackbody limit due to the low emissivity of SiN. In contrast, the heat flux, at the radiator apex, exceeds the blackbody limit by a factor of 3, at the minimal separation of 180 nm.

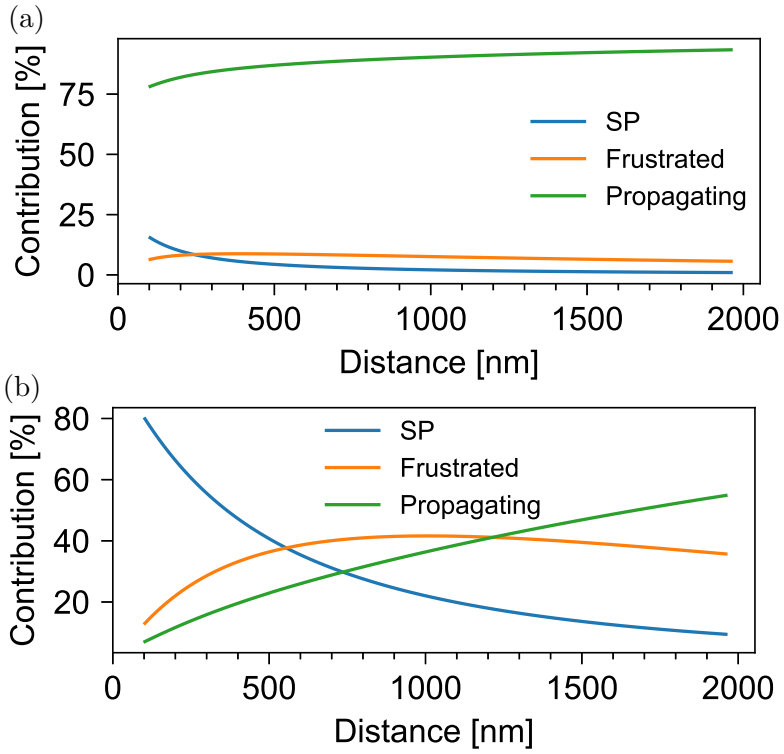

Figure 4.22: Contribution of each of the components of the radiative heat flux over the full area of the resonator as a function of distance for a 4.1 K temperature difference for (a) the case of our membrane (1.7 mm in side length) and (b) the case of a membrane with a 0.25 mm side length.

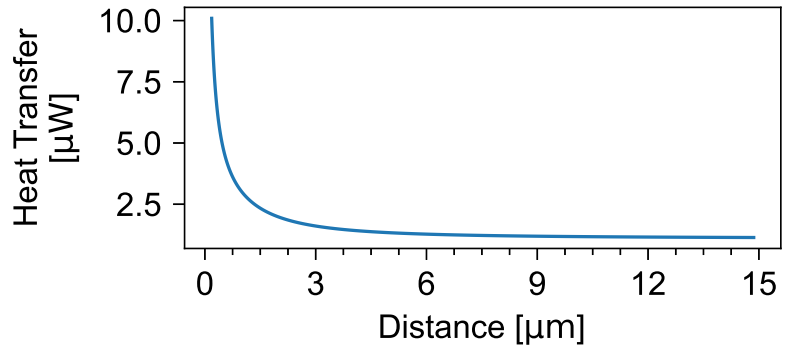

Figure 4.23: Radiative heat transfer as a function of separation for a membrane side length of 0.25 mm showing a 9-fold enhancement of the heat transfer as we transition from the far-field to the near-field regime.

4.2.4.7 Hybridization of Surface Polariton Resonances in Thin Film SiN

In this section, we discuss the potential hybridization of surface polariton (SP) resonances. In Fig. 4.25, we can observe the spectral radiative heat transfer at a 180 nm

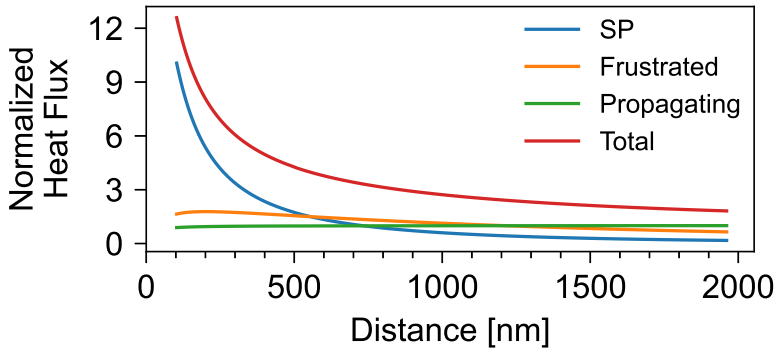

Figure 4.24: Far-field normalized heat flux of each of the heat transfer modes over the full area of the resonator as a function of distance for a 4.1 K temperature difference for the case of a membrane with a 0.25 mm side length.

separation for different membrane thickness. The comparison demonstrates that the use of a thin layer, such as our 100 nm thick membrane, enhances slightly the amplitude of the SP resonance which could be due to the hybridization of the top and bottom interface modes. However, a thin membrane leads to an overall weaker heat transfer compared to bulk SiN, due mostly to attenuation of propagating and frustrated radiative coupling.

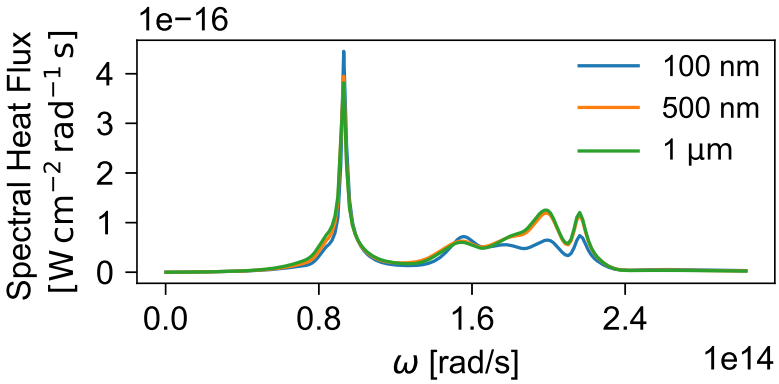

Figure 4.25: Spectral radiative heat transfer at a 180 nm separation for different membrane thickness. The data demonstrates an enhancement of the SP resonance due to hybridization in thin layers.

4.2.4.8 Radiative Heat Transfer Transmission Coefficients

In this section, we discuss the transmission coefficient describing the coupling of the two surfaces in the near-field regime at the radiator apex. In Fig. 4.26a and Fig. 4.26b, we can observe the transmission coefficient as a function of the unit angular frequency, ω, and

parallel wavevector, k_ρ, at 180 nm separation for transverse magnetic (TM) and transverse electric (TE) polarization, respectively. A surface polariton (SP) resonance ($k_\rho > \min(\mathrm{Re}(n_{\mathrm{SiO_2}})k_\mathrm{v}, \mathrm{Re}(n_{\mathrm{SiN}})k_\mathrm{v})$) is clearly visible in Fig. 4.26a at $\omega = 9.24 \times 10^{13}$ rad/s.

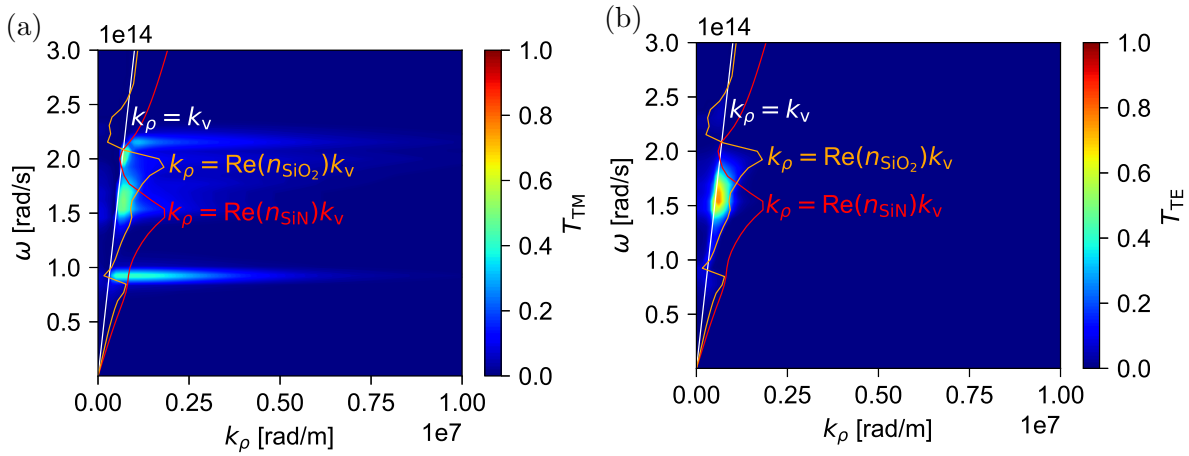

Figure 4.26: Calculated transmission coefficients, at the radiator apex, per unit angular frequency, ω, and parallel wavevector, k_ρ, at 180 nm separation for (a) transverse magnetic (TM) and (b) transverse electric (TE) polarization.

4.2.4.9 Spectral Distribution of Radiative Heat Transfer

Fig. 4.27 shows the spectral radiative heat flux, at radiator apex, for the minimal distance reached in all scans discussed in the manuscript.

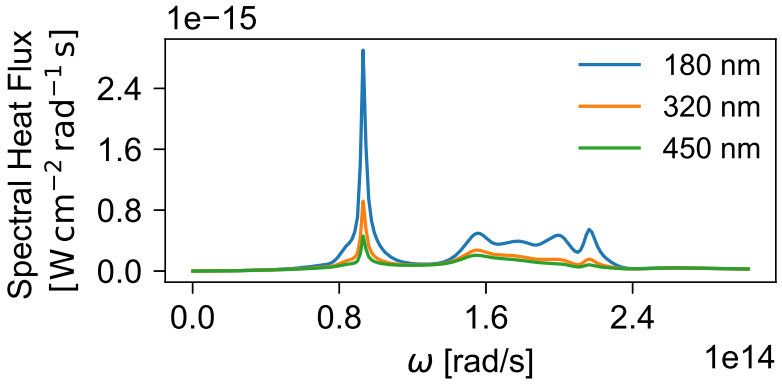

Figure 4.27: Spectral radiative heat transfer at the minimal separation reached in all scans discussed in the manuscript.

5. Experimental Platform for Near-Field Thermophotovoltaics

This chapter discusses the technical challenges encountered during attempts to perform NFTPV measurements using custom InAs PV cells (i.e., Objective 3). This work is part of a multidisciplinary initiative between uOttawa, Princeton, and Polytechnique Montréal aimed at achieving high efficiency NFTPV energy conversion. During the first phase of this partnership, PV cell experts (Prof. Karin Hinzer group, uOttawa, and Prof. Zbig Wasilewski group, University of Waterloo) have fabricated custom PV cells optimized for near-field thermal radiation [78]. Our role in this collaboration is to achieve the experimental demonstration of NFTPV energy conversion using these specialized cells; however, as detailed in this chapter, certain technical challenges prevented the successful execution of these measurements. In Section 5.1, we first discuss the development of the NFTPV platform, followed by an overview of the far-field and near-field measurements and the associated technical challenges in Section 5.2. Finally, in Section 5.3, we propose a revised platform.

5.1 Development of the Experimental Platform

During the first phase of this work, we redesigned the platform described in our previous work [150] (i.e., Platform 2 in Chapter 3) to incorporate PV cells. The new platform (see Fig. 5.1), referred to as Platform 3 in Chapter 3, supports the integration of PCBs on which the PV cells are mounted. An additional rotation stage (Thorlabs PDR1V) is included to enable the alignment of the front contact electrodes with the radiator chip. Preliminary testing revealed that the high temperature of the radiator

chip (i.e., $\sim 700\,\mathrm{K}$, much higher than in our previous work [150]) caused parasitic heating of the positioners, exceeding the threshold value. To mitigate this issue, we redesigned the platform to support the radiator chip with glass rods, thereby reducing conduction between the radiator chip and the positioners. Additionally, aluminum sheets, acting as heat shields, are placed in front of the positioners to minimize parasitic heating.

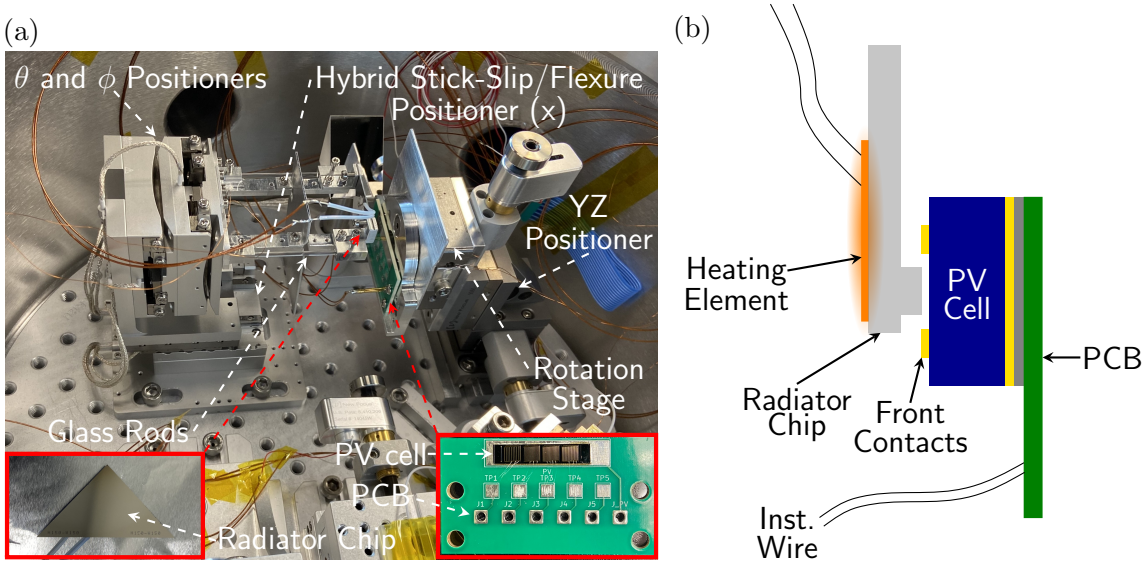

Figure 5.1: (a) Photograph of the experimental platform adapted for NFTPV. A metal ceramic heater is mounted to the back of the Si radiator chip, as shown in the bottom-left inset. The InAs PV cell is mounted to a PCB with silver epoxy, as shown in the bottom-right inset. (b) Illustration of the experimental platform adapted for NFTPV, showing how the radiator tip is positioned between the front contacts of the PV cell.

Due to alignment requirements, the platform cannot accommodate probes, therefore, the PV cell must be packaged on a PCB (see bottom-right inset of Fig. 5.1a). This poses additional challenges, as it requires the development of dicing, mounting, and wire bonding procedures. The devices were sent to the Interdisciplinary Institute for Technological Innovation (3IT) in Sherbrooke for dicing into a suitable form factor using a two-step dicing process to avoid short-circuiting at the edges. A precut is first performed with a $100\,\mu\mathrm{m}$ wide blade to a depth of $\sim 50\,\mu\mathrm{m}$, followed by a full cut with a $40\,\mu\mathrm{m}$ wide blade, aligned at the center of the precut trench, dicing the sample through its entire thickness (i.e., $500\,\mu\mathrm{m}$). For the mounting procedure, various bonding agents are tested;

however, due to the low damage threshold temperature of InAs PV cells, the use of high curing temperature bonding agents is precluded. While InAs substrates can withstand temperatures exceeding 700 K [177], the thin layers and junctions in InAs-based PV cells increase susceptibility to thermal degradation, resulting in a much lower damage threshold temperature [178, 179]. For each test, a dark current-voltage (IV) curve is performed on the sample using a probe station prior to mounting. Another dark IV curve is then performed after mounting and wire bonding to assess the impact of the packaging procedure on the device's performance. We initially attempt to mount GaAs PV cells, provided by Myles Steiner and Eric Tervo's team at NREL, using solder paste (Chip Quik® SMD291AX10 Solder Paste). The results appear quite promising (see Fig. 5.2a), as the mounting procedure has no noticeable effect on the performance of the cell. We believe that the discrepancy between the pre- and post-packaging curves in Fig. 5.2a is solely due to parasitic resistance introduced by the probes used for the pre-packaging dark-IV measurements. However, the high melting temperature (i.e., 183 °C) of the solder paste renders it unsuitable for InAs PV cells. We explore silver paste (PELCO® High Performance Silver Paste) as a potential alternative, given its low curing temperature (i.e., 93 °C). Unfortunately, we conclude that the bond formed is not sufficiently sturdy to endure the pressure exerted during wire bonding. Finally, we investigate silver epoxy (M.G. Chemicals Silver Conductive Epoxy Adhesive), which has an even lower curing temperature (i.e., 65 °C). The resulting bond proves to be robust enough to withstand the pressure applied during wire bonding. Most importantly, the performance of the cell does not appear to be significantly affected by the packaging procedure (see Fig. 5.2b).

To complement our experimental platform, we design and fabricate specialized p-doped Si chips intended to function as radiators for NFTPV measurements. Note that, while we now employ custom devices for the radiator, this platform remains flexible as it enables the implementation of cells of various materials and geometries. Although the radiator chip must be designed to fit between the front contacts of the cell, chips of

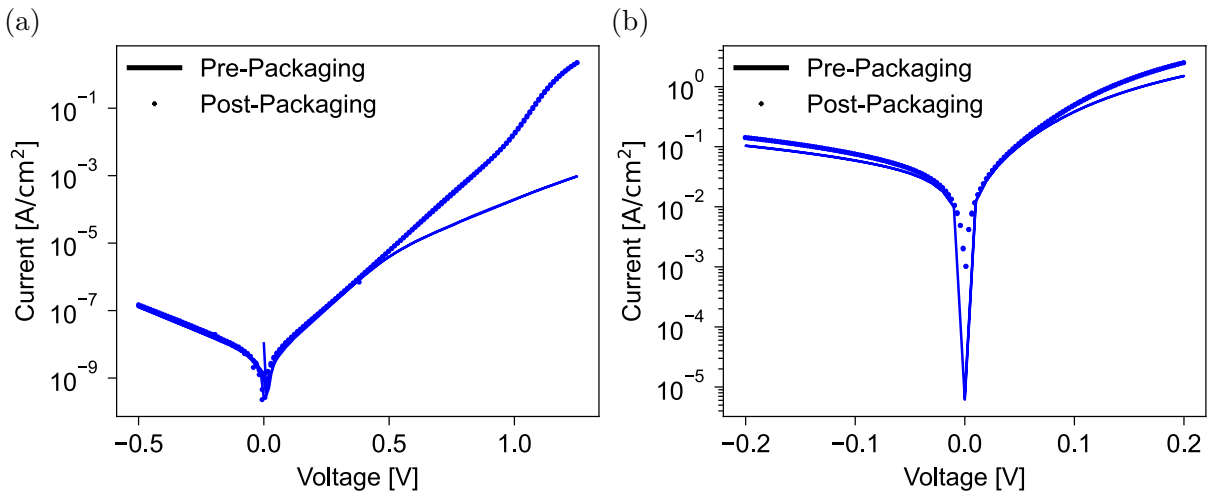

Figure 5.2: Pre- and post-packaging dark IV curves for (a) a GaAs PV cell mounted with solder paste and (b) an InAs PV cell mounted with silver epoxy.

different dimensions can easily be fabricated and exchanged to test various cells. The radiator chip is heated by a metal ceramic heater attached to its back side using silver paste (PELCO® High Performance Silver Paste), as illustrated in Fig. 5.1b. This Si radiator consists of a triangular chip, where most of the substrate is etched (i.e., to a depth of $\sim 5\,\mu m$) via RIE, except for a small area of a few hundred microns (see Fig. 5.3). The etched area is coated with platinum to lower its emissivity. The unetched area serves as the radiator, while the metal coating on the etched area significantly reduces radiative heat flux from that region. The unetched radiator region will be strategically aligned with the front contact electrodes of the PV cell and positioned to operate within the

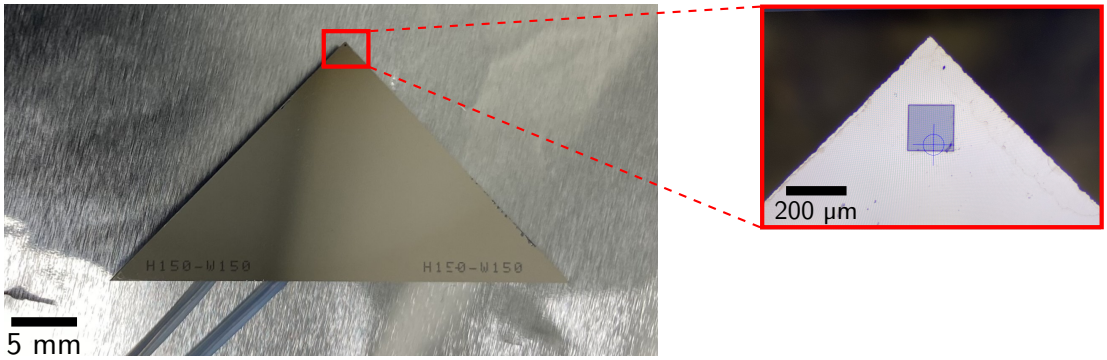

Figure 5.3: Photograph of the p-doped Si radiator chip with a close-up of the radiator tip.

near-field of the cell, as shown in Fig. 5.1b. The complete fabrication process is outlined in Fig. 5.4.

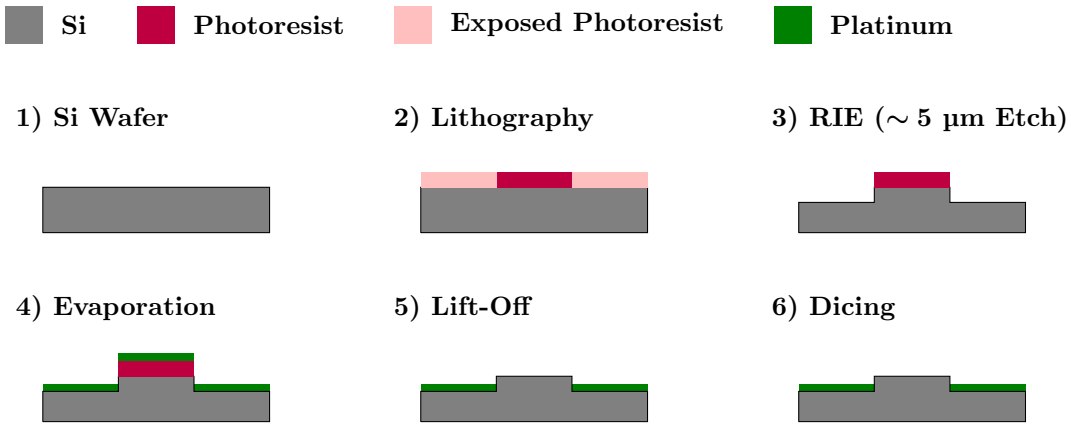

Figure 5.4: Illustration of the fabrication process for the p-doped Si radiator chip tailored for NFTPV measurements.

5.2 Measurements and Testing

We perform far-field TPV measurements using the experimental platform described in Section 5.1 to assess its performance. During these scans, we increase the temperature of the metal ceramic heater from room temperature to approximately 700 K—resulting in a radiator tip temperature of approximately 625 K, assuming negligible thermal contact resistance—and measure the power generated by the PV cell at each temperature. As shown in Fig. 5.5, power generation occurs once the heater temperature reaches approximately 500 K. These measurements are carried out with InAs PV cells provided by Myles Steiner and Eric Tervo's team at NREL.

To perform NFTPV measurements, the radiator must be precisely aligned between the two front contacts of the PV cell. In a first attempt to perform such alignment, we adjust the transverse position of the PV cell while maintaining the radiator tip stationary at 550 K in the far-field, as illustrated in Fig. 5.6a. We anticipated that positioning the radiator in front of a front contact would cause shadowing, leading to a reduction in the measured photocurrent. However, no such shadowing effect is observed in Fig. 5.6b,

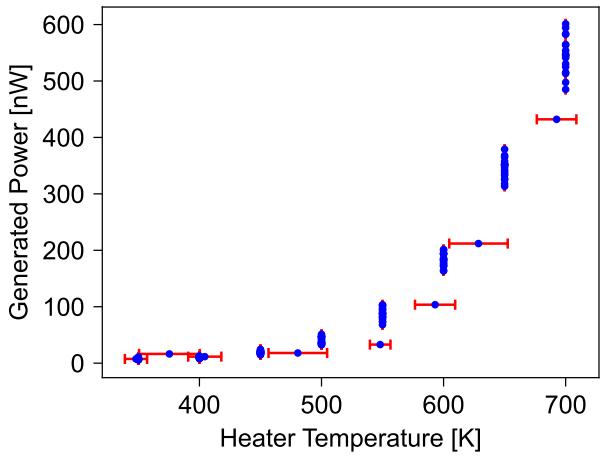

Figure 5.5: Far-field TPV measurement showing the output power of an InAs PV cell as a function of the temperature of the metal ceramic heater.

in which we perform 14,000 transverse motion steps of $\sim 25\,\text{nm}$. Given the spacing of $150\,\mu\text{m}$ between the front contacts of the PV cell, at least two photocurrent drops due to shadowing were expected. Unfortunately, these drops in photocurrent, anticipated to occur at approximately every 6,000 steps, are not visible in Fig. 5.6b. We suspect that the shadowing effect may be negligible due to the very narrow width of the front contacts ($5\,\mu\text{m}$). Additionally, it is possible that parasitic far-field radiation emitted from the platinum-coated substrate is masking the effect of the radiator tip alignment. The variation in photocurrent observed in Fig. 5.6b is likely attributable to drift or changes in the view factor as the transverse position of the PV cell is adjusted.

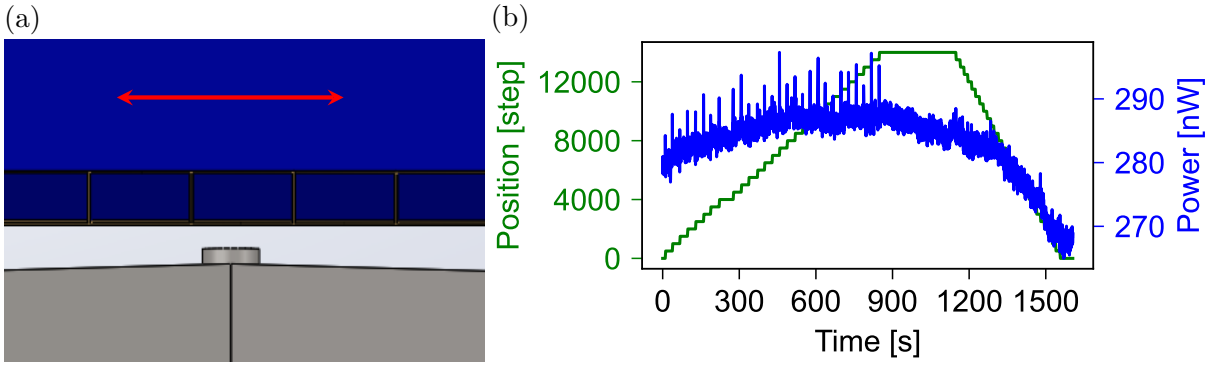

Figure 5.6: (a) Render of the far-field alignment of the PV cell with the Si radiator tip. (b) Measured generated power from the PV cell in the far-field as a function of transverse position as the Si radiator is being heated at 550 K.

Since aligning the radiator tip in the far-field regime was unsuccessful, we attempt alignment in the near-field regime. We heat the radiator to 550 K and conduct near-field scans, adjusting the transverse position between each scan to find the location where the power increase due to near-field radiation is maximal. During each scan, we measure the generated power at a specific voltage while approaching the radiator until a sharp drop in power is observed. We assume that this sharp drop is due to heating of the PV cell, therefore, indicating contact between the radiator and the PV cell. Surprisingly, we do not observe any power increase due to near-field radiation. As shown in Fig. 5.7a, as the radiator tip is approached, only a reduction in generated power is observed. This reduction suggests that we are not measuring near-field radiation but rather experiencing a preliminary contact with the front contact, exponentially decreasing the generated power until the radiator makes contact with the PV cell substrate. However, this power decrease could also be caused by subgap near-field radiation. In Fig. 5.8, we demonstrate, using a one-dimensional fluctuational electrodynamics model from Ref. 98, that as the radiator tip transitions into the near-field regime, an increase in above-bandgap radiation occurs as expected, yet a much more significant increase in subgap radiation is noticeable.

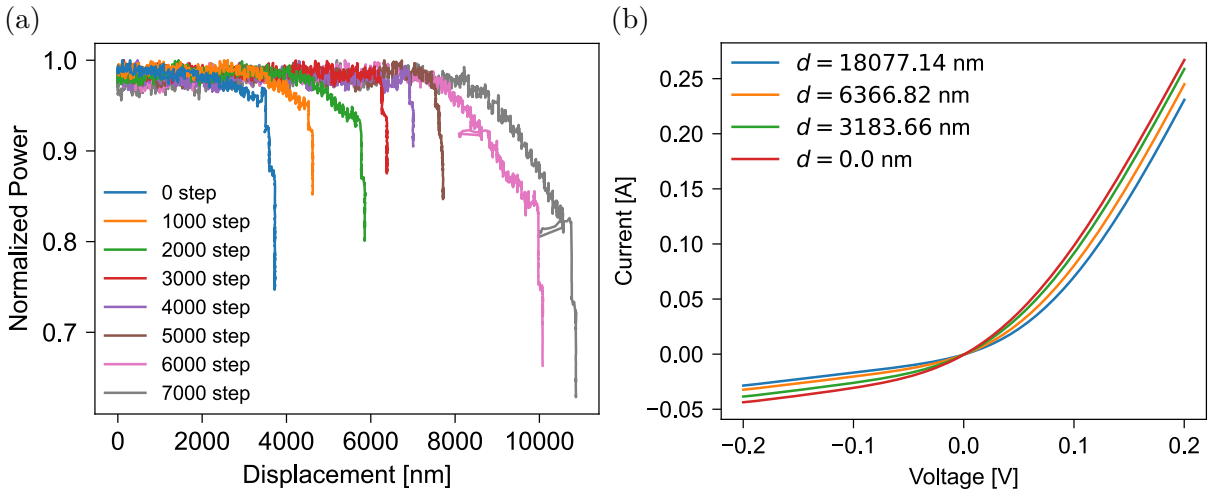

Figure 5.7: (a) Measured normalized generated power from the PV cell as we bring the radiator in the near-field regime for different transverse positions. (b) IV curve of the PV cell for different distances from the radiator.

This subgap radiation heats the PV cell, thus altering its performance and, therefore, could explain the observed decrease in photocurrent.

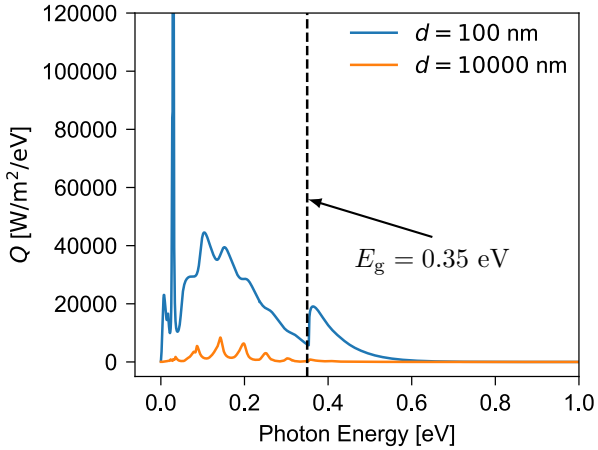

Figure 5.8: Simulated spectral radiative heat flux absorbed in the InAs PV cell for a distance of 10 µm and 100 nm.

Despite this limitation, Fig. 5.7a shows that the power decrease varies with the transverse position of the PV cell, suggesting that alignment could still be achieved using this procedure. Nevertheless, it is crucial to confirm that the observed effect is due to near-field radiative heat transfer. To validate this hypothesis, we assess the performance of the PV cell through IV measurements in the far-field, at various locations in the near-field, and following a "contact" event (i.e., sharp drop in power). As shown in Fig. 5.7b, as we approach the radiator tip, the IV curve shifts lower in reverse bias but higher in forward bias, indicating performance degradation. We conduct measurements at higher temperatures (i.e., 700 K) with the aim of enhancing the above-bandgap radiation sufficiently to observe power generation from near-field radiation. Unfortunately, we find that the large thermal mass of the radiator at higher temperatures causes significant damage to the device upon contact, precluding further high-temperature scans. Consequently, we are unable to definitively determine whether we observe a preliminary contact event or measure subgap near-field radiation. Additionally, non-localized heating makes it impossible to distinguish between contact with the radiator tip and the radiator substrate, further complicating the alignment process.

5.3 Proposed Revised Platform

We propose a major redesign of our experimental platform to facilitate the alignment of the radiator with the PV cell. In our current platform (i.e., Platform 3 in Chapter 3), we attempt to rely on the variation of the near-field radiative signal to align the two surfaces. While this method has been successful in the past [77], it required a localized heating element, contact detection through a laser deflection scheme, cryogenic cooling of the PV cell, and pre-alignment with an optical microscope—all of which are not feasible with our current platform. To address these limitations, we suggest replacing our radiator chip with a graphite sphere glued onto a SThM probe (BRUKER® VITA-HE-NANOTA-200) using a ceramic adhesive (RESBOND^{TM} 989F) that can withstand temperatures up to 1920 K, as illustrated in Fig. 5.9. This probe-sphere platform has been successfully implemented in Ref. 53. The micrometer-sized heating element will enable higher temperature measurements and significantly simplify the alignment process. Similar to Platforms 1 and 2, contact detection is enabled by a fiber interferometer measuring the vibrational response of the mechanically excited probe. We also plan on integrating a thermoelectric cooler to maintain the PV cell at a constant temperature, thereby minimizing the effect of parasitic subgap radiation. Recent works [58, 59, 78] have shown that such cooling is crucial for NFTPV measurements. Finally, the graphite spherical surface will eliminate the need for angular alignment. Additionally, at small distances ($\lesssim 50\,\text{nm}$), transitioning from a Si radiator to a graphite radiator will enhance the above-bandgap radiation and reduce the parasitic subgap radiation [53]. This proposed platform is referred to as Platform 4 in Chapter 3.

The use of graphite for the radiator seems contradictory to the findings in Chapter 6, in which we demonstrate that InAs is a promising radiator material. While graphite is predicted to deliver excellent performance in the sub-100 nm regime, its advantages over doped Si only emerge at distances smaller than 70 nm [53]. In contrast, in Chapter 6,

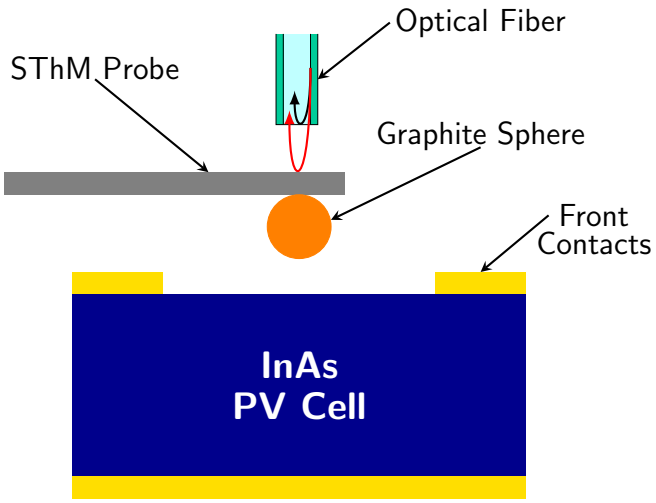

Figure 5.9: Illustration of the suggested NFTPV platform using a SThM probe onto which a graphite microsphere is mounted. This platform is similar to the one observed in Ref. 53.

we demonstrate that InAs outperforms doped Si even at larger distances, such as those typically observed in static devices (i.e., $> 100\,\text{nm}$ [180]), which we anticipate to be the form factor of commercially deployed products. In the case of static devices, InAs would also be advantageous for monolithic fabrication in a single crystal growth process for both the radiator and the PV cell. A sacrificial layer between the radiator and PV cell could be selectively etched to achieve a precise gap between the two surfaces, simplifying fabrication. Nevertheless, in this case, we opt for graphite microspheres due to their commercial availability [181] and relative simplicity of fabrication.

Despite the complex design of the radiator and the restrictions imposed on its material, this new platform can still be regarded as a flexible platform, as it enables the testing of many new interesting PV materials. In fact, the spherical geometry of the heating element will facilitate the integration of PV cells of various geometries. Additionally, although we will be limited to materials that can be shaped into microspheres, using a spherical radiator will simplify the alignment procedure, enabling the rapid testing of various PV samples.

6. New Radiator Materials for Near-Field Thermophotovoltaics

This chapter discusses the theoretical investigation of new radiator materials aimed at improving the performance of NFTPV systems (i.e., Objective 4). In Section 6.1, we present our theoretical NFTPV article [182], which focuses on achieving Objective 4.

6.1 Radiator Tailoring for Enhanced Performance in InAs-Based Near-Field Thermophotovoltaics

This section is a reproduction of our theoretical NFTPV article [182], published in *Solar Energy Materials and Solar Cells* in 2025, which focuses on the theoretical investigation of new radiator materials that could improve the performance of InAs-based NFTPV systems. Additionally, this work investigates the overestimation of free carrier absorption in the dielectric model of InAs.

6.1.1 Impact

This manuscript presents the following novelties:

1. Designed a NFTPV radiator that results in a nearly threefold enhancement of spectral efficiency compared to a doped Si radiator.

2. Proposed a revised model to correct the overestimation of free carrier absorption in the dielectric model of InAs.

6.1.2 Author Contribution

Mathieu Giroux: As the lead graduate student associated with this project, I developed part of the numerical model and performed simulations. Additionally, I was the lead author of this article.

Sean Molesky: As a professor at Polytechnique Montréal, Dr. Molesky implemented the fluctuational electrodynamics model used in this work and provided detailed feedback during the analysis of the simulation results.

Raphael St-Gelais: As a professor at the University of Ottawa, Dr. St-Gelais provided detailed feedback and helped with the conceptualization of the project.

Jacob J. Krich: As the principal investigator of the project and a professor at the University of Ottawa, Dr. Krich led the conceptualization of the project, guided my research, provided detailed feedback throughout this project, and assisted in editing the manuscript.

6.1.3 Article Content

Radiator Tailoring for Enhanced Performance in InAs-Based Near-Field Thermophotovoltaics

Mathieu Giroux[a], Sean Molesky[b], Raphael St-Gelais[a,c,d], and Jacob J. Krich[c,d]

[a]Department of Mechanical Engineering, University of Ottawa, Ottawa K1N 6N5, Ontario, Canada
[b]Department of Engineering Physics, Polytechnique Montreal, Montreal H3T 1J4, Quebec, Canada
[c]Department of Physics, University of Ottawa, Ottawa K1N 6N5, Ontario, Canada
[d]Nexus for Quantum Technologies, University of Ottawa, Ottawa K1N 6N5, Ontario, Canada

Abstract

Near-field thermophotovoltaics (NFTPV) systems have significant potential for waste heat recovery applications, with both high theoretical efficiency and power density, up to 40% and 11 W/cm^2 at 900 K. Yet experimental demonstrations have only achieved up to 14% efficiency and modest power densities (i.e., 0.75 W/cm^2). While experiments have recently started to focus on photovoltaic (PV) cells custom-made for NFTPV, many studies still rely on doped silicon radiators. In this work, we design an optimized NFTPV radiator for an indium arsenide-based system and, in the process, investigate models for the permittivity of InAs in the context of NFTPV. Based on existing measurements of InAs absorption, we find that the traditional Drude model overestimates free carrier absorption in InAs. We replace the Drude portion of the InAs dielectric function with a revised model derived from ionized impurity scattering. Using this revised model, we maximize the spectral efficiency and power density of a NFTPV system by optimizing the spectral coupling between a radiator and an InAs PV cell. We find that when the radiator and the PV cell are both made of InAs, a nearly threefold improvement of spectral efficiency is possible compared to a silicon radiator with the same InAs cell. This enhancement reduces subgap thermal transfer while maintaining power output.

6.1.3.1 Introduction

Waste heat above 600 K represents 10% of the global energy consumption [28]. Harvesting this energy would significantly enhance energy-use efficiency and reduce carbon emissions. For 600-900 K heat sources, thermoelectric generators (TEGs) are the most-widely used solid-state technology [183]. While TEGs have experimentally achieved high power densities up to 22 W/cm^2 at 868 K [30], conduction losses limit achievable efficiencies [31], which are typically less than 10% [183]. Thermophotovoltaic (TPV) systems present an alternative, potentially efficient, solid-state solution, with theoretical efficiencies up to 45% at 900 K [183], but are limited to low power densities, below 0.2 W/cm^2 at 900 K [183]. Near-field thermophotovoltaics (NFTPV) systems have significant potential for waste heat recovery applications [1–5], with both high theoretical efficiency and power density, up to 40% and 11 W/cm^2 at 900 K [2]. This technology exploits the drastic enhancement of the thermal radiation between two bodies at subwavelength distances due to evanescent radiative thermal coupling. When a cold photovoltaic (PV)

cell is positioned in such close proximity to a hot radiator, tremendous amounts of heat transfer from the hot object to the PV cell, where it can be converted to electricity.

Despite such potential, experimental demonstrations have only achieved up to 14% efficiency and $0.75\,\mathrm{W/cm^2}$ power density [6, 8, 53, 77]. One of the main challenges in the development of NFTPV technology is the need for specialized narrow-bandgap PV cells. Early demonstrations [6, 8] relied on basic PV cells fabricated in house [8] or on commercially available photodetectors [6]. The use of PV cells unoptimized for near-field operations resulted in modest performance, with conversion efficiencies below 1% and less than 1 nW of generated power. Recently, PV cells optimized for NFTPV operation [53, 77] were reported, leading to higher efficiencies and power densities, up to 14% and $0.75\,\mathrm{W/cm^2}$, which are still far from the predicted limits [1–5].

One reason for the gap between high theoretical performances and modest experimental results is that many experimental studies still rely on doped Si radiators [6, 77, 79]. A few theoretical works reported optimized radiator designs for NFTPV applications [4, 5]. These studies relied on plasmonic materials, such as indium-tin-oxide (ITO), which exhibit surface polariton resonances in the infrared region, enhancing the radiative heat flux in a spectral distribution located just above the bandgap of the PV cell. While these materials greatly improve the theoretical performance of NFTPV systems, in practice their optical properties are contingent upon factors such as film annealing and deposition conditions [80], making the experimental implementation of these proposed films quite challenging. Here, with eye towards near-term large-scale implementation, we focus on the more practical and reproducible possibilities offered by crystalline materials.

For the temperature range of waste heat recovery applications (< 1000 K [6]), InAs is a promising material [2, 59, 78], with a bandgap (0.35 eV) well aligned to the Planck spectrum. To predict the properties of InAs in a NFTPV system, an accurate dielectric model is imperative to correctly model the radiative heat transfer spectrum. For this purpose, most dielectric models employ a Drude form for the free-carrier absorption.

We have found that this choice leads to a consistent overestimation of free carrier absorption, both above and below the bandgap, especially for highly doped InAs. Here, we correct this overestimation by substituting the Drude response for a revised model, derived from ionized impurity scattering [123], and, using this refinement, design an optimized radiator for an InAs-based NFTPV system.

We compare the performance of a doped silicon radiator to that of a doped InAs radiator, both paired with an InAs-based photovoltaic cell designed specifically for NFTPV [78]. We find that, when the doping levels and thicknesses of the radiators are chosen optimally, the power output from both radiators is nearly identical, but the spectral efficiency is higher with an InAs radiator. Namely the use of a silicon radiator leads to increased subgap heat transfer, due to an additional subgap resonance. In addition to improving the heat transfer spectrum, reducing such subgap heat transfer lowers cooling requirements and is therefore highly desirable.

6.1.3.2 Results and Discussion

6.1.3.2.1 Dielectric Function

Calculating radiative heat transfer requires knowledge of the dielectric functions of all materials used (in our case Si and InAs) from low energy up to several times the material bandgap. For Si, we use a dielectric model containing lattice and interband contributions from Ref. 125 combined with the Drude free-carrier model from Ref. 109, while incorporating the mobility, decay rates and donor and acceptor contributions from Ref. 124. All of these models have been validated against experimental data in Refs. 109, 125, and 124. For InAs, we employ the comprehensive dielectric model assembled in Ref. 117 with the updated parameters from Ref. 78. This dielectric model includes a Drude-Lorentz model to account for both lattice and free carrier contributions, as well as an interband absorption model with non-parabolicity corrections and the Moss-Burstein shift. Non-parabolicity corrections are employed as both the valence and conduction bands deviate significantly from a simple quadratic relationship at the energies relevant

to this study. The Moss-Burstein shift is included to account for band filling effects, which are significant in InAs due to both its small bandgap and its light effective mass, leading to a shift in the effective bandgap. Note that, unlike Ref. 117, we employ an approximation to the Kramers-Kronig relations to improve computational speed, following the approach of Ref. 78 (see Appendix for full discussion). A Python implementation and a detailed description of these dielectric models can be found in Ref. 184.

Based on existing measurements of InAs absorption [122, 185, 186], we find that the traditional Drude model, proposed for example in Ref. 117, overestimates free carrier absorption in InAs. Fig. 6.1a compares the InAs absorption coefficient from the dielectric model described in Ref. 117 to experimental n-doped InAs absorption data at different donor concentrations N_d taken from Refs. 122, 185, and 186. The comparison suggests that the Drude contribution results in a significant overestimation of free carrier absorption at energies near the bandgap. This discrepancy becomes more noticeable at higher doping levels, leading to an overestimation of absorption above the bandgap. These differences cause inaccurate model predictions of NFTPV performances as above-bandgap absorption originating from free carrier absorption does not generate collectible electron-hole pairs. Additionally, parasitic subgap heating has a considerable effect on the overall performance of the device.

We address this overestimation by incorporating an alternative model, described in Ref. 123, derived from screened ionized impurity scattering. The discrepancies in Fig. 6.1a are most significant at high doping concentration, which is precisely where ionized impurity scattering is strongest. The Drude model is widely used for its simplicity, and it is able to accurately and generically describe the low-frequency dielectric function—and thus free-carrier absorption—in many semiconductors. There are many physically motivated dielectric models that could be used in place of the Drude model, including those considering acoustic phonons and plasmon effects [123]. Models accounting for optical phonons were not considered here, as this effect is already captured by the Lorentz model.

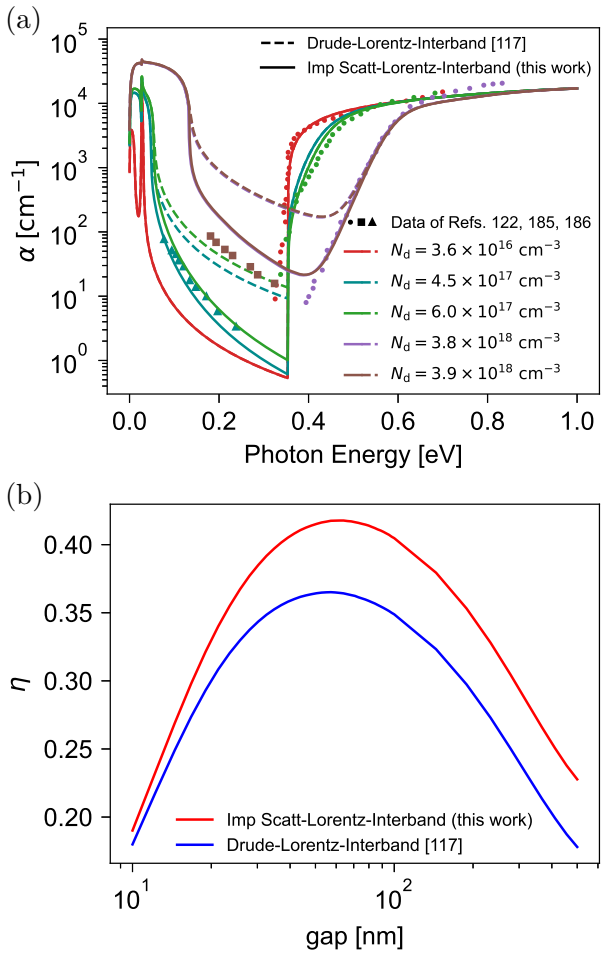

Figure 6.1: (a) InAs absorption coefficient from the dielectric model of Ref. 117 (dashed lines), which combines a Drude-Lorentz model with an interband model (Drude-Lorentz-Interband), compared to data from n-doped InAs (markers). Our revised model, which replaces the Drude model with an ionized impurity scattering model (Imp Scatt-Lorentz-Interband), significantly improves the agreement with experimental data above and below the bandgap, especially at high doping. Circles from Ref. 122, squares from Ref. 185, and triangles from Ref. 186. (b) Computed spectral efficiency, with the Drude-Lorentz-Interband model (blue) and with our proposed model (red), as a function of the gap for an InAs-based NFTPV system using an InAs radiator. The Drude model underestimates the spectral efficiency by up to 22% because it overestimates below-bandgap free carrier absorption.

We select a model based on screened ionized impurity scattering because it provides a physically motivated form that agrees with the Drude model at low frequency but produces an absorption coefficient that decays more rapidly at higher frequency. It is also computationally tractable. While adjusting the loss parameter in the Drude model may appear to be the most straightforward approach to address this issue, we find that reduc-

ing this parameter decreases high-frequency absorption but compromises the accuracy in the low-frequency region. The corrective model is only valid when the Fermi level E_{F} measured from the conduction band minimum is larger than the thermal energy and the frequency ω exceeds the plasma frequency ω_{p}, given by

$$\omega_{\mathrm{p}} = \sqrt{\frac{Ne^2}{\varepsilon_0 \varepsilon_\infty m_{\mathrm{e}}^*}}, \tag{6.1}$$

where N is the carrier density, e is the elementary charge, ε_0 is the vacuum permittivity, ε_∞ is the high-frequency dielectric constant, and m_{e}^* is the electron conduction band effective mass. Therefore, we still employ the Drude model when $\omega < \omega_{\mathrm{p}}$ or when E_{F} is below the thermal energy. For highly n-doped InAs, when $\omega > \omega_{\mathrm{p}}$, the corrective model substitutes the imaginary component of the Drude model $\varepsilon''_{\mathrm{FC}}$ with

$$\begin{aligned}\varepsilon''_{\mathrm{FC}}(\omega) =& A\zeta^{-4} \int_{(1-\zeta)\theta(1-\zeta)}^{1} \left[\frac{1}{2} \ln \frac{\left(\sqrt{X+\zeta} + \sqrt{X}\right)^2 + X_{\mathrm{TF}}}{\left(\sqrt{X+\zeta} - \sqrt{X}\right)^2 + X_{\mathrm{TF}}} \right. \\ & \left. - \frac{2X_{\mathrm{TF}} \sqrt{X\left(X+\zeta\right)}}{\left[\left(\sqrt{X+\zeta} + \sqrt{X}\right)^2 + X_{\mathrm{TF}}\right]\left[\left(\sqrt{X+\zeta} - \sqrt{X}\right)^2 + X_{\mathrm{TF}}\right]} \right] dX \end{aligned} \tag{6.2}$$

where $\zeta = \frac{\hbar\omega}{E_{\mathrm{F}}}$, $X_{\mathrm{TF}} = \left(\frac{q_{\mathrm{TF}}}{k_{\mathrm{F}}}\right)^2$, $q_{\mathrm{TF}} = \sqrt{\frac{3Ne^2}{2\varepsilon_0 \varepsilon_\infty E_{\mathrm{F}}}}$ is the Thomas-Fermi screening wavevector, $A = \frac{1}{12\pi^3} \frac{e^2 \gamma k_{\mathrm{F}}^4}{\varepsilon_0 E_{\mathrm{F}}^3}$, $k_{\mathrm{F}} = \frac{\sqrt{2m_{\mathrm{e}}^* E_{\mathrm{F}}}}{\hbar}$ is the Fermi wavevector, $\gamma = R\left[\frac{Ze^2}{\varepsilon_0 \varepsilon_\infty k_{\mathrm{F}}^2}\right]^2$, and $\theta(x)$ is the Heaviside step function. Here, $\hbar$ is the reduced Planck constant, Z is the charge number of the impurity, and R denotes the number of impurities with charge $Z \cdot e$. Eq. 6.2 was derived assuming statically screened matrix elements for the interaction of electrons with ionized impurities. This static approximation of the dynamical screening of charges by conduction electrons breaks down at lower frequencies (i.e., $\omega < \omega_{\mathrm{p}}$), which is why the model is only valid for $\omega > \omega_{\mathrm{p}}$ [123]. With this new form for $\varepsilon''_{\mathrm{FC}}(\omega)$,

we can use the Kramers-Kronig relations to find the corresponding modification to the real part of the dielectric $\varepsilon'_{\mathrm{FC}}(\omega)$. We have confirmed that simply using $\varepsilon'_{\mathrm{FC}}$ from the original Drude model introduces less than 1% error in $\varepsilon'_{\mathrm{FC}}$ in a highly doped test case. Note that in Eq. 6.1, N is set to the doping concentration. For an InAs radiator with a doping level of $2 \times 10^{18}\,\mathrm{cm}^{-3}$ at 1000 K, accounting for thermally generated carriers results in a carrier concentration of $3.57 \times 10^{18}\,\mathrm{cm}^{-3}$. However, we find that neglecting the contribution of thermally excited carriers only results in a 0.025% overestimation of P and a 0.37% underestimation of η. The contribution of thermally excited carriers would become significant at lower doping concentrations and should be included in such cases. Our freely available implementation of the model, available in Ref. 184, includes an option to account for this contribution.

The proposed model more adequately represents the free carrier contribution and results in a good agreement with the experimental data at doping levels below $10^{18}\,\mathrm{cm}^{-3}$ (see Fig. 6.1). While this is a significant improvement, the model could be further refined as we continue to observe approximately a twofold overestimation of the free carrier contribution at high doping levels (e.g., $N_{\mathrm{d}} = 3.8 \times 10^{18}\,\mathrm{cm}^{-3}$ near 0.4 eV).

In Fig. 6.1b, we compare the spectral efficiency of a NFTPV system using an optimized InAs radiator computed with a Drude model to that computed with our proposed model; details on the optimization and calculation of spectral efficiency are in the next section. We find that the standard Drude model results in up to a 22% underestimation of the spectral efficiency due to the overestimation of below bandgap absorption.

6.1.3.2.2 Radiator Optimization

6.1.3.2.2.1 InAs as a Radiator

Using a one-dimensional fluctuational electrodynamics model from Ref. 98, which employs a frequency-domain Maxwell-equation solver, we attempt to improve NFTPV system performance via optimization of radiator material. Our goal is to determine

whether an InAs radiator outperforms a doped Si radiator in an InAs-based NFTPV system. We consider an InAs PV cell designed specifically for high efficiency NFTPV [78], which was designed assuming a silicon radiator, and compare the performance of a NFTPV system using a silicon or InAs radiator. The PV device modeled in this work consists of a p-i-n-n^+ InAs structure, depicted in Fig. 6.2, with the n^+ layer effectively forming a reflector for subgap radiation. The layers in this p-i-n-n^+ structure are designated as the front surface field (FSF), emitter, base, and back reflector (BR), respectively. Note that the high doping level in the BR layer is achievable experimentally [187]. This high doping level leads to $\omega_\mathrm{p} > E_\mathrm{g}$. As described in Section 6.1.3.2.1, the ionized impurity model is employed only for $\omega > \omega_\mathrm{p}$, so the BR layer uses the Drude model and thus has an overestimation of absorptivity. In all simulations, the PV cell is assumed to operate at 300 K. We assess the performance of NFTPV systems using two key metrics: the useful transferred power P and the spectral efficiency η [5],

$$P = \int_{\frac{E_\mathrm{g}}{\hbar}}^{\infty} \frac{E_\mathrm{g}}{\hbar\omega} Q(\omega)\mathrm{d}\omega, \tag{6.3}$$

$$\eta = \frac{P}{\int_0^\infty Q(\omega)\mathrm{d}\omega}, \tag{6.4}$$

where E_g is the bandgap energy and $Q(\omega)$ is the spectral heat flux. P is an upper limit to useful power, where we assume that all energy transfer with $\omega > E_\mathrm{g}/\hbar$ generates electron-hole pairs, and that they each give E_g of useful energy, also known as the Trivich-Flinn efficiency limit [188]. Note that the figures of merit presented in Eqs. 6.3 and 6.4 are not associated with a real diode, as the losses through electroluminescence—accounted for in the Shockley-Queisser model [189]—are not included. The spectral efficiency considers the inefficiencies from above-gap heat transfer, where the PV cell cannot use all of the energy, as well as subgap heat transfers that do not produce electron-hole pairs but still heat the PV cell.

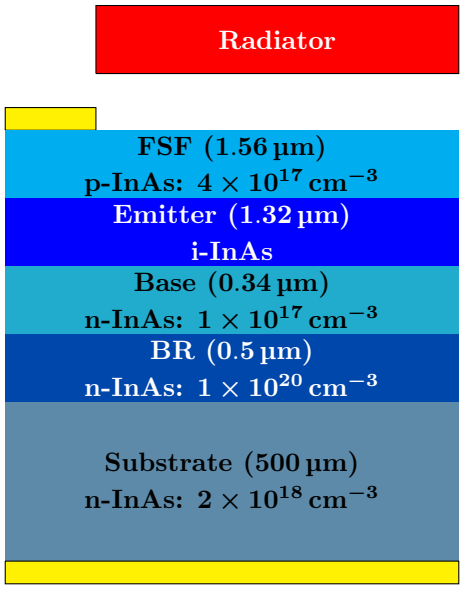

Figure 6.2: Illustration of the InAs-based NFTPV system for which we design an optimized radiator.

The radiative heat flux absorbed by the PV device depends on several factors, including the radiator doping level and thickness, gap, and temperature. Therefore, prior to comparing the performance of the two radiator materials, we must optimize the radiator parameters for various fixed gaps and temperatures.

6.1.3.2.2.2 Optimization of the Radiator Parameters

Before comparing radiator materials, we must first select appropriate thicknesses and doping levels. To ensure a fair comparison, we optimize these parameters for each radiator material. We choose four representative test conditions (700 and 1000 K radiator temperatures with 30 and 100 nm gaps) and optimize the radiator thickness and doping level at each test condition. Our goal is to select a radiator design that can perform well at a variety of temperatures and gaps. We first identify optimal designs for each test condition, and then select the design with the best average performance across the four test conditions.

We consider both finite and semi-infinite thickness radiators separately. We analyze the performance of semi-infinite thickness radiators to study the behavior of bulk ma-

terials. We simulate semi-infinite thickness radiators by generating an output medium behind the radiator made of the same material, neglecting any transmission through the layer. This semi-infinite medium removes any spurious Fabry-Pérot interference effect that can arise in the case of a finite stack. Radiators can effectively behave as semi-infinite at achievable thicknesses as low as 100 µm depending on the material and doping level, and this approach enables us to compute the performance of such bulk radiators much faster than if we considered large finite-thickness radiators.

We optimize for the quantity $P \cdot \eta$ since we want large power densities with high efficiency. Optimizing either P or η on its own does not capture these effects. Although optimizing P is essential, it is equally important to optimize η, as poor spectral efficiency leads to significant parasitic subgap radiation, heating the cell and increasing cooling requirements. We explored independent optimizations of P and η, but found that the optimization of one parameter often results in a significant reduction in the other. For instance, in the case of finite-thickness InAs, optimizing for P alone—compared to optimizing for $P \cdot \eta$—yields a 4.1% increase in P at the expense of more than a fivefold decrease in η.

Our optimizer relies on the Nelder-Mead method implemented in the Optim package in Julia. Initial guesses are generated using a coarse 5×5 grid for the doping level and radiator thickness. After finding optimal finite and semi-infinite designs for each material under each test condition, we normalize the $P \cdot \eta$ value by dividing it by its maximum across all radiator designs for each test condition. We then compute the average normalized $P \cdot \eta$ value across all test conditions and select the design with the largest average. The selected optimal finite and semi-infinite designs are reported in Table 6.1. In Table 6.1, we note that, for Si, a semi-infinite thickness radiator offers better performance, while for InAs, a finite thickness radiator is more effective. It is worth mentioning that in Table 6.1, the doping levels for the Bulk and Thin Si radiators differ significantly, as thinner radiators need higher carrier concentrations to be optically

thick above 0.35 eV. While semi-infinite radiators can behave as optically thick at low doping levels, finite-thickness radiators require higher doping levels to ensure sufficient free-carrier absorption above the InAs bandgap.

Table 6.1: Optimized finite and semi-infinite NFTPV radiator designs with their performance at each test condition.

Radiator Design	Radiator Material	Thickness [µm]	Doping [cm^{-3}]	$P \cdot \eta$ [$kW\,cm^{-2}$]			
				700 K		1000 K	
				30 nm	100 nm	30 nm	100 nm
Bulk InAs	n-doped InAs	∞	4.6×10^{18}	4.89	3.13	68.5	42.7
Finite InAs	n-doped InAs	6.5	2×10^{18}	5.15	3.56	68.8	43.6
Bulk Si	p-doped Si	∞	1×10^{17}	4.51	2.92	62.1	43.3
Finite Si	p-doped Si	100	1×10^{20}	2.94	2.45	52.4	40.3

6.1.3.2.2.3 InAs vs Si

We first compare, in Fig. 6.3, the performance of the two semi-infinite radiators, one InAs and the other Si, for which the doping level was optimized (Bulk InAs and Bulk Si designs). In the case of a semi-infinite radiator, InAs achieves significantly higher spectral efficiency, particularly at small gaps and elevated temperatures. InAs, however, suffers from more than 11% relative reduction in useful power at small gaps.

In Table 6.1, we note that, for Si, a semi-infinite radiator offers the best performance, while for an InAs radiator, a finite-thickness radiator is more effective. In fact, the Finite InAs radiator improves the average $P \cdot \eta$ by approximately 5%. We, therefore, compare these two best cases (Finite InAs design vs Bulk Si design) in Fig. 6.4. The Finite InAs radiator significantly improves spectral efficiency at larger gaps, while offering a useful power similar to that of a silicon radiator. Conversely, at smaller gaps, the thinner InAs radiator achieves greater useful power than the semi-infinite and is at most only 7% lower than the Si radiator, though this power comes with a small reduction in the spectral efficiency.

Since experimental NFTPV platforms often rely on thin films, we compare, in Fig. 6.5, the performance of the two radiator materials using finite-thickness designs ($< 100\,\mu m$).

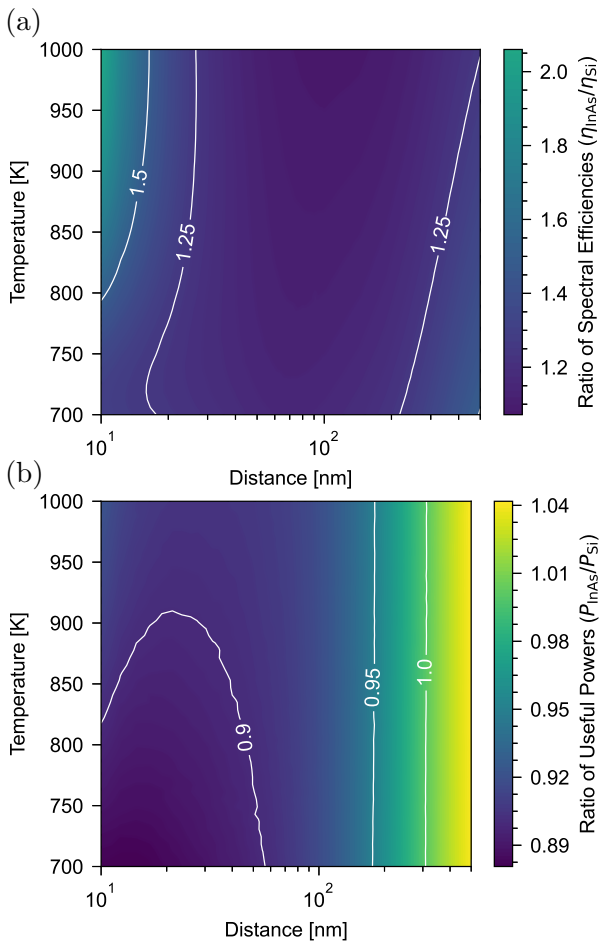

Figure 6.3: Bulk InAs vs Bulk Si: (a) Spectral efficiency ratio and (b) useful power ratio. For bulk radiators, InAs offers greater spectral efficiency at the expense of a relative reduction in useful power of over 11% at small gaps.

In this case, an InAs radiator significantly improves the spectral efficiency, achieving nearly a threefold enhancement at small distances, while only resulting in a reduction in useful power of at most 5%.

6.1.3.2.2.4 Underlying Phenomena

To study the origin of the spectral efficiency enhancement observed with an InAs radiator, Fig. 6.6 compares the spectral heat flux of both radiator materials. Compared to the Si radiator, subgap heat absorption is substantially reduced with the InAs radiator, without significantly affecting the above-bandgap heat absorption. This reduction is further illustrated in Fig. 6.7, which shows the spatially resolved spectral absorption in the

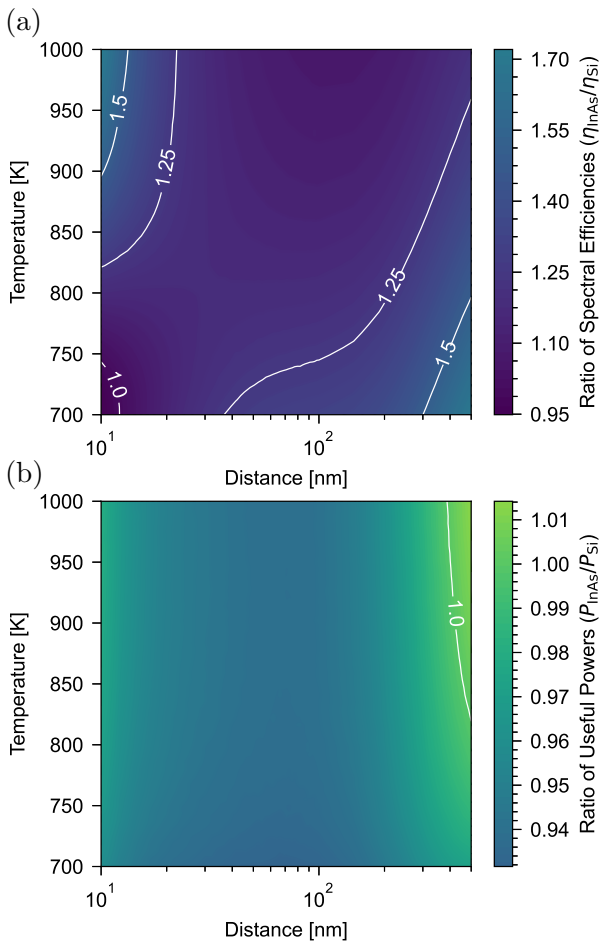

Figure 6.4: Best-case InAs vs best-case Si, i.e., Finite InAs vs Bulk Si: (a) Spectral efficiency ratio and (b) useful power ratio. An InAs radiator offers greater spectral efficiency and comparable useful power.

PV cell, accounting for the contributions from both evanescent and propagating modes. A comparison of Figs. 6.7a and 6.7b reveals that the InAs radiator significantly reduces the below-bandgap absorption in the n^+ layer that acts as a back reflector. Although a reduction in the front-surface p-region is not immediately apparent in Fig. 6.7, the InAs radiator results in a 53% reduction of below-bandgap absorption in this layer. While index matching generally leads to enhanced heat flux, this is not the effect observed in Fig. 6.6. Since the optical constants of InAs vary with temperature, the large temperature difference between the radiator and PV cell prevents the InAs radiator from benefiting from index matching. For example, the bandgap (0.354 eV at 300 K vs. 0.246 eV at

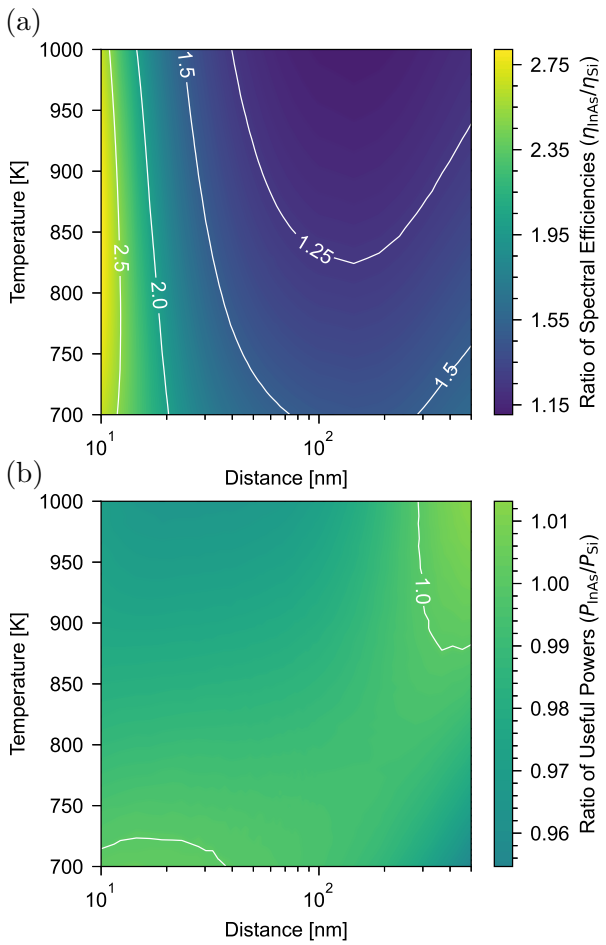

Figure 6.5: Finite InAs vs Finite Si: (a) Spectral efficiency ratio and (b) useful power ratio. For thin-film radiators, InAs offers greater spectral efficiency, achieving nearly a threefold enhancement at small distances, with a reduction in useful power of at most 5%.

700 K) varies significantly with temperature, so the radiator and PV cell have distinct optical properties, even if they are made of the same material.

To study how the optical properties of InAs results in such improvement, Fig. 6.8 contrasts the absorption coefficient of the FSF to the InAs radiator (i.e., doping of the Finite InAs design), and the Si radiator (i.e., doping of the Finite Si design). This comparison shows that the absorption coefficient of InAs is much lower than that of Si at energies just below the bandgap. According to the Kirchhoff law, under isothermal conditions, the emissivity of a material is proportional to its absorption coefficient. Therefore, the absorption coefficient of the radiator plays a crucial role in determining the radiative

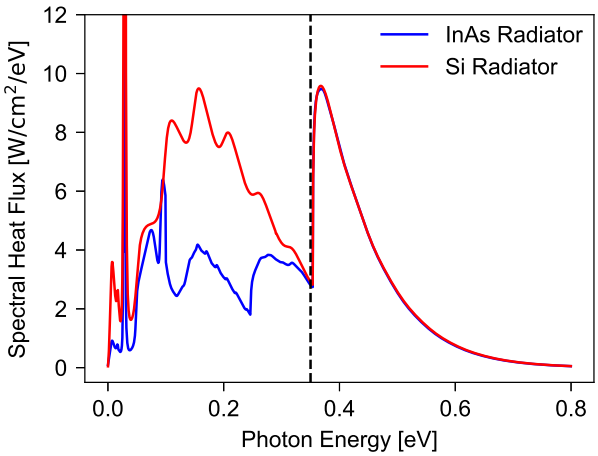

Figure 6.6: Spectral radiative heat transfer in an InAs-based NFTPV system using an InAs radiator (Finite InAs design, blue) and a Si radiator (Finite Si design, red) at 700 K and a separation of 100 nm.

heat flux. In this case, the lower subgap absorption coefficient of the InAs radiator could explain the reduction in subgap absorption in the BR layer.

We attribute the substantial below-bandgap absorption observed with the Si radiator to a surface polariton resonance. As shown in Fig. 6.9, for both radiator materials, at a 10 nm separation, the above-bandgap heat transfer is primarily influenced by frustrated modes occurring at a parallel wavevector k_ρ exceeding the vacuum wavevector k_v but lower than the material light lines (given by $\mathrm{Re}(n)k_\mathrm{v}$ where n is the refractive index of the material) [174]. These results also demonstrate that, for Si, the below-bandgap radiative heat flux is dominated by a resonance at $\omega = 0.0255\,\mathrm{eV}$. This resonance originates from surface polariton resonances in the Si radiator, since its parallel wavevector exceeds both material light lines. This below-bandgap surface resonance is anticipated since silicon has a plasma resonance below bandgap ($\omega_\mathrm{p} = 0.198\,\mathrm{eV}$ for the Finite Si design [124]). Conversely, InAs is a polar material with a resonance around 0.028 eV, which is slightly noticeable in Fig. 6.9a. However, this resonance is much narrower than the plasmonic resonance in Si, leading to less below-bandgap emission. Consequently, the presence of a slowly decaying below-bandgap surface polariton resonance in Si explains why an InAs radiator significantly enhances spectral efficiency.

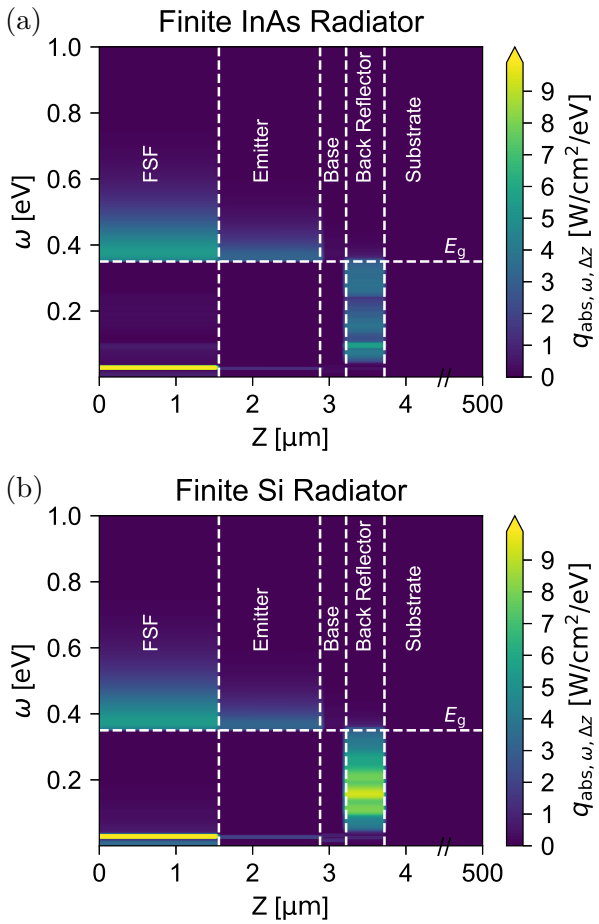

Figure 6.7: Spectral-spatial absorption distribution, $q_{\mathrm{abs},\omega,\Delta z}$, within the InAs cell for a separation of 100 nm and a radiator temperature of 700 K using (a) an InAs radiator (Finite InAs design) and (b) a Si radiator (Finite Si design).

6.1.3.3 Conclusions

We have demonstrated that the spectral efficiency of NFTPV systems can be greatly enhanced when both the PV cell and radiator are made of InAs. In such a case, spectral coupling results in a significant improvement in spectral efficiency compared to a doped Si radiator, achieving nearly a threefold enhancement at small distances. This improvement reduces the parasitic heating of the PV cell and increases its overall efficiency while not significantly affecting the power density. Additionally, utilizing InAs for both the PV cell and the radiator could be advantageous for monolithic fabrication in a single crystal growth process for both the radiator and the PV cell. During our analysis, we also

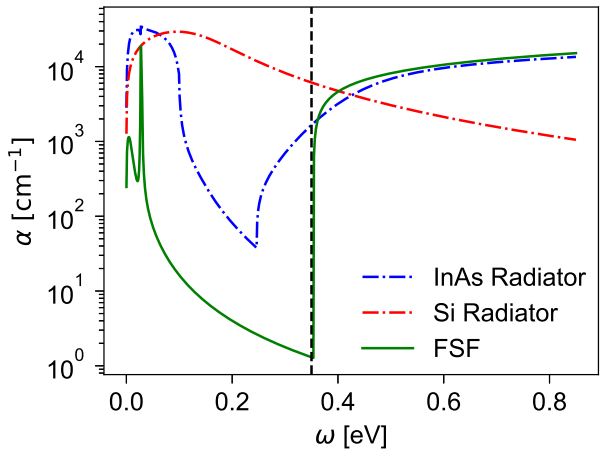

Figure 6.8: Absorption coefficient of the FSF layer of the InAs PV cell at 300 K (green), compared with the absorption coefficient of an InAs radiator (Finite InAs design, blue) and a Si radiator (Finite Si design, red), both at 700 K.

uncovered an overestimation of free carrier absorption in InAs dielectric function models. We implement a corrective model and demonstrate that it accurately represents the absorption at moderate doping levels but could be further refined for improved accuracy at higher doping levels.

Acknowledgments

The authors thank Mathieu Francoeur from the University of Utah and Daniel Milovich from the Universidad Politécnica de Madrid for useful discussions on the dielectric model of InAs. The authors also thank Mauro Antezza from the Institut Universitaire de France for stimulating discussions on the Kramers-Kronig relations. The authors also extend their gratitude to University of Ottawa colleague Gavin Forcade for discussions on permittivity and heat transfer calculation algorithms. This work was funded by the Natural Sciences and Engineering Research Council of Canada (NSERC) through the CREATE TOP-SET program (No. 497981) and the CGS-D program.

Appendix. Kramers-Kronig Relations in InAs Dielectric Model

In Ref. 117, the real part of the interband refractive index n'_{IB} is calculated from the imaginary part of the interband refractive index n''_{IB}, using the Kramers-Kronig rela-

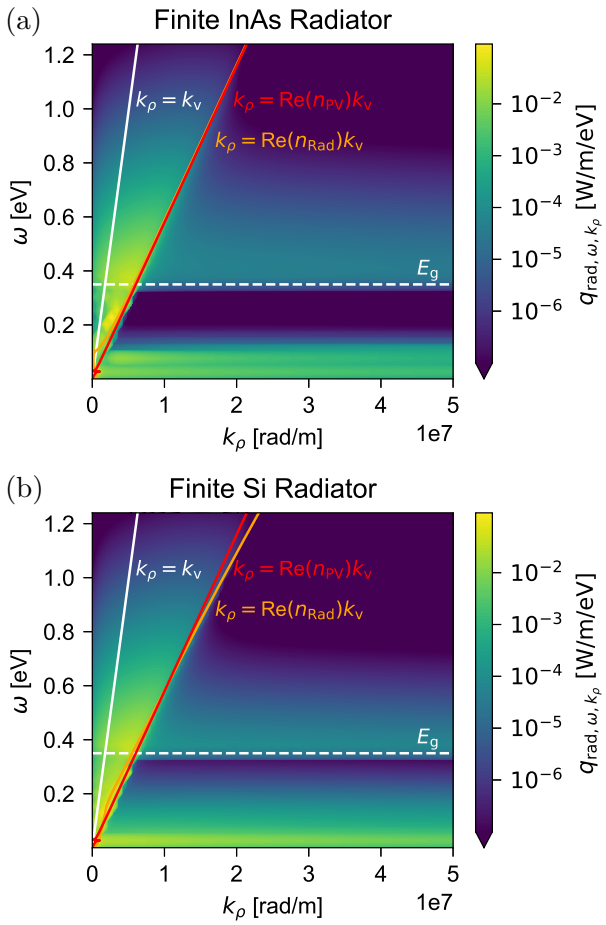

Figure 6.9: Radiative heat flux, $q_{\mathrm{rad},\omega,k_\rho}$, per unit angular frequency, ω, and parallel wavevector, k_ρ, at a 10 nm separation and a radiator temperature of 700 K for (a) an InAs radiator (Finite InAs design) and (b) a Si radiator (Finite Si design). For both materials, the above-bandgap radiative heat flux is primarily influenced by frustrated modes ($k_\mathrm{v} < k_\rho < k_\mathrm{v}\min\left(\mathrm{Re}(n_\mathrm{Rad}), \mathrm{Re}(n_\mathrm{PV})\right)$), while propagating modes ($k_\rho < k_\mathrm{v}$) have modest contributions. For Si, the below-bandgap radiative heat flux is significantly dominated by surface polariton resonances ($k_\rho > k_\mathrm{v}\min\left(\mathrm{Re}(n_\mathrm{Rad}), \mathrm{Re}(n_\mathrm{PV})\right)$).

tions. Similarly, the contribution from Eq. 6.2 to the real part of the permittivity ε', can be determined using the Kramers-Kronig relations. Unfortunately, the Kramers-Kronig relations can be computationally expensive. Therefore, to avoid a Kramers-Kronig calculation, we instead approximate $n'_\mathrm{IB} = \sqrt{\varepsilon_\infty}$, following the approach of Ref. 78, and employ the Drude model to describe the real part of the permittivity due to free carrier absorption. We find that this approximation results in an underestimation of both the useful transferred power and the spectral efficiency of approximately 1% and 4%, relative,

respectively.

Note that NFTPV simulations only require optical constants up to approximately 1.5 eV, although the Kramers-Kronig relations involve integration over the entire frequency range. In our dielectric model, the interband absorption model, taken from Ref. 120, is based on $k \cdot p$ theory and is therefore only valid near the absorption edge. In this case, the light-hole absorption contribution obeys $\alpha_{\mathrm{lh}}(\omega) \sim \omega$ as $\omega \to \infty$, leading to a non-convergent Kramers-Kronig relation. This limit is not physical, and the α_{lh} term can be smoothly suppressed at energies above 1 eV with only a few percent change in the Kramers-Kronig derived interband refractive index n'_{IB} depending on the exact form of the suppression function. We consider such changes to be within the expected errors for the modeled optical constants. Also note that we evaluate the interband absorption coefficient α_{IB} by considering only the contributions from the light-hole and heavy-hole bands, as the contributions from remote bands are accounted for in ε_∞. Absorption from the split-off hole band begins at approximately 0.75 eV, and above this energy, α_{IB} is already underestimated.

7. Conclusions and Recommendations

7.1 Summary

To conclude, within the scope of Objectives 1 and 2, we developed a flexible NFRHT platform and experimentally demonstrated the potential of using nanomechanical resonators as temperature sensors for NFRHT measurements. Relying on Platform 1, we demonstrated that nanomechanical resonators enable a temperature resolution (i.e., 1.2×10^{-6} K) unparalleled in previous NFRHT experiments. Given the well-established protocols for depositing materials on SiN, this platform could facilitate the exploration of many new interesting materials for NFRHT. We also demonstrated, relying on Platform 2 with its improved alignment capabilities and refined geometries, that SiN membranes can enable NFRHT measurements in the deep sub-wavelength regime without the need for custom-fabricated microdevices, aside from the relatively common SiN membrane. The total measured radiative heat transfer (i.e., across the entire resonator area) remains dominated by propagating modes, although using a smaller resonator ($\lesssim (0.25\text{ mm})^2$) could enable measurements primarily governed by surface polaritons. Additionally, this work provides us with an opportunity for measuring NFRHT and the Casimir effect simultaneously using nanomechanical resonators.

Within the scope of Objective 3, we first demonstrated, using Platform 3, that employing large thermal mass radiators significantly limits the capability of positioner-based NFTPV approaches. These radiators generate excessive parasitic radiation, which interferes with measurements, and their geometry complicates the alignment procedure. Localized heating elements not only appear essential for non-static NFTPV systems but also enable vibrational contact detection, further simplifying the alignment process. Based on these findings, we propose a revised approach (i.e., Platform 4), which relies on a

localized heating element. Unfortunately, such heating elements would be classified as custom devices and, therefore, limit the versatility of the platform. However, we argue that while these heating elements may complicate the testing of new radiator materials, Platform 4 could still be considered flexible. In fact, with a properly designed radiator, such as the one in Platform 4, the platform could enable the testing of PV cells of various materials and geometries.

Note that, here, Platforms 1, 2, 3, and 4 are regarded as flexible platforms for testing purposes, rather than for application use. In fact, the experimental platforms reported in this thesis are positioner-based approaches that could enable the testing of many new materials for NFRHT and NFTPV. While positioner-based approaches are crucial to the investigation of various geometries and materials, they do not constitute a deployable technology. We strongly believe that static devices are key for attaining practical applications.

Lastly, in the scope of Objective 4, we demonstrated that the spectral efficiency of NFTPV systems can be greatly enhanced when both the PV cell and radiator are made of InAs. In such a case, spectral coupling results in a nearly threefold enhancement of spectral efficiency when compared to a doped Si radiator. This improvement reduces the parasitic heating of the PV cell and increases its overall efficiency while not significantly affecting the power density. Additionally, utilizing InAs for both the PV cell and the radiator could be advantageous for monolithic fabrication in a single growth process for both the radiator and the PV cell. Through this work, we also uncovered an overestimation of free carrier absorption in InAs dielectric function models. We proposed a corrective model and demonstrated that it accurately represents the absorption at moderate doping levels but could be further refined for improved accuracy at higher doping levels.

To summarize, we developed a platform that could allow for the investigation of new phenomena between two closely spaced objects using nanomechanical resonators. We believe that the wide availability of freestanding SiN substrates could make this plat-

form a go-to approach for studying new materials for NFRHT. Conversely, for NFTPV measurements, the design of a specialized heating element has turned out to be more complex than anticipated. In fact, our current heating elements proved to be unsuitable for NFTPV measurements. Consequently, we were unable to develop a platform for the experimental testing of new PV materials for NFTPV applications. Moving forward, the design of a localized heating element would be essential to NFTPV measurements. Finally, based on our theoretical investigation, we identify InAs as a promising radiator material for future NFTPV experiments. Additionally, through our investigation, we uncovered an overestimation of free carrier absorption in InAs dielectric function models and proposed a corrective model.

7.2 Future Work

Looking ahead, several directions could be pursued to build upon the findings of this work. Concerning our nanomechanical resonator-based NFRHT platform, exploring new materials presents a promising avenue. Developing an automated alignment procedure could simplify this investigation by improving repeatability and accelerating the measurement process. An optimization of the geometry of the components could further improve the platform. More specifically, using a smaller resonator and radiator while increasing the radius of curvature of the radiator may improve thermal isolation and near-field interaction. The heating element could also be made significantly smaller to minimize parasitic radiation. Additionally, reorienting the platform to allow an in-plane view could simplify the alignment process. Finally, validating simultaneous Casimir and NFRHT measurements would further establish the versatility of our proposed platform.

Regarding NFTPV measurements, as previously stated, the development of localized heating elements enabling contact detection and minimizing parasitic radiation could be a promising direction. Incorporating such a heating element into our platform could allow for valuable testing of various novel PV cell designs. Finally, incorporating a

thermoelectric cooler behind the PV cell may be beneficial, as effective cooling is essential for NFTPV measurements.

Regarding our theoretical investigation, we designed a radiator for a specific InAs cell, developed based on the findings from Ref. 78 while accounting for fabrication constraints. However, assessing the performance of the radiator with other cell designs remains an interesting direction for future investigation. Furthermore, the refinement and experimental validation of the InAs dielectric model could help capture additional physical process that contribute to absorption, thereby enhancing accuracy at higher doping levels. Finally, investigating other III-V materials for the radiator may provide valuable insights.

As previously stated, we strongly believe that static devices represent the most viable option for practical applications. Future NFTPV systems will likely resemble the configuration employed in Ref. 59, where both the radiator and PV cell are composed of III-V materials, as this approach may simplify fabrication. The findings reported in this thesis pave the way for designing high-performance static devices. The experimental framework developed here offers opportunities for testing new materials for NFTPV as well as for evaluating novel PV cell designs. Finally, our theoretical investigation provides key insights into material selection and optimization that can guide the design of III-V–based NFTPV static platforms.

References

[1] M. Laroche, R. Carminati, and J.-J. Greffet, "Near-field thermophotovoltaic energy conversion," *Journal of Applied Physics*, vol. 100, no. 6, p. 063704, 2006.

[2] B. Zhao, K. Chen, S. Buddhiraju, G. Bhatt, M. Lipson, and S. Fan, "High-performance near-field thermophotovoltaics for waste heat recovery," *Nano Energy*, vol. 41, pp. 344 – 350, 2017.

[3] S. Molesky and Z. Jacob, "Ideal near-field thermophotovoltaic cells," *Phys. Rev. B*, vol. 91, p. 205435, May 2015.

[4] O. Ilic, M. Jablan, J. D. Joannopoulos, I. Celanovic, and M. Soljačić, "Overcoming the black body limit in plasmonic and graphene near-field thermophotovoltaic systems," *Opt. Express*, vol. 20, pp. A366–A384, May 2012.

[5] R. St-Gelais, G. R. Bhatt, L. Zhu, S. Fan, and M. Lipson, "Hot carrier-based near-field thermophotovoltaic energy conversion," *ACS Nano*, vol. 11, p. 3001–3009, Mar. 2017.

[6] A. Fiorino, L. Zhu, D. Thompson, R. Mittapally, P. Reddy, and E. Meyhofer, "Nanogap near-field thermophotovoltaics," *Nature nanotechnology*, vol. 13, p. 806—811, Sep 2018.

[7] R. S. DiMatteo, P. Greiff, S. L. Finberg, K. A. Young-Waithe, H. K. H. Choy, M. M. Masaki, and C. G. Fonstad, "Enhanced photogeneration of carriers in a semiconductor via coupling across a nonisothermal nanoscale vacuum gap," *Applied Physics Letters*, vol. 79, no. 12, pp. 1894–1896, 2001.

[8] G. R. Bhatt, B. Zhao, S. Roberts, I. Datta, A. Mohanty, T. Lin, J.-M. Hartmann,

R. St-Gelais, S. Fan, and M. Lipson, "Integrated near-field thermo-photovoltaics for heat recycling," *Nature Communications*, vol. 11, p. 2545, Dec 2020.

[9] L. Zhu, C. R. Otey, and S. Fan, "Ultrahigh-contrast and large-bandwidth thermal rectification in near-field electromagnetic thermal transfer between nanoparticles," *Phys. Rev. B*, vol. 88, p. 184301, Nov 2013.

[10] S.-A. Biehs, F. S. S. Rosa, and P. Ben-Abdallah, "Modulation of near-field heat transfer between two gratings," *Applied Physics Letters*, vol. 98, no. 24, p. 243102, 2011.

[11] P. Ben-Abdallah, A. Belarouci, L. Frechette, and S.-A. Biehs, "Heat flux splitter for near-field thermal radiation," *Applied Physics Letters*, vol. 107, no. 5, p. 053109, 2015.

[12] B. Guha, C. Otey, C. B. Poitras, S. Fan, and M. Lipson, "Near-field radiative cooling of nanostructures," *Nano Letters*, vol. 12, p. 4546–4550, Sep 2012.

[13] S.-A. Biehs, "Thermal heat radiation, near-field energy density and near-field radiative heat transfer of coated materials," *The European Physical Journal B*, vol. 58, p. 423–431, Aug 2007.

[14] H. Salihoglu and X. Xu, "Near-field radiative heat transfer enhancement using natural hyperbolic material," *Journal of Quantitative Spectroscopy and Radiative Transfer*, vol. 222-223, pp. 115–121, 2019.

[15] S. Basu, Y. Yang, and L. Wang, "Near-field radiative heat transfer between metamaterials coated with silicon carbide thin films," *Applied Physics Letters*, vol. 106, no. 3, p. 033106, 2015.

[16] K. Kim, B. Song, V. Fernández-Hurtado, W. Lee, W. Jeong, L. Cui, D. Thompson,

J. Feist, M. T. H. Reid, F. J. García-Vidal, and et al., "Radiative heat transfer in the extreme near field," *Nature*, vol. 528, p. 387–391, Dec 2015.

[17] M. Francoeur, M. P. Mengüç, and R. Vaillon, "Near-field radiative heat transfer enhancement via surface phonon polaritons coupling in thin films," *Applied Physics Letters*, vol. 93, no. 4, p. 043109, 2008.

[18] W. Jin, S. Molesky, Z. Lin, and A. W. Rodriguez, "Material scaling and frequency-selective enhancement of near-field radiative heat transfer for lossy metals in two dimensions via inverse design," *Phys. Rev. B*, vol. 99, p. 041403, Jan 2019.

[19] E. Moncada-Villa, V. Fernández-Hurtado, F. J. García-Vidal, A. García-Martín, and J. C. Cuevas, "Magnetic field control of near-field radiative heat transfer and the realization of highly tunable hyperbolic thermal emitters," *Phys. Rev. B*, vol. 92, p. 125418, Sep 2015.

[20] J. R. Howell, M. P. Mengüç, K. Daun, and R. Siegel, *Thermal Radiation Heat Transfer*. CRC Press, 7 ed., Dec 2020.

[21] E. G. Cravalho, C. L. Tien, and R. P. Caren, "Effect of small spacings on radiative transfer between two dielectrics," *Journal of Heat Transfer*, vol. 89, pp. 351–358, November 1967.

[22] D. Polder and M. Van Hove, "Theory of radiative heat transfer between closely spaced bodies," *Phys. Rev. B*, vol. 4, pp. 3303–3314, Nov 1971.

[23] J. B. Pendry, "Radiative exchange of heat between nanostructures," *Journal of Physics: Condensed Matter*, vol. 11, pp. 6621–6633, aug 1999.

[24] R. Carminati and J.-J. Greffet, "Near-field effects in spatial coherence of thermal sources," *Phys. Rev. Lett.*, vol. 82, pp. 1660–1663, Feb 1999.

[25] A. I. Volokitin and B. N. J. Persson, "Radiative heat transfer between nanostructures," *Phys. Rev. B*, vol. 63, p. 205404, Apr 2001.

[26] A. Babuty, K. Joulain, P.-O. Chapuis, J.-J. Greffet, and Y. De Wilde, "Blackbody spectrum revisited in the near field," *Phys. Rev. Lett.*, vol. 110, p. 146103, Apr 2013.

[27] P. Ben-Abdallah and S.-A. Biehs, "Near-field thermal transistor," *Phys. Rev. Lett.*, vol. 112, p. 044301, Jan 2014.

[28] C. Forman, I. K. Muritala, R. Pardemann, and B. Meyer, "Estimating the global waste heat potential," *Renewable and Sustainable Energy Reviews*, vol. 57, pp. 1568–1579, 2016.

[29] I. A. O. Tedah, F. Maculewicz, D. E. Wolf, and R. Schmechel, "Thermoelectrics versus thermophotovoltaics: two approaches to convert heat fluxes into electricity," *Journal of Physics D: Applied Physics*, vol. 52, p. 275501, may 2019.

[30] R. He, D. Kraemer, J. Mao, L. Zeng, Q. Jie, Y. Lan, C. Li, J. Shuai, H. S. Kim, Y. Liu, D. Broido, C.-W. Chu, G. Chen, and Z. Ren, "Achieving high power factor and output power density in p-type half-heuslers nb 1-x ti x fesb," *Proceedings of the National Academy of Sciences*, vol. 113, p. 13576–13581, Nov. 2016.

[31] A. Datas and R. Vaillon, "Thermionic-enhanced near-field thermophotovoltaics," *Nano Energy*, vol. 61, pp. 10–17, 2019.

[32] K. Kloppstech, N. Könne, S.-A. Biehs, A. W. Rodriguez, L. Worbes, D. Hellmann, and A. Kittel, "Giant heat transfer in the crossover regime between conduction and radiation," *Nature Communications*, vol. 8, p. 14475, Apr 2017.

[33] J. Xu, K. Läuger, R. Möller, K. Dransfeld, and I. H. Wilson, "Heat transfer between

two metallic surfaces at small distances," *Journal of Applied Physics*, vol. 76, no. 11, pp. 7209–7216, 1994.

[34] B. Song, Y. Ganjeh, S. Sadat, D. Thompson, A. Fiorino, V. Fernández-Hurtado, J. Feist, F. J. Garcia-Vidal, J. C. Cuevas, P. Reddy, and et al., "Enhancement of near-field radiative heat transfer using polar dielectric thin films," *Nature Nanotechnology*, vol. 10, p. 253–258, Mar 2015.

[35] E. Rousseau, A. Siria, G. Jourdan, S. Volz, F. Comin, J. Chevrier, and J.-J. Greffet, "Radiative heat transfer at the nanoscale," *Nature Photonics*, vol. 3, p. 514–517, Sep 2009.

[36] A. Narayanaswamy, S. Shen, and G. Chen, "Near-field radiative heat transfer between a sphere and a substrate," *Phys. Rev. B*, vol. 78, p. 115303, Sep 2008.

[37] F. Menges, M. Dittberner, L. Novotny, D. Passarello, S. S. P. Parkin, M. Spieser, H. Riel, and B. Gotsmann, "Thermal radiative near field transport between vanadium dioxide and silicon oxide across the metal insulator transition," *Applied Physics Letters*, vol. 108, no. 17, p. 171904, 2016.

[38] K. Shi, Y. Sun, Z. Chen, N. He, F. Bao, J. Evans, and S. He, "Colossal enhancement of near-field thermal radiation across hundreds of nanometers between millimeter-scale plates through surface plasmon and phonon polaritons coupling," *Nano Letters*, vol. 19, p. 8082–8088, Nov 2019.

[39] M. Lim, J. Song, S. S. Lee, and B. J. Lee, "Tailoring near-field thermal radiation between metallo-dielectric multilayers using coupled surface plasmon polaritons," *Nature Communications*, vol. 9, p. 4302, Dec 2018.

[40] R. St-Gelais, L. Zhu, S. Fan, and M. Lipson, "Near-field radiative heat transfer between parallel structures in the deep subwavelength regime," *Nature Nanotechnology*, vol. 11, pp. 515 – 519, March 2016.

[41] H. Salihoglu, W. Nam, L. Traverso, M. Segovia, P. K. Venuthurumilli, W. Liu, Y. Wei, W. Li, and X. Xu, "Near-field thermal radiation between two plates with sub-10 nm vacuum separation," *Nano Letters*, vol. 20, p. 6091–6096, Aug 2020.

[42] R. S. Ottens, V. Quetschke, S. Wise, A. A. Alemi, R. Lundock, G. Mueller, D. H. Reitze, D. B. Tanner, and B. F. Whiting, "Near-field radiative heat transfer between macroscopic planar surfaces," *Phys. Rev. Lett.*, vol. 107, p. 014301, Jun 2011.

[43] T. Kralik, P. Hanzelka, M. Zobac, V. Musilova, T. Fort, and M. Horak, "Strong near-field enhancement of radiative heat transfer between metallic surfaces," *Phys. Rev. Lett.*, vol. 109, p. 224302, Nov 2012.

[44] T. Ijiro and N. Yamada, "Near-field radiative heat transfer between two parallel sio2 plates with and without microcavities," *Applied Physics Letters*, vol. 106, no. 2, p. 023103, 2015.

[45] M. Ghashami, H. Geng, T. Kim, N. Iacopino, S. K. Cho, and K. Park, "Precision measurement of phonon-polaritonic near-field energy transfer between macroscale planar structures under large thermal gradients," *Phys. Rev. Lett.*, vol. 120, p. 175901, Apr 2018.

[46] C. Hargreaves, "Anomalous radiative transfer between closely-spaced bodies," *Physics Letters A*, vol. 30, no. 9, pp. 491–492, 1969.

[47] P. Sabbaghi, L. Long, X. Ying, L. Lambert, S. Taylor, C. Messner, and L. Wang, "Super-planckian radiative heat transfer between macroscale metallic surfaces due to near-field and thin-film effects," *Journal of Applied Physics*, vol. 128, no. 2, p. 025305, 2020.

[48] L. Tang, J. DeSutter, and M. Francoeur, "Near-field radiative heat transfer between

dissimilar materials mediated by coupled surface phonon- and plasmon-polaritons," *ACS Photonics*, vol. 7, p. 1304–1311, May 2020.

[49] L. Hu, A. Narayanaswamy, X. Chen, and G. Chen, "Near-field thermal radiation between two closely spaced glass plates exceeding planck's blackbody radiation law," *Applied Physics Letters*, vol. 92, no. 13, p. 133106, 2008.

[50] K. Ito, A. Miura, H. Iizuka, and H. Toshiyoshi, "Parallel-plate submicron gap formed by micromachined low-density pillars for near-field radiative heat transfer," *Applied Physics Letters*, vol. 106, no. 8, p. 083504, 2015.

[51] S. Lang, G. Sharma, S. Molesky, P. U. Kränzien, T. Jalas, Z. Jacob, A. Y. Petrov, and M. Eich, "Dynamic measurement of near-field radiative heat transfer," *Scientific Reports*, vol. 7, p. 13916, Dec 2017.

[52] C. Feng, Z. Tang, J. Yu, and C. Sun, "A mems device capable of measuring near-field thermal radiation between membranes," *Sensors*, vol. 13, no. 2, pp. 1998–2010, 2013.

[53] C. Lucchesi, D. Cakiroglu, J.-P. Perez, T. Taliercio, E. Tournié, P.-O. Chapuis, and R. Vaillon, "Near-field thermophotovoltaic conversion with high electrical power density and cell efficiency above 14%," *Nano Letters*, vol. 21, p. 4524–4529, Jun 2021.

[54] L. Tang, L. M. Corrêa, M. Francoeur, and C. Dames, "Corner- and edge-mode enhancement of near-field radiative heat transfer," *Nature*, vol. 629, p. 67–73, May 2024.

[55] A. C. Jones and M. B. Raschke, "Thermal infrared near-field spectroscopy," *Nano Letters*, vol. 12, p. 1475–1481, Mar. 2012.

[56] J. I. Watjen, B. Zhao, and Z. M. Zhang, "Near-field radiative heat transfer between doped-si parallel plates separated by a spacing down to 200 nm," *Applied Physics Letters*, vol. 109, p. 203112, Nov. 2016.

[57] H. Iizuka and S. Fan, "Rectification of evanescent heat transfer between dielectric-coated and uncoated silicon carbide plates," *Journal of Applied Physics*, vol. 112, p. 024304, 07 2012.

[58] R. Mittapally, A. Majumder, P. Reddy, and E. Meyhofer, "Near-field thermophotovoltaic energy conversion: progress and opportunities," *Physical Review Applied*, vol. 19, no. 3, p. 037002, 2023.

[59] J. Selvidge, R. M. France, J. Goldsmith, P. Solanki, M. A. Steiner, and E. J. Tervo, "Large area near-field thermophotovoltaics for low temperature applications," *Advanced Materials*, vol. 37, no. 5, p. 2411524, 2025.

[60] W. Müller-Hirsch, A. Kraft, M. T. Hirsch, J. Parisi, and A. Kittel, "Heat transfer in ultrahigh vacuum scanning thermal microscopy," *Journal of Vacuum Science & Technology A*, vol. 17, no. 4, pp. 1205–1210, 1999.

[61] P. J. van Zwol, L. Ranno, and J. Chevrier, "Tuning near field radiative heat flux through surface excitations with a metal insulator transition," *Phys. Rev. Lett.*, vol. 108, p. 234301, Jun 2012.

[62] S. Shen, A. Mavrokefalos, P. Sambegoro, and G. Chen, "Nanoscale thermal radiation between two gold surfaces," *Applied Physics Letters*, vol. 100, no. 23, p. 233114, 2012.

[63] D. L. Nika and A. A. Balandin, "Two-dimensional phonon transport in graphene," *Journal of Physics: Condensed Matter*, vol. 24, p. 233203, may 2012.

[64] K. Shi, F. Bao, and S. He, "Enhanced near-field thermal radiation based on multilayer graphene-hbn heterostructures," *ACS Photonics*, vol. 4, p. 971–978, Apr 2017.

[65] C. Lucchesi, R. Vaillon, and P.-O. Chapuis, "Radiative heat transfer at the nanoscale: experimental trends and challenges," *Nanoscale Horiz.*, vol. 6, pp. 201–208, 2021.

[66] C. Zhang, M. Giroux, T. A. Nour, and R. St-Gelais, "Radiative heat transfer in freestanding silicon nitride membranes," *Phys. Rev. Appl.*, vol. 14, p. 024072, Aug 2020.

[67] C. Zhang and R. St-Gelais, "Demonstration of frequency stability limited by thermal fluctuation noise in silicon nitride nanomechanical resonators," *Applied Physics Letters*, vol. 122, p. 193501, 05 2023.

[68] L. Laurent, J.-J. Yon, J.-S. Moulet, M. Roukes, and L. Duraffourg, "12$-\mu$m-pitch electromechanical resonator for thermal sensing," *Phys. Rev. Appl.*, vol. 9, p. 024016, Feb 2018.

[69] M. Piller, P. Sadeghi, R. G. West, N. Luhmann, P. Martini, O. Hansen, and S. Schmid, "Thermal radiation dominated heat transfer in nanomechanical silicon nitride drum resonators," *Applied Physics Letters*, vol. 117, p. 034101, 07 2020.

[70] X. C. Zhang, E. B. Myers, J. E. Sader, and M. L. Roukes, "Nanomechanical torsional resonators for frequency-shift infrared thermal sensing," *Nano Letters*, vol. 13, p. 1528–1534, Apr. 2013.

[71] M. Piller, J. Hiesberger, E. Wistrela, P. Martini, N. Luhmann, and S. Schmid, "Thermal ir detection with nanoelectromechanical silicon nitride trampoline resonators," *IEEE Sensors Journal*, vol. 23, no. 2, pp. 1066–1071, 2023.

[72] Y. Hui, J. S. Gomez-Diaz, Z. Qian, A. Alu, and M. Rinaldi, "Plasmonic piezoelectric nanomechanical resonator for spectrally selective infrared sensing," *Nature communications*, vol. 7, no. 1, p. 11249, 2016.

[73] A. Blaikie, D. Miller, and B. J. Alemán, "A fast and sensitive room-temperature graphene nanomechanical bolometer," *Nature Communications*, vol. 10, p. 4726, oct 2019.

[74] Y. Zhang, Y. Watanabe, S. Hosono, N. Nagai, and K. Hirakawa, "Room temperature, very sensitive thermometer using a doubly clamped microelectromechanical beam resonator for bolometer applications," *Applied Physics Letters*, vol. 108, no. 16, 2016.

[75] C. Zhang, E. K. Yalavarthi, M. Giroux, W. Cui, M. Stephan, A. Maleki, A. Weck, J.-M. Ménard, and R. St-Gelais, "High detectivity terahertz radiation sensing using frequency-noise-optimized nanomechanical resonators," *APL Photonics*, vol. 9, p. 126105, 12 2024.

[76] Q. Lu, X. Zhou, A. Krysa, A. Marshall, P. Carrington, C.-H. Tan, and A. Krier, "Inas thermophotovoltaic cells with high quantum efficiency for waste heat recovery applications below 1000 c," *Solar Energy Materials and Solar Cells*, vol. 179, pp. 334–338, 2018.

[77] R. Mittapally, B. Lee, L. Zhu, A. Reihani, J. W. Lim, D. Fan, S. R. Forrest, P. Reddy, and E. Meyhofer, "Near-field thermophotovoltaics for efficient heat to electricity conversion at high power density," *Nature Communications*, vol. 12, p. 4364, Jul 2021.

[78] G. P. Forcade, C. E. Valdivia, S. Molesky, S. Lu, A. W. Rodriguez, J. J. Krich, R. St-Gelais, and K. Hinzer, "Efficiency-optimized near-field thermophotovoltaics using InAs and InAsSbP," *Applied Physics Letters*, vol. 121, p. 193903, 11 2022.

[79] T. Inoue, T. Koyama, D. D. Kang, K. Ikeda, T. Asano, and S. Noda, "One-chip near-field thermophotovoltaic device integrating a thin-film thermal emitter and photovoltaic cell," *Nano Letters*, vol. 19, p. 3948–3952, June 2019.

[80] M. Alam and D. Cameron, "Investigation of annealing effects on sol–gel deposited indium tin oxide thin films in different atmospheres," *Thin Solid Films*, vol. 420-421, pp. 76–82, 2002. Proceedings of the 29th International Conference on Metallurgic Coatings and Thin Films.

[81] M. Planck, "On the law of distribution of energy in the normal spectrum," *Annalen der physik*, vol. 4, no. 553, p. 1, 1901.

[82] T. L. Bergman, F. P. Incropera, D. P. DeWitt, and A. S. Lavine, *Fundamentals of heat and mass transfer*. John Wiley & Sons, 2011.

[83] F. L. Pedrotti, L. M. Pedrotti, and L. S. Pedrotti, *Introduction to optics*. Cambridge University Press, 2017.

[84] M. Francoeur, *Near-Field Thermal Radiation*, p. 979–1021. Cham: Springer International Publishing, 2018.

[85] S.-A. Biehs, R. Messina, P. S. Venkataram, A. W. Rodriguez, J. C. Cuevas, and P. Ben-Abdallah, "Near-field radiative heat transfer in many-body systems," *Rev. Mod. Phys.*, vol. 93, p. 025009, Jun 2021.

[86] J. K.-K. Tong, *Photonic engineering of near- and far-field radiative heat transfer*. Thesis, Massachusetts Institute of Technology, 2016.

[87] S. Zhu, A. Yu, D. Hawley, and R. Roy, "Frustrated total internal reflection: A demonstration and review," *American Journal of Physics - AMER J PHYS*, vol. 54, pp. 601–607, 07 1986.

[88] M. Francoeur, *Near-field radiative transfer: Thermal radiation, thermophotovoltaic power generation and optical characterization.* PhD thesis, University of Kentucky, Lexington, KY, Jan. 2010.

[89] K. Joulain, J.-P. Mulet, F. Marquier, R. Carminati, and J.-J. Greffet, "Surface electromagnetic waves thermally excited: Radiative heat transfer, coherence properties and casimir forces revisited in the near field," *Surface Science Reports*, vol. 57, no. 3, pp. 59 – 112, 2005.

[90] S. A. Maier, *Plasmonics: Fundamentals and Applications.* New York, NY: Springer US, 2007.

[91] S. M. Rytov and H. Erkku, *Theory of electric fluctuations and thermal radiation.* Air Force Cambridge Research Center Bedford, MA, 1959.

[92] H. B. Callen and T. A. Welton, "Irreversibility and generalized noise," *Phys. Rev.*, vol. 83, pp. 34–40, Jul 1951.

[93] M. Francoeur, M. P. Mengüç, and R. Vaillon, "Spectral tuning of near-field radiative heat flux between two thin silicon carbide films," *Journal of Physics D: Applied Physics*, vol. 43, p. 075501, feb 2010.

[94] O. S. Heavens, *Optical properties of thin solid films.* Courier Corporation, 1991.

[95] M. Francoeur, M. Pinar Mengüç, and R. Vaillon, "Solution of near-field thermal radiation in one-dimensional layered media using dyadic green's functions and the scattering matrix method," *Journal of Quantitative Spectroscopy and Radiative Transfer*, vol. 110, p. 2002–2018, Dec. 2009.

[96] S.-A. Biehs and J.-J. Greffet, "Near-field heat transfer between a nanoparticle and a rough surface," *Phys. Rev. B*, vol. 81, p. 245414, Jun 2010.

[97] B. Derjaguin, I. Abrikosova, and E. Lifshitz, "Direct measurement of molecular attraction between solids separated by a narrow gap," *Quarterly Reviews, Chemical Society*, vol. 10, no. 3, pp. 295–329, 1956.

[98] S. Molesky, "heatSlabs." `https://github.com/SeanMolesky/HeatSlabs`, 2020.

[99] A. W. Blakers, "Substrates for thin crystalline silicon solar cells," *Solar Energy Materials and Solar Cells*, vol. 51, no. 3, pp. 385–392, 1998.

[100] B. G. Streetman, S. Banerjee, *et al.*, *Solid state electronic devices*, vol. 4. Prentice hall New Jersey, 2000.

[101] C. Siu, *Electronic Devices, Circuits, and Applications*. Cham: Springer International Publishing, 2022.

[102] J. Huang, Z. Yin, and Q. Zheng, "Applications of zno in organic and hybrid solar cells," *Energy & Environmental Science*, vol. 4, no. 10, p. 3861, 2011.

[103] J. I. Morales-Aragonés, M. d. C. Alonso-García, S. Gallardo-Saavedra, V. Alonso-Gómez, J. L. Balenzategui, A. Redondo-Plaza, and L. Hernández-Callejo, "Online distributed measurement of dark i-v curves in photovoltaic plants," *Applied Sciences*, vol. 11, no. 4, 2021.

[104] S. R. Wenham, M. A. Green, M. E. Watt, R. Corkish, and A. Sproul, *Applied Photovoltaics*. Routledge, 0 ed., Jan. 2013.

[105] D. Feng, S. K. Yee, and Z. M. Zhang, "Improved performance of a near-field thermophotovoltaic device by a back gapped reflector," *Solar Energy Materials and Solar Cells*, vol. 237, p. 111562, 2022.

[106] M. Fox, *Optical Properties of Solids*. Oxford Master Series in Physics, OUP Oxford, 2010.

[107] C. Kittel, *Introduction to solid state physics*. John Wiley & sons, inc, 2005.

[108] M. Eldlio, F. Che, and M. Cada, *Drude-Lorentz Model of Semiconductor Optical Plasmons*, pp. 41–49. Dordrecht: Springer Netherlands, 2014.

[109] C. Fu and Z. Zhang, "Nanoscale radiation heat transfer for silicon at different doping levels," *International Journal of Heat and Mass Transfer*, vol. 49, no. 9, pp. 1703–1718, 2006.

[110] H. Fujiwara and R. W. Collins, *Spectroscopic ellipsometry for photovoltaics*, vol. 1. Springer, 2018.

[111] K. W. Böer and U. W. Pohl, *Elasticity and Phonons*, pp. 113–155. Cham: Springer International Publishing, 2023.

[112] M. Dresselhaus, G. Dresselhaus, S. B. Cronin, and A. G. Souza Filho, "Solid state properties," *Alemania: Springer-Verlag*, 2018.

[113] F. Wooten, *Optical properties of solids*. Citeseer, 1972.

[114] K. Schneider, "Optical properties and electronic structure of v2o5, v2o3 and vo2," *Journal of Materials Science: Materials in Electronics*, vol. 31, 07 2020.

[115] A. Taya, P. Rani, and M. K. Kashyap, "Moss-Burstein shift in La-doped BaSnO3; A novel electron transport layer material for hybrid halide perovskite solar cells," *AIP Conference Proceedings*, vol. 1942, p. 140039, 04 2018.

[116] S. Adachi, *Optical properties of crystalline and amorphous semiconductors: Materials and fundamental principles*. Springer Science & Business Media, 2012.

[117] D. Milovich, J. Villa, E. Antolin, A. Datas, A. Marti, R. Vaillon, and M. Francoeur, "Design of an indium arsenide cell for near-field thermophotovoltaic devices," *Journal of Photonics for Energy*, vol. 10, no. 2, p. 025503, 2020.

[118] T. S. Moss, "The interpretation of the properties of indium antimonide," *Proceedings of the Physical Society. Section B*, vol. 67, p. 775, oct 1954.

[119] N. Zhang and Y. Xiong, "Plasmonic semiconductors for advanced artificial photosynthesis," *Advanced Sensor and Energy Materials*, vol. 2, no. 1, p. 100047, 2023.

[120] W. Anderson, "Absorption constant of Pb1-xSnxTe and Hg1-xCdxTe alloys," *Infrared Physics*, vol. 20, p. 363–372, Nov. 1980.

[121] T. C. Harman and A. J. Strauss, "Band Structure of HgSe and HgSe–HgTe Alloys," *Journal of Applied Physics*, vol. 32, pp. 2265–2270, 10 1961.

[122] J. R. Dixon and J. M. Ellis, "Optical properties of n-type indium arsenide in the fundamental absorption edge region," *Phys. Rev.*, vol. 123, pp. 1560–1566, Sep 1961.

[123] R. von Baltz and W. Escher, "Quantum theory of free carrier absorption," *physica status solidi (b)*, vol. 51, no. 2, pp. 499–507, 1972.

[124] S. Basu, B. J. Lee, and Z. M. Zhang, "Infrared Radiative Properties of Heavily Doped Silicon at Room Temperature," *Journal of Heat Transfer*, vol. 132, p. 023301, 11 2009.

[125] B. J. Lee, Z. M. Zhang, E. A. Early, D. P. DeWitt, and B. K. Tsai, "Modeling radiative properties of silicon with coatings and comparison with reflectance measurements," *Journal of Thermophysics and Heat Transfer*, vol. 19, no. 4, pp. 558–565, 2005.

[126] P. J. Timans, "Emissivity of silicon at elevated temperatures," *Journal of Applied Physics*, vol. 74, pp. 6353–6364, 11 1993.

[127] G. Cataldo, J. A. Beall, H.-M. Cho, B. McAndrew, M. D. Niemack, and E. J.

Wollack, "Infrared dielectric properties of low-stress silicon nitride," *Opt. Lett.*, vol. 37, pp. 4200–4202, Oct 2012.

[128] M. Wang, M. Xie, L. Ferraioli, Z. Yuan, D. Li, D. Yang, and L. Pavesi, "Light emission properties and mechanism of low-temperature prepared amorphous sinx films. i. room-temperature band tail states photoluminescence," *Journal of Applied Physics*, vol. 104, p. 083504, Oct. 2008.

[129] R. Kitamura, L. Pilon, and M. Jonasz, "Optical constants of silica glass from extreme ultraviolet to far infrared at near room temperature," *Appl. Opt.*, vol. 46, pp. 8118–8133, Nov 2007.

[130] J. F. Creemer, S. Helveg, P. J. Kooyman, A. M. Molenbroek, H. W. Zandbergen, and P. M. Sarro, "A mems reactor for atomic-scale microscopy of nanomaterials under industrially relevant conditions," *Journal of Microelectromechanical Systems*, vol. 19, no. 2, pp. 254–264, 2010.

[131] J. D. Thompson, B. M. Zwickl, A. M. Jayich, F. Marquardt, S. M. Girvin, and J. G. E. Harris, "Strong dispersive coupling of a high-finesse cavity to a micromechanical membrane," *Nature*, vol. 452, p. 72–75, mar 2008.

[132] D. J. Wilson, C. A. Regal, S. B. Papp, and H. J. Kimble, "Cavity optomechanics with stoichiometric sin films," *Phys. Rev. Lett.*, vol. 103, p. 207204, Nov 2009.

[133] R. A. Norte, J. P. Moura, and S. Gröblacher, "Mechanical resonators for quantum optomechanics experiments at room temperature," *Phys. Rev. Lett.*, vol. 116, p. 147202, Apr 2016.

[134] D. Rugar, H. J. Mamin, and P. Guethner, "Improved fiber-optic interferometer for atomic force microscopy," *Applied Physics Letters*, vol. 55, pp. 2588–2590, 12 1989.

[135] D. Garcia-Sanchez, K. Y. Fong, H. Bhaskaran, S. Lamoreaux, and H. X. Tang, "Casimir force and in situ surface potential measurements on nanomembranes," *Physical Review Letters*, vol. 109, p. 027202, Jul 2012.

[136] M. Giroux, C. Zhang, N. Snell, G. Mu, M. Stephan, and R. St-Gelais, "High resolution measurement of near-field radiative heat transfer enabled by nanomechanical resonators," *Applied Physics Letters*, vol. 119, p. 173104, Oct. 2021.

[137] S. Schmid, L. G. Villanueva, and M. L. Roukes, *Fundamentals of nanomechanical resonators*, vol. 49. Springer, 2016.

[138] M. H. Sadd, *Elasticity: theory, applications, and numerics*. Academic Press, 2009.

[139] C. Zhang, M. Giroux, T. A. Nour, and R. St-Gelais, "Thermal radiation sensing using high mechanical q-factor silicon nitride membranes," in *2019 IEEE SENSORS*, pp. 1–4, 2019.

[140] N. Snell, C. Zhang, G. Mu, A. Bouchard, and R. St-Gelais, "Heat transport in silicon nitride drum resonators and its influence on thermal fluctuation-induced frequency noise," *Phys. Rev. Appl.*, vol. 17, p. 044019, Apr 2022.

[141] H. B. G. Casimir and D. Polder, "The influence of retardation on the london-van der waals forces," *Phys. Rev.*, vol. 73, pp. 360–372, Feb 1948.

[142] S. Hawking, *A Brief History of Time*. Bantam Books, 2011.

[143] M. Sparnaay, "Measurements of attractive forces between flat plates," *Physica*, vol. 24, no. 6, pp. 751–764, 1958.

[144] S. K. Lamoreaux, "The casimir force: background, experiments, and applications," *Reports on Progress in Physics*, vol. 68, p. 201–236, Jan. 2005.

[145] E. M. Lifshitz, "The theory of molecular attractive forces between solids," *Soviet Phys. JETP*, vol. 2, 1 1956.

[146] M. Antezza, L. P. Pitaevskii, S. Stringari, and V. B. Svetovoy, "Casimir-lifshitz force out of thermal equilibrium," *Phys. Rev. A*, vol. 77, p. 022901, Feb 2008.

[147] G. Bimonte, "A theory of electromagnetic fluctuations for metallic surfaces and van der waals interactions between metallic bodies," *Phys. Rev. Lett.*, vol. 96, p. 160401, Apr 2006.

[148] J. M. Obrecht, R. J. Wild, M. Antezza, L. P. Pitaevskii, S. Stringari, and E. A. Cornell, "Measurement of the temperature dependence of the casimir-polder force," *Phys. Rev. Lett.*, vol. 98, p. 063201, Feb 2007.

[149] P. Sadeghi, A. Demir, L. G. Villanueva, H. Kähler, and S. Schmid, "Frequency fluctuations in nanomechanical silicon nitride string resonators," *Physical Review B*, vol. 102, no. 21, p. 214106, 2020.

[150] M. Giroux, M. Stephan, M. Brazeau, S. Molesky, A. W. Rodriguez, J. J. Krich, K. Hinzer, and R. St-Gelais, "Measurement of near-field radiative heat transfer at deep sub-wavelength distances using nanomechanical resonators," *Nano Letters*, vol. 23, p. 8490–8497, Sept. 2023.

[151] R. S. DiMatteo, P. Greiff, S. L. Finberg, K. A. Young-Waithe, H. K. H. Choy, M. M. Masaki, and C. G. Fonstad, "Micron-gap thermophotovoltaics (mtpv)," *AIP Conference Proceedings*, vol. 653, no. 1, pp. 232–240, 2003.

[152] C. Tien, K. Lee, and A. Stretton, "Radiation heat transfer," *SFPE Handbook of Fire Protection Engineering, Section*, vol. 1, 2002.

[153] J. Shi, B. Liu, P. Li, L. Y. Ng, and S. Shen, "Near-field energy extraction with hyperbolic metamaterials," *Nano Letters*, vol. 15, p. 1217–1221, Feb 2015.

[154] G. A. Domoto, R. F. Boehm, and C. L. Tien, "Experimental investigation of ra-

diative transfer between metallic surfaces at cryogenic temperatures," *Journal of Heat Transfer*, vol. 92, p. 412–416, Aug 1970.

[155] V. c. v. Musilová, T. c. v. Králík, T. c. v. Fořt, and M. Macek, "Strong suppression of near-field radiative heat transfer by superconductivity in nbn," *Phys. Rev. B*, vol. 99, p. 024511, Jan 2019.

[156] P. C. Lipoma, "Wein bridge oscillator circuit," Tech. Rep. MSC-13686, NASA, 1971.

[157] B. M. Zwickl, W. E. Shanks, A. M. Jayich, C. Yang, A. C. Bleszynski Jayich, J. D. Thompson, and J. G. E. Harris, "High quality mechanical and optical properties of commercial silicon nitride membranes," *Applied Physics Letters*, vol. 92, no. 10, p. 103125, 2008.

[158] A. Demir, "Understanding fundamental trade-offs in nanomechanical resonant sensors," *Journal of Applied Physics*, vol. 129, no. 4, p. 044503, 2021.

[159] J. Fang, H. Frederich, and L. Pilon, "Harvesting nanoscale thermal radiation using pyroelectric materials," *Journal of Heat Transfer*, vol. 132, p. 092701, Sep 2010.

[160] I. Latella and P. Ben-Abdallah, "Graphene-based autonomous pyroelectric system for near-field energy conversion," *Scientific Reports*, vol. 11, no. 1, p. 19489, 2021.

[161] J. R. Howell and M. P. Mengüç, "Radiative transfer configuration factor catalog: A listing of relations for common geometries," *Journal of Quantitative Spectroscopy and Radiative Transfer*, vol. 112, no. 5, pp. 910–912, 2011.

[162] S. C. Mao, S. H. Tao, Y. L. Xu, X. W. Sun, M. B. Yu, G. Q. Lo, and D. L. Kwong, "Low propagation loss sin optical waveguide prepared by optimal low-hydrogen module," *Opt. Express*, vol. 16, pp. 20809–20816, Dec 2008.

[163] Ted Pella, Inc., "PELCO® Silicon Nitride Support Films for TEM." https://www.tedpella.com/grids_html/silicon-nitride.aspx#_21597_10, 2007. Accessed on 2022-12-21.

[164] Norcada, "Silicon Nitride Membrane Windows for TEM Analysis." https://www.norcada.com/products/nitride-windows-tem/, 2013. Accessed on 2023-04-05.

[165] G. Anetsberger, O. Arcizet, Q. P. Unterreithmeier, R. Rivière, A. Schliesser, E. M. Weig, J. P. Kotthaus, and T. J. Kippenberg, "Near-field cavity optomechanics with nanomechanical oscillators," *Nature Physics*, vol. 5, p. 909–914, Dec 2009.

[166] D. Thompson, L. Zhu, R. Mittapally, S. Sadat, Z. Xing, P. McArdle, M. M. Qazilbash, P. Reddy, and E. Meyhofer, "Hundred-fold enhancement in far-field radiative heat transfer over the blackbody limit," *Nature*, vol. 561, p. 216–221, Sep 2018.

[167] B. Song, D. Thompson, A. Fiorino, Y. Ganjeh, P. Reddy, and E. Meyhofer, "Radiative heat conductances between dielectric and metallic parallel plates with nanoscale gaps," *Nature Nanotechnology*, vol. 11, p. 509–514, Jun 2016.

[168] G. Mu, N. Snell, C. Zhang, X. Xie, R. Tahvildari, A. Weck, M. Godin, and R. St-Gelais, "Remote actuation of silicon nitride nanomechanical resonators using on-chip substrate capacitors," *Journal of Microelectromechanical Systems*, vol. 32, no. 1, pp. 29–36, 2023.

[169] S. D. Senturia, *Microsystem design*. Boston: Kluwer Academic Publishers, 2001.

[170] Y. Toivola, J. Thurn, R. F. Cook, G. Cibuzar, and K. Roberts, "Influence of deposition conditions on mechanical properties of low-pressure chemical vapor deposited low-stress silicon nitride films," *Journal of Applied Physics*, vol. 94, no. 10, pp. 6915–6922, 2003.

[171] G. Carlotti, P. Colpani, D. Piccolo, S. Santucci, V. Senez, G. Socino, and L. Verdini, "Measurement of the elastic and viscoelastic properties of dielectric films used in microelectronics," *Thin Solid Films*, vol. 414, no. 1, pp. 99–104, 2002.

[172] S.-E. Zhu, M. Krishna Ghatkesar, C. Zhang, and G. C. A. M. Janssen, "Graphene based piezoresistive pressure sensor," *Applied Physics Letters*, vol. 102, no. 16, p. 161904, 2013.

[173] K. Petersen, "Dynamic micromechanics on silicon: Techniques and devices," *IEEE Transactions on Electron Devices*, vol. 25, no. 10, pp. 1241–1250, 1978.

[174] J. DeSutter, L. Tang, and M. Francoeur, "A near-field radiative heat transfer device," *Nature nanotechnology*, vol. 14, no. 8, pp. 751–755, 2019.

[175] C. Metzger, M. Ludwig, C. Neuenhahn, A. Ortlieb, I. Favero, K. Karrai, and F. Marquardt, "Self-induced oscillations in an optomechanical system driven by bolometric backaction," *Phys. Rev. Lett.*, vol. 101, p. 133903, Sep 2008.

[176] J. Howell, *A Catalog of Radiation Configuration Factors*. McGraw-Hill, 1982.

[177] G. Hollinger, R. Skheyta-Kabbani, and M. Gendry, "Oxides on gaas and inas surfaces: An x-ray-photoelectron-spectroscopy study of reference compounds and thin oxide layers," *Physical Review B*, vol. 49, no. 16, p. 11159, 1994.

[178] L. M. Shaker, A. A. Al-Amiery, M. M. Hanoon, W. K. Al-Azzawi, and A. A. H. Kadhum, "Examining the influence of thermal effects on solar cells: a comprehensive review," *Sustainable Energy Research*, vol. 11, no. 1, p. 6, 2024.

[179] Y.-J. Jeon, D.-S. Kim, and Y.-E. Shin, "Study of characteristics of solar cells through thermal shock and high-temperature and high-humidity testing," *International journal of precision engineering and manufacturing*, vol. 15, pp. 355–360, 2014.

[180] J. Zhang, K. Shi, L. Lu, D. Feng, H. Liu, and X. Wu, "Experiments on near-field radiative heat transfer: a review," *Clean Energy Sci. Technol.*, vol. 1, p. 1, 2023.

[181] Goodfellow, "Carbon Powder." `https://www.goodfellow.com/global/carbon-powder-group`, 2018. Accessed on 2025-03-04.

[182] M. Giroux, S. Molesky, R. St-Gelais, and J. J. Krich, "Radiator tailoring for enhanced performance in inas-based near-field thermophotovoltaics," *Solar Energy Materials and Solar Cells*, vol. 292, p. 113804, 2025.

[183] I. A. O. Tedah, F. Maculewicz, D. E. Wolf, and R. Schmechel, "Thermoelectrics versus thermophotovoltaics: two approaches to convert heat fluxes into electricity," *Journal of Physics D: Applied Physics*, vol. 52, no. 27, p. 275501, 2019.

[184] M. Giroux, "Matgiroux/permittivity: Initial release." `https://doi.org/10.5281/zenodo.15056994`, Mar. 2025.

[185] J. R. Dixon, "Optical absorption mechanisms in indium arsenide," in *Proceedings of 5th International Conference on Physics of Semiconductors*, (Prague), p. 366, 1960.

[186] R. M. Culpepper and J. R. Dixon, "Free-carrier absorption in n-type indium arsenide," *JOSA*, vol. 58, no. 1, pp. 96–102, 1968.

[187] A. Baraskar, V. Jain, M. A. Wistey, U. Singisetti, Y. J. Lee, B. Thibeault, A. Gossard, and M. J. W. Rodwell, "High doping effects on in-situ ohmic contacts to n-inas," in *2010 22nd International Conference on Indium Phosphide and Related Materials (IPRM)*, pp. 1–4, 2010.

[188] M. A. Green, "Analytical treatment of trivich–flinn and shockley–queisser photovoltaic efficiency limits using polylogarithms," *Progress in Photovoltaics: Research and Applications*, vol. 20, no. 2, pp. 127–134, 2012.

[189] W. Shockley and H. J. Queisser, "Detailed balance limit of efficiency of p-n junction solar cells," *Journal of Applied Physics*, vol. 32, pp. 510–519, 03 1961.